Lamellar Grating Interferometer Based MEMS Fourier Transform Infrared Spectrometer

by

Nadire Pelin Ayerden

A Thesis Submitted to the
Graduate School of Sciences and Engineering
in Partial Fulfillment of the Requirements for
the Degree of

Master of Science

in

Electrical and Computer Engineering

Koç University

March 2012

Koç University

Graduate School of Sciences and Engineering

This is to certify that I have examined this copy of a master's thesis by

Nadire Pelin Ayerden

and have found that it is complete and satisfactory in all respects,
and that any and all revisions required by the final
examining committee have been made.

Committee Members:

____

Prof. Dr. Hakan Ürey, (Advisor)

____

Assoc. Prof. Erdem Alaca

____

Asst. Prof. Şükrü Ekin Kocabaş

Date: 06.03.2012

ABSTRACT

Fourier transform infrared (FTIR) spectroscopy is a widely used non-contact optical material characterization method that is used for chemical analysis of solids, fluids, gases, and process flows. FTIR utilizes a black body light source with broad spectrum, moving opto-mechanical components, and a detector. Current FTIR spectrometers offer good spectral resolution (few cm^{-1} or better); however, they are costly bench top laboratory instruments, require very high opto-mechanical precision, sensitive to vibrations due to interferometric detection principle, and have low measuring speed (few seconds to minutes). A portable FTIR system is needed as it would allow field use and has the potential to open up new research directions and applications.

The aim of this project was to build a miniaturized handheld FTIR spectrometer with high measuring speed (1-2msec) and moderate spectral sensitivity ($10cm^{-1}$) that works across a wide wavelength range in the mid-infrared (2.5-16μm) region. The project is done as a part of the European Commission funded project called MEMFIS within a consortium. A novel lamellar grating interferometer (LGI) based on micro-electro-mechanical-system (MEMS) technology and electrostatic actuation is at the heart of the FTIR system and offers the required precision, speed, and the vibration immunity for a portable system. LGI MEMS device was designed and microfabricated by our group prior to this thesis research. LGI is a dynamic diffraction grating operated at resonance and functions as a high-precision opto-mechanical interferometer with key important advantages compared to other types of interferometers.

This thesis mainly focuses on the detailed optical and mechanical characterization of the LGI MEMS device and its integration into a fully functional FTIR system using the source, detector, and IR optics. For this purpose, MEMS devices fabricated in five separate runs are characterized mechanically and optically. For mechanical characterization, two

automatized systems based on laser Doppler vibrometry and laser fringe counting are developed using a Labview based controller. Physical optics simulations of the system are performed in MATLAB and ray-tracing simulations are performed in ZEMAX to find the optimum combination of optical components. A fully functional LGI based FTIR spectrometer system is built on an optical table and successfully benchmarked with other FTIR systems using polystyrene film samples. The system can currently achieve about $30cm^{-1}$ spectral resolution. This is the best MEMS-based LGI system developed to date considering the spectral resolution and clear aperture size of $10mm^2$. To increase the mechanical deflection (i.e., improve spectral resolution) and to avoid problems related to electrostatic actuation such as pull-in and nonlinear frequency response, acoustic excitation using a speaker and mechanically-coupled excitation using a piezoelectric-vibrator are introduced as alternative actuation methods. As another application of the FTIR system, measurement of photovoltaic solar cell thin film thickness uniformity is exploited.

ÖZET

Fourier dönüşümü kızılötesi (FTIR) spektroskopi temassız optik yolla maddelerin kimyasal analizinde yaygın olarak kullanılan bir yöntemdir. Fourier dönüşümü spektrometrelerde kara cisim ışıması yapan ışık kaynağı, hareketli optik-mekanik parçalar ve dedektör kullanılır. Mevcut FTIR spektrometreler birkaç cm^{-1} veya daha iyi çözünürlük sunmalarına rağmen kullanımı laboratuarla kısıtlı pahalı cihazlardır. Ek olarak yüksek optik-mekanik hassasiyet gerektirir, girişimölçer temelli algılama prensibi nedeniyle sallanmaya duyarlıdır ve birkaç saniyeden birkaç dakikaya uzanan düşük ölçüm hızlarına sahiplerdir. Dolayısıyla saha kullanımına izin vermesi ve yeni araştırma ve uygulama alanları yaratma potansiyeli olmasından ötürü taşınabilir bir FTIR spektroskopi sistemi geliştirilmesi gerekmektedir.

Bu projenin temel amacı orta kızılötesi dalgaboyunda (2.5-16µm) geniş bir dalgaboyu aralığında çalışan hızlı (1-2ms) ve ortalama çözünürlüklü ($10cm^{-1}$) küçük, taşınabilir bir FTIR spektrometre tasarlamak ve üretmektir. Bahsi geçen proje, Avrupa Birliği tarafından desteklenen MEMFIS projesi kapsamında tamamlanmıştır. Taşınabilir bir sistem için gereken hassasiyet, hız ve sallanmaya duyarsızlık mikro-elektronik-mekanik-sistemler (MEMS) temelli elektriksel olarak çalıştırılan kırınım ızgaralı girişimölçer tarafından karşılanabilir. LGI MEMS cihazı bu araştırma tezinden önce grubumuz tarafından tasarlanmış ve üretilmiştir. LGI, rezonans frekansında çalıştırılan ve diğer girişimölçerlerle kıyaslandığında önemli avantajları olan yüksek hassasiyetli bir optik-mekanik girişimölçer olarak tanımlanabilecek bir dinamik kırınım ızgarasıdır.

Bu tezde temel olarak LGI MEMS cihazının detaylı optik ve mekanik karakterizasyonu ile cihazın ışık kaynağı, dedektör ve kızılötesi optik elemanlar ile birleştirilerek çalışan bir FTIR sistemine dönüştürülmesi anlatılmıştır. Bu amaçla, beş kez üretimi yapılan MEMS cihazları mekanik ve optik olarak test edilmiştir. Mekanik testler için Labview ortamında

lazer Doppler vibrometre ve lazer saçak sayımı temelli otomatik sistemler geliştirilmiştir. Optik masa üzerine LGI temelli FTIR spektrometre kurulmuş ve polisitren örneği kullanılarak diğer sistemlerle başarılı bir şekilde kıyaslanmıştır. Mevcut sistemle yaklaşık $30cm^{-1}$ çözünürlük sağlanmaktadır. Çözünürlük açısından bakıldığında $10mm^2$ açık aralıkla geliştirilen bu sistem, bugüne kadar geliştirilmiş en iyi MEMS temelli LGI sistemidir. Hareket genliğini artırmak (ya da çözünürlüğü iyileştirmek) ve cihazın elektriksel olarak çalıştırılması sonucu ortaya çıkan tutulma ve lineer olmayan frekans cevabı gibi sorunları engellemek için akustik dalgalar ve piezoelektrik-vibrasyon ile çalıştırma alternatif yöntemler olarak sunulmuştur. Ek bir uygulama olarak FTIR sistemini kullanarak ışıl-elektriksel güneş pili ince film kalınlık ölçümü önerilmiştir.

ACKNOWLEDGEMENT

I would like to thank Prof. Hakan Ürey for letting me study in such a productive research environment as OML. It was a privilege to participate in the MEMFIS project with pioneer partners under his supervision. I am grateful to Thilo Sandner from Fraunhofer IPMS for helping me during my internship, Adam Piotrowski from Vigo Systems and Stephan Luettjohann from Bruker Optics for their valuable opinions. Above all, I would like to thank Jean-Louis Stehle from SOPRA for answering all my questions with patience. In addition, I would like to thank Dr. Çağlar Ataman and Hüseyin R. Seren for building a solid background in the project and leaving behind two valuable theses for me to learn new things each time I read. I am also thankful to Prof. Erdem Alaca and Prof. Şükrü Ekin Kocabaş for taking part in my thesis committee.

It would have been impossible to complete my studies without the help of my colleagues and good friends at OML, especially Selim, Sven and Onur. I want to thank Selim for helping me in everything regardless of the subject. He always had practical solutions waiting for me. I am grateful to Sven for being a great project partner as well as being a great geek friend. Working in the clean room was not only bearable but also a lot fun with him. I also want to thank Sven for letting me improve my ninja skills on him without getting hurt. My mentor, Onur always encouraged me even if he was thousands of kilometers away.

I had the chance to work with many brilliant friends at OML. I want to thank Aslıhan for teaching me how to do characterization when I had no idea what characterization even meant. I also want to thank Hüseyin for kindly answering all my questions. It was a pleasure to get to know Kutal and Adana culture inevitably. I want to thank Erdem for helping me adjust to the university and being a great desk mate. It was a privilege to work with Burak, learning geography with Zeynep, listening to a new song with Cem everyday,

going to every fish restaurant in the city with Erhan, consuming less with Kaan, learning to ride horse with Kıvanç and taking car rides with Onur and Ulaş. I also want to thank my colleagues Utku, Aref, Sridhar and Jaibir.

Last but not least, I am deeply grateful to my family for doubtlessly believing in me. I would not be able to complete this thesis without the support of my family to whom I dedicate it.

LIST OF FIGURES

Figure 1.1 Electromagnetic spectrum. 2
Figure 1.2 Infrared active and inactive molecules. 3
Figure 1.3 Fundamental vibrational modes of H_2O. 4
Figure 1.4 (a) Michelson interferometer based, (b) LGI based FT spectrometer. (Dashed frame shows the interferometer.) 6
Figure 1.5 One of the first lamellar grating interferometers with Czerny-Turner optics [8]. 7
Figure 1.6 Lamellar grating (side view) 7
Figure 1.7 Term A of equation (1-11) for $\Lambda = 100\mu m$ and $\lambda = 10\mu m$. 10
Figure 1.8 Term B of equation (1-11) for $\Lambda = 100\mu m$ and $\lambda = 10\mu m$. 11
Figure 1.9 Multiplication of terms A and B of equation (1-11) for $\Lambda = 100\mu m$ and $\lambda = 10\mu m$. 11
Figure 1.10 (a) Term C for $d = \lambda/4$ (blue) and $d = \lambda/2$ (red). (b) Multiplication of all terms for $d = \lambda/4$ (blue) and $d = \lambda/2$ (red). 12
Figure 1.11 (a) LGI MEMS device by O. Manzardo [9]. (b) ARCoptix spectrometer installed on an electronic board [10]. 13
Figure 1.12 LGI MEMS device by KOC University. 14
Figure 1.13 LGI MEMS devices by National University of Singapore with (a) electromagnetic actuation [12] and (b) electrostatic actuation [14]. 14
Figure 1.14 LGI MEMS design with serpentine springs. (1) Stationary grating fingers. (2) Moving grating fingers. (3) Rigid backbone. (4) Serpentine springs. 16
Figure 1.15 First four natural oscillation modes of LGI with serpentine springs. 17
Figure 1.16 (a)-(c) Microscope images of the fabricated device. (d) Frequency response with 28V sinusoidal excitation. 17

Figure 1.17 LGI MEMS design with pantograph springs (1st prototype). (1) Stationary grating fingers. (2) Moving grating fingers. (3) Rigid backbone. (4) Pantograph spring....18
Figure 1.18 First four natural oscillation modes of LGI with pantograph springs (1st prototype). 19
Figure 1.19 LGI MEMS design with pantograph springs (2nd prototype). (1) Moving grating fingers. (2) Rigid backbone. (3) Pantograph spring....................20
Figure 2.1 (a) MEMS device mounted on specifically designed PCB. (b) PCB designed for MEMS testing. 24
Figure 2.2 Mechanical characterization setup with laser Doppler vibrometer. 25
Figure 2.3 Front panel of laser Doppler vibrometer based Labview program. 26
Figure 2.4 Block diagram of LDV based Labview program. 27
Figure 2.5 Fringe counting based mechanical characterization setup....................28
Figure 2.6 Optical part of laser fringe counting setup. 29
Figure 2.7 Front panel of laser fringe counting based Labview program. 30
Figure 2.8 Block diagram of laser fringe counting based Labview. 31
Figure 2.9 Optical setup for comparison of laser fringe counting and LDV based systems. 32
Figure 2.10 Frequency sweeps obtained from both laser fringe counting and LDV based systems simultaneously. 33
Figure 2.11 Mechanical characterization results of FabRun 1_KOC. 35
Figure 2.12 (a) A bare LGI MEMS device from FabRun 1_KOC on a coin. (b) Wirebonded device....................36
Figure 2.13 (a) SEM picture of a pre-deflected LGI MEMS device from FabRun 1_IPMS. (b) Frequency response at 62V input voltage. 37
Figure 2.14 Frequency response of an LGI device from FabRun 2_IPMS at various pressures. 38

Figure 2.15 Frequency and voltage responses of FabRun 2_KOC devices. 39
Figure 2.16 LGI MEMS device fabricated in (a) FabRun 2_KOC, (b) FabRun 3_KOC. ...39
Figure 2.17 Frequency sweeps with square and sine wave actuation, respectively. 40
Figure 2.18 (a) Speaker actuation setup. (b) Piezoelectric actuation setup. (c) Frequency responses with all actuation methods. 42
Figure 3.1 (a) Interferogram before resampling. (b) Interferogram after resampling. (c) Spectrum. 43
Figure 3.2 (a) Discrete Fourier transform of a single sided interferogram. (b) Fast Fourier transform of a double sided interferogram. (c) Fast Fourier transform of a single sided interferogram. 47
Figure 3.3 OPD calculation with nonzero incidence angle illumination. 48
Figure 3.4 Device III-SM actuated with 30V_{pp} at 667Hz at various incidence angles. 49
Figure 3.5 Optical characterization setup and data analysis algorithm. 50
Figure 3.6 (a) Interferograms measured with a red (λ=632.8nm) and a reference blue (λ=408nm) laser at small deflection. (b) Interferogram before resampling at large deflection. (c) Interferogram after resampling. (d) Magnitude spectrum. 51
Figure 3.7 (a) Zoomed view of the laser interferogram. (b) Interferogram before resampling with its DC offset removed. (c) Interferogram after resampling. (d) Magnitude spectrum. 52
Figure 4.1 Schematics of simulated setup. 55
Figure 4.2 Flowchart of the algorithm. FBP(x): Fresnel beam propagation for distance x. R_1, R_2: Amplitude reflectance function of moving, stationary grating fingers. L: Amplitude transmittance function of lens. 56
Figure 4.3 Exemplary spectrum for SBR definition. 59

Figure 4.4 Physical optics simulation results of case#3 for λ=3.3μm. (a) Interferogram. (b) Magnitude spectrum. (c) Wave pattern at the detector plane at the highest deflection. The red box represents detector window. 60
Figure 4.5 Physical optics simulation results of case#8 for λ=3.3μm. (a) Interferogram. (b) Magnitude spectrum. (c) Wave pattern at the detector plane at the highest deflection. The red box represents detector window. 61
Figure 4.6 Physical optics simulation results of case#13 for λ=3.3μm. (a) Interferogram. (b) Magnitude spectrum. (c) Wave pattern at the detector plane at the highest deflection. The red box represents detector window. 62
Figure 4.7 Physical optics simulation results of case#3 for λ=6.45μm. (a) Interferogram. (b) Magnitude spectrum. (c) Wave pattern at the detector plane at the highest deflection. The red box represents detector window. 63
Figure 4.8 Physical optics simulation results of case#8 for λ=6.45μm. (a) Interferogram. (b) Magnitude spectrum. (c) Wave pattern at the detector plane at the highest deflection. The red box represents detector window. 64
Figure 4.9 Physical optics simulation results of case#13 for λ=6.45μm. (a) Interferogram. (b) Magnitude spectrum. (c) Wave pattern at the detector plane at the highest deflection. The red box represents detector window. 65
Figure 4.10 Physical optics simulation results of case#3 for λ=16μm. (a) Interferogram. (b) Magnitude spectrum. (c) Wave pattern at the detector plane at the highest deflection. The red box represents detector window. 66
Figure 4.11 Physical optics simulation results of case#8 for λ=16μm. (a) Interferogram. (b) Magnitude spectrum. (c) Wave pattern at the detector plane at the highest deflection. The red box represents detector window. 67

Figure 4.12 Physical optics simulation results of case#13 for λ=16μm. (a) Interferogram. (b) Magnitude spectrum. (c) Wave pattern at the detector plane at the highest deflection. The red box represents detector window. 68
Figure 4.13 Physical optics simulation results for all lens combinations. 69
Figure 4.14 (a) ZEMAX design and (b) Detector view of case#3. 70
Figure 4.15 (a) ZEMAX design and (b) Detector view of case#8. 71
Figure 4.16 (a) ZEMAX design and (b) Detector view of case#13. 71
Figure 5.1 MEMFIS source and its spectrum. 74
Figure 5.2 MEMFIS Detector. 74
Figure 5.3 LGI based FTS operation. PD: Photodetector. ZCD: Zero-crossing detector, ADC: Analog-to-digital converter. 76
Figure 5.4 Light absorption in sample. 77
Figure 5.5 (a) Excitation voltage and deflection curve vs. time. (b) Laser interferogram. (c) IR interferogram. 79
Figure 5.6 Actual LGI based FTIR spectrometer setup. 80
Figure 5.7 Data acquisition and analysis with chirped clock sampling. 81
Figure 5.8 Data acquisition and analysis with interpolated zero-crossing detection sampling. 81
Figure 5.9 IR interferograms with and without sample before filtering. 84
Figure 5.10 IR interferograms with and without sample after filtering. 85
Figure 5.11 IR interferograms with and without sample after filtering – zoomed in. 86
Figure 5.12 Magnitude spectrum with and without sample. 87
Figure 5.13 % Transmittance and absorbance spectrum. 88
Figure 5.14 Effect of deflection on resolution. 89
Figure 5.15 Effect of data cropping on resolution. 91
Figure 5.16 Effect of asymmetry in resolution. 92

Figure 5.17 Effect of averaging on resolution....................93
Figure 5.18 Effect of at which step averaging is applied on resolution. 94
Figure 5.19 Effect of reference laser interferogram on resolution. 95
Figure 5.20 Spectra obtained with different lens combinations. 96
Figure 5.21 Spectrum comparison of LGI based FTIR spectrometer and Bruker Optics' Alpha-T FTIR spectrometer. 97
Figure 5.22 (a) LGI based FTIR spectrometer modified for film thickness measurement. (b) Detailed view of sample plane [29]. 98
Figure 5.23 IR interferogram obtained with 20μm silicon film in the optical path. 99

LIST OF TABLES

Table 1.1 Number of fundamental vibrations. 4
Table 1.2 First four natural oscillation modes of LGI with pantograph springs (2nd prototype). 20
Table 2.1 Design variations..33
Table 2.2 LGI MEMS device fabrication summary..34
Table 2.3 First four experimental oscillation modes of LGI_P2_Koc_D5 devices. 41
Table 4.1 Available optical components. 56
Table 4.2 Physical optics simulation results. 57
Table 4.3 Simulated detector power and experimentally detected signal amplitude for case#3, case#8 and case#13. 72

Table of Contents

ACKNOWLEDGEMENT .... **vii**

LIST OF FIGURES .... **ix**

LIST OF TABLES .... **xv**

1 INTRODUCTION **1**

1.1 Vibrational Spectroscopy 1

1.2 Fourier Transform Infrared (FTIR) Spectroscopy 4

1.2.1 Michelson Interferometer 5

1.2.2 Lamellar Grating Interferometer (LGI) 6

1.3 MEMS-based LGI Devices in the Literature 13

1.4 LGI MEMS Devices Developed at KOC 15

1.4.1 LGI Design with Serpentine Springs 16

1.4.2 LGI Design with Pantograph Springs 18

1.5 Contributions of the Thesis 21

2 MECHANICAL CHARACTERIZATION **23**

2.1 Mechanical Characterization Methods 24

2.1.1 Laser Doppler Vibrometry Setup 24

2.1.2 Laser Fringe Counting Setup 28

2.2 Mechanical Characterization Results 33

2.3 Alternative Actuation Methods 41

3 OPTICAL CHARACTERIZATION **43**

3.1 Resolution in FT Spectroscopy 43

3.2 Effect of Incidence Angle on Resolution 47

3.3 Optical Characterization Results....49

4 OPTICAL SIMULATIONS....53

4.1 Optical Setup Optimization....54

4.2 Optical Setup Power Calculations....69

5 SPECTROMETER SYSTEM INTEGRATION....73

5.1 Infrared Source and Detector....73

5.2 LGI based FTS System Operation....75

5.3 Data Acquisition and Analysis....80

5.4 Spectrum of Polystyrene....88

5.5 Application: Thin Film Thickness Measurement....97

6 CONCLUSION....100

BIBLIOGRAPHY....102

1 INTRODUCTION

Spectroscopy is the study of interaction between electromagnetic radiation and matter. It is based on the principle that under certain conditions, materials absorb or emit radiation. It is a widely used method for identification of materials due to its capability of monitoring the sample without physical contact. There are several spectroscopic techniques operating on different wavelength ranges depending on the application.

1.1 Vibrational Spectroscopy

Infrared spectroscopy is one of the most frequently used spectroscopic techniques since the 1940s. Initially, dispersive elements such as prisms and later, gratings were being used. By the introduction of Fourier transform spectrometers, the quality of infrared spectrum increased substantially while reducing the acquisition time. Infrared spectroscopy works in the infrared region of the electromagnetic spectrum which is divided into three subsections: near infrared (0.8-2.5µm), mid infrared (2.5-25µm) and far infrared (25-1000µm) exciting rotations, vibrations and harmonics respectively. In this thesis, a Fourier transform spectrometer working in mid infrared wavelength range (2.5-16µm) is be investigated.

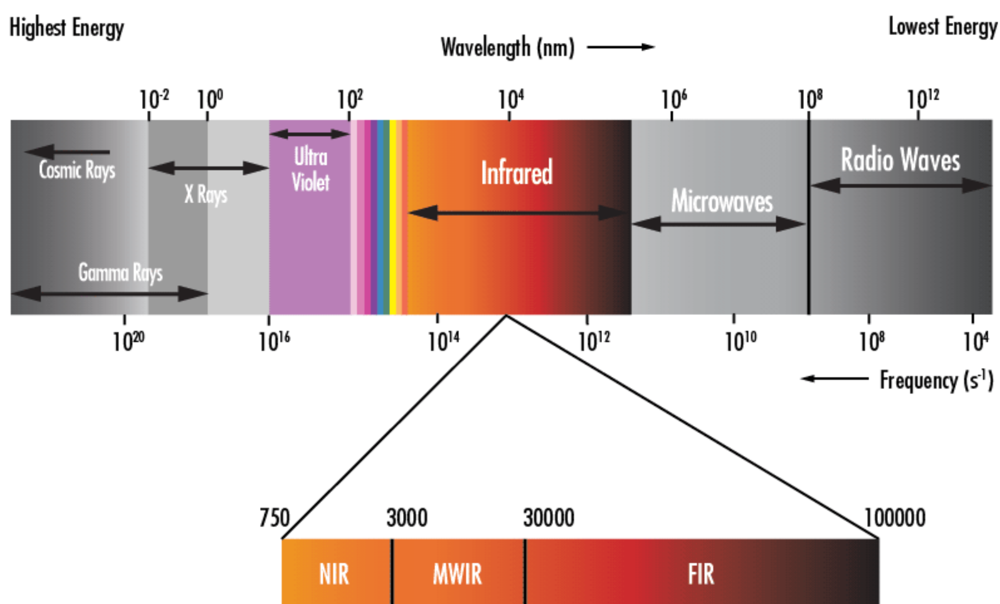

Figure 1.1 Electromagnetic spectrum.

Mid infrared spectroscopy relies on the vibration of atoms in a molecule. In this technique, infrared radiation is passed through a sample and the ratio of absorbed to incident radiation is recorded. When the energy of radiation matches the energy of a vibration, an absorption peak in the spectrum occurs. Vibration related to infrared radiation can be represented with quantized discrete energy levels. When a molecule interacts with radiation, a quantized energy given with the below equation is absorbed or emitted:

$$\Delta E = h\upsilon = h\frac{c}{\lambda} = hc\bar{\upsilon} \tag{1-1}$$

where h is Planck's constant ($h = 6.6 \times 10^{-34}\,Js$), υ is frequency, c is velocity of light, and $\bar{\upsilon}$ is wavenumber [1]. The energy difference (ΔE) for most of the vibrational modes corresponds to the mid infrared range.

Infrared radiation interacts with a molecule only if the dipole moment of the molecule changes due to vibration. The size of dipole moment deformation also determines the

absorption strength. Dipole moment of N charges is calculated with the following formula where $\boldsymbol{p}$ is dipole moment, q is charge, and $\boldsymbol{d}$ is position vector:

$$\boldsymbol{p} = \sum_{i=1}^{N} q_i \, \boldsymbol{d_i} \tag{1-2}$$

Molecules which have a dipole moment that changes with vibration are called *infrared active* (HCl, CO, etc.), whereas molecules with zero dipole moment are defined as *infrared inactive* (O_2, H_2, Cl_2, etc.). Examples of such molecules are shown below.

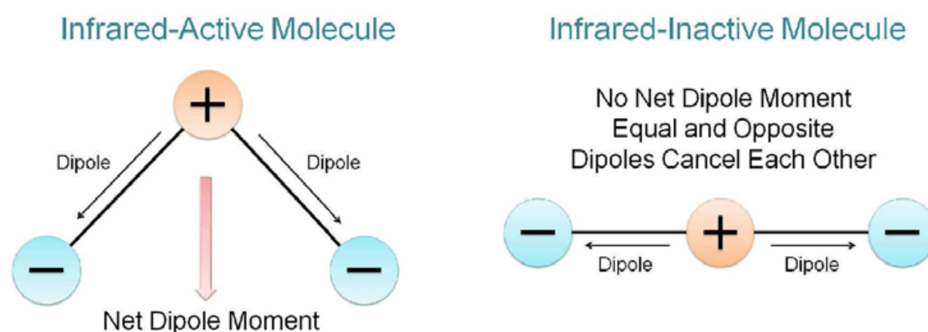

Figure 1.2 Infrared active and inactive molecules.

For a diatomic molecule, frequency (or wavenumber) of vibration modes can be described by the stiffness of the bond and the reduced mass (μ), a combination of individual atomic masses (m_1, m_2) at each end of the bond.

$$\mu = \frac{m_1 m_2}{m_1 + m_2} \tag{1-3}$$

$$\bar{\upsilon} = \frac{1}{2\pi c}\sqrt{\frac{k}{\mu}} \tag{1-4}$$

Molecular vibrations can be divided into two groups, bending and stretching. A molecule that has n atoms has a net number of fundamental vibrations as given in the table below [2].

molecule	degrees of freedom
linear	3n-6
nonlinear	3n-5

Table 1.1 Number of fundamental vibrations.

For instance, water (H_2O), a nonlinear molecule, has 3 fundamental vibrations as shown in Figure 1.3.

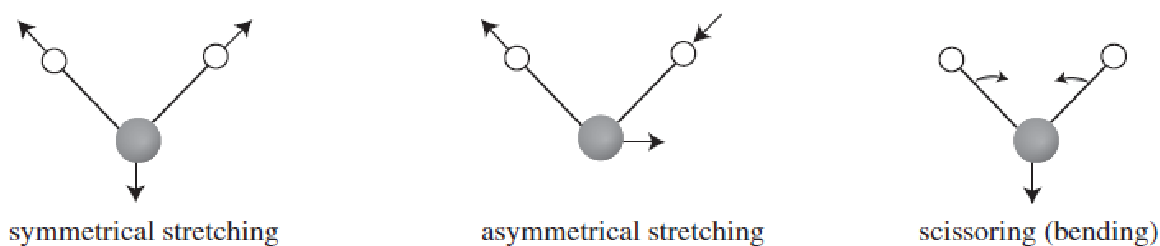

Figure 1.3 Fundamental vibrational modes of H_2O.

Interpretation of infrared spectra is easily done using well prepared IR absorption tables instead of performing the aforementioned calculations. The identifying properties of an absorption band are intensity, shape and position.

1.2 Fourier Transform Infrared (FTIR) Spectroscopy

An interferogram is created by dividing the source beam into two either by a beam splitter (amplitude division) or a diffraction grating (wavefront division) and introducing an optical path difference prior to interference. In Fourier transform spectroscopy, this information is translated into spectral domain by means of the mathematical method of Fourier transform [3].

In dispersive spectroscopy on the other hand, incoming light is dispersed into its spectral components by a prism or a grating and then detected by a single detector or an array of detectors. FTIR has three major advantages compared to dispersive methods:

- *Felgett (Multiplex) advantage*: In FTIR, all frequencies are measured simultaneously and the entire targeted part of the spectrum is covered at once while every wavelength is measured individually in dispersive spectrometers with single detector. In FT spectroscopy data collection is faster than that of dispersive spectroscopy [4].
- *Jacquinot (Throughput) advantage*: Since the frequency reaching the sample is limited with a slit in dispersive spectroscopy, the energy reaching the sample and resultantly the energy observed at the detector is low. This results in a low signal-to-noise ratio, thus low resolution in dispersive systems compared to FTIR. Hence, optical throughput is higher in FTIR spectrometers [5].
- *Connes advantage*: External calibration is required over time in dispersive spectrometers while a HeNe reference laser is used in FTIR spectrometers, which as a result are regarded as internally calibrated instruments [6].

FT spectrometers are classified according to the interferometers employed in the system. Two main interferometer types are Michelson interferometer and lamellar grating interferometer.

1.2.1 Michelson Interferometer

Michelson interferometer is the most commonly used interferometer in FTIR systems. Two mirrors, one stationary and one moving are used to create an optical path difference. The beam is divided into two by a beam splitter, which is placed at the center of the interferometer and inclined at an angle of 45º. Ideally half of the light is transmitted and the other half is reflected. The mirrors are located on both arms of the interferometer perpendicular to each other. The beam gets reflected from both mirrors after amplitude division by the beam splitter. Later, these beams are superimposed. By scanning the

moving mirror over a distance, an interference pattern is created at the output of the interferometer.

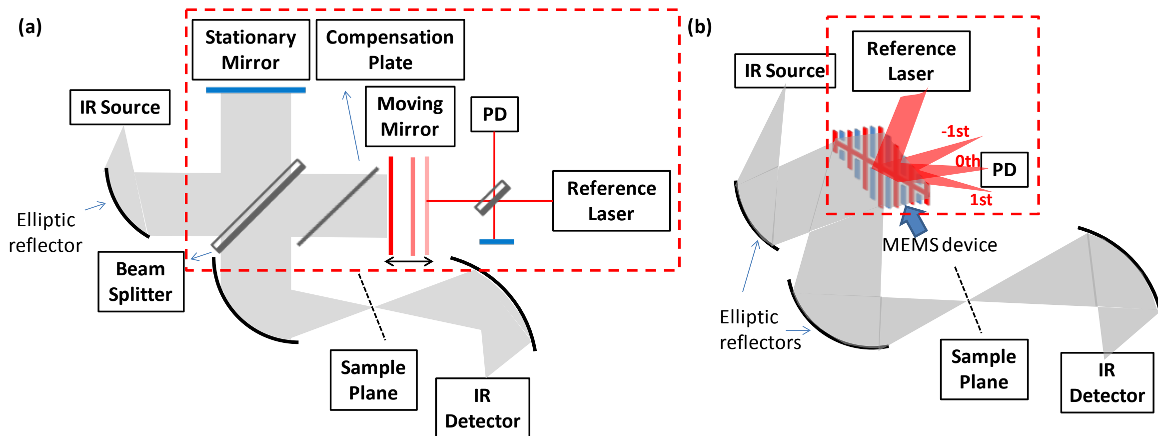

Figure 1.4 (a) Michelson interferometer based, (b) LGI based FT spectrometer. (Dashed frame shows the interferometer.)

The beam that is reflected from the stationary mirror passes through the beam splitter three times while the beam that is reflected from the moving mirror passes through the beam splitter only once. A compensation plate is used in the optical path of the moving mirror to counterbalance the difference introduced by the beam splitter. The second interferometer shown in Figure 1.4 (a), illuminating the backside of the moving mirror, is used as a reference to correct for tilt and non-uniform velocity in the moving mirror.

1.2.2 Lamellar Grating Interferometer (LGI)

Lamellar grating interferometer was invented by John Strong in 1950's [7]. One of the first lamellar grating interferometers is shown in Figure 1.5.

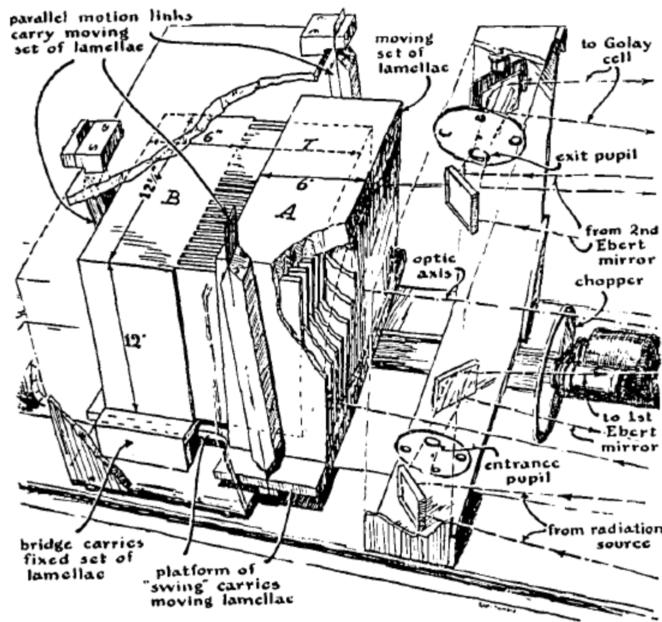

Figure 1.5 One of the first lamellar grating interferometers with Czerny-Turner optics [8].

Lamellar grating interferometer has basically the same working principle as Michelson interferometer as illustrated in Figure 1.4(b) . In LGI both moving and stationary mirrors are combined in one device. One set of grating fingers moves in the out-of-plane mode while the other set remains stationary as shown in Figure 1.6.

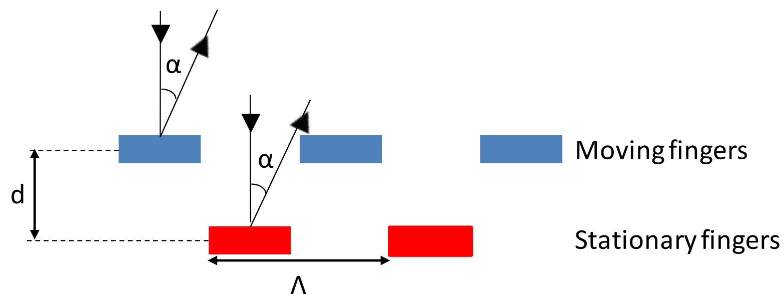

Figure 1.6 Lamellar grating (side view)

LGI systems offer several advantages compared to the Michelson interferometers.

- Since both stationary and moving mirrors are combined in one device, LGI eliminates separate reference mirror.
- Michelson interferometer uses a beam splitter to divide the light coming from the source into two beams whereas LGI does wavefront division by the grating structure. As a result, neither beam splitter nor compensation plate is needed in LGI.
- LGI does not require vacuum packaging of MEMS as Michelson configuration.
- There is no need for interference alignment efforts in LGI.
- LGI is less susceptible to vibration since it eliminates the use of interferometer optics and combines both stationary and moving mirrors on the same device.

To summarize, LGI is smaller, more robust and easier to assemble.

Diffraction theory of lamellar grating interferometers is investigated in detail in [7] and is summarized below. Total diffracted wave amplitude of a lamellar grating is given by the equation below where E_{moving} and $E_{stationary}$ are diffracted wave amplitudes of moving and stationary grating fingers respectively.

$$E_{tot} = E_{moving} + E_{stationary} \tag{1-5}$$

Diffracted wave amplitude of a set of fingers can be defined in terms of the diffracted wave amplitude of a single finger (E_s) and the interference function between diffracted waves from a set of fingers (F).

$$E = E_s F \tag{1-6}$$

$$E_s \, \alpha \, \frac{\sin\left[\frac{\pi\Lambda \sin\alpha}{2\lambda}\right]}{\frac{\pi\Lambda \sin\alpha}{2\lambda}} \tag{1-7}$$

$$F\ \alpha\ \frac{\sin\left[\frac{N\pi\Lambda\sin\alpha}{\lambda}\right]}{\sin\left[\frac{\pi\Lambda\sin\alpha}{\lambda}\right]} exp\left(-i\left[\frac{(N-1)\pi\Lambda\sin\alpha}{\lambda}\right]\right) \tag{1-8}$$

Since moving and stationary grating fingers are identical and there is only a phase difference between the reflected waves, E_{tot} can be further described as follows:

$$E_{tot} = E_s F + E_s F e^{i\varphi} \tag{1-9}$$

where phase is $\varphi = 2\pi\rho/\lambda$ and the optical path difference is $\rho = d[(1 + cos\alpha) + (\Lambda/2d)sin\alpha]$ for a normally incident wave. Therefore the total amplitude of the wave diffracted from lamellar grating is,

$$E_{tot}\alpha \frac{\sin\left[\frac{\pi\Lambda\sin\alpha}{2\lambda}\right]}{\frac{\pi\Lambda\sin\alpha}{2\lambda}} \frac{\sin\left[\frac{N\pi\Lambda\sin\alpha}{\lambda}\right]}{\sin\left[\frac{\pi\Lambda\sin\alpha}{\lambda}\right]} \left(1 + e^{i\varphi}\right)e^{-i\varphi_N} \tag{1-10}$$

where $\varphi_N = [(N-1)\pi\Lambda\sin\alpha]/\lambda$.

Since intensity is defined as $I_{tot} = E_{tot}E_{tot}^*$,

$$I_{tot}\ \alpha \underbrace{\left(\frac{\sin\left[\frac{\pi\Lambda\sin\alpha}{2\lambda}\right]}{\frac{\pi\Lambda\sin\alpha}{2\lambda}}\right)^2}_{Term\ A} \underbrace{\left(\frac{\sin\left[\frac{N\pi\Lambda\sin\alpha}{\lambda}\right]}{\sin\left[\frac{\pi\Lambda\sin\alpha}{\lambda}\right]}\right)^2}_{Term\ B} \underbrace{cos^2\left(\frac{\varphi}{2}\right)}_{Term\ C} \tag{1-11}$$

Term A in the equation above is for a single finger while term B is for a set of either moving or stationary grating fingers. Term C accounts for the phase difference. Terms A and B are plotted in figures Figure 1.7 and Figure 1.8 respectively for $\Lambda = 100$μm and $\lambda = 10$μm.

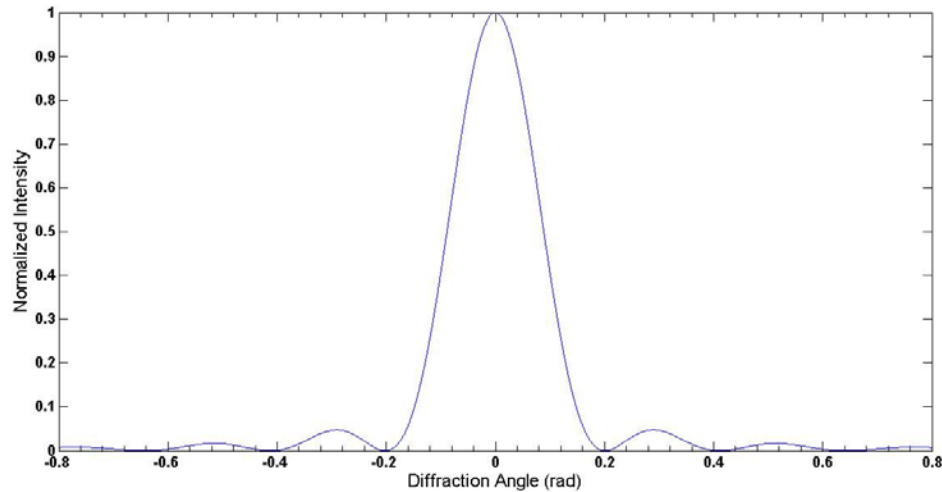

Figure 1.7 Term A of equation (1-11) for $\Lambda = 100\mu\text{m}$ and $\lambda = 10\mu\text{m}$.

For even m values except for zero, term A becomes zero. Therefore, even orders do not exist in lamellar grating interferometers. Constructive interference occurs when the second term is at maximum, for which the denominator should be equal to zero. Thus the equation below must hold where m is an integer.

$$\frac{\pi\Lambda \sin\alpha}{\lambda} = m\pi \tag{1-12}$$

This brings us to the grating equation where m is defined as the order of interference.

$$m\lambda = \Lambda \sin\alpha \tag{1-13}$$

Angular order separation can be calculated by using the equation above.

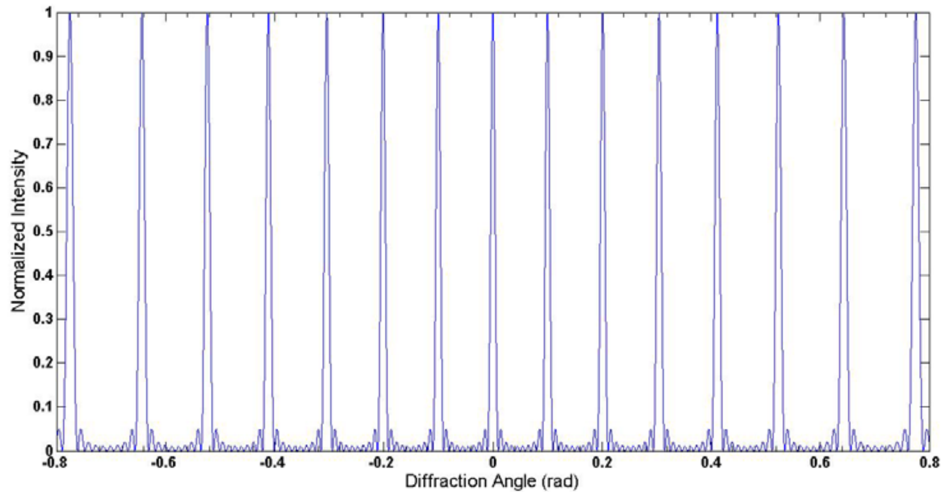

Figure 1.8 Term B of equation (1-11) for $\Lambda = 100\mu\text{m}$ and $\lambda = 10\mu\text{m}$.

The multiplication of terms A and B gives the actual order positions and relative intensity values.

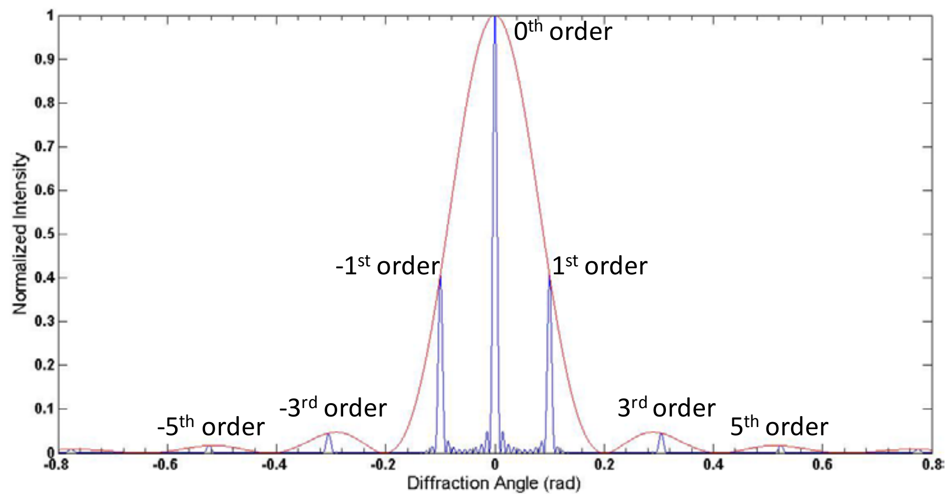

Figure 1.9 Multiplication of terms A and B of equation (1-11) for $\Lambda = 100\mu\text{m}$ and $\lambda = 10\mu\text{m}$.

Term C in equation (1-11) inserts the deflection dependent phase difference into the formula. There is a $\pi/2$ phase difference between the 0th and the odd diffraction orders which can be clearly observed in Figure 1.10 (a).

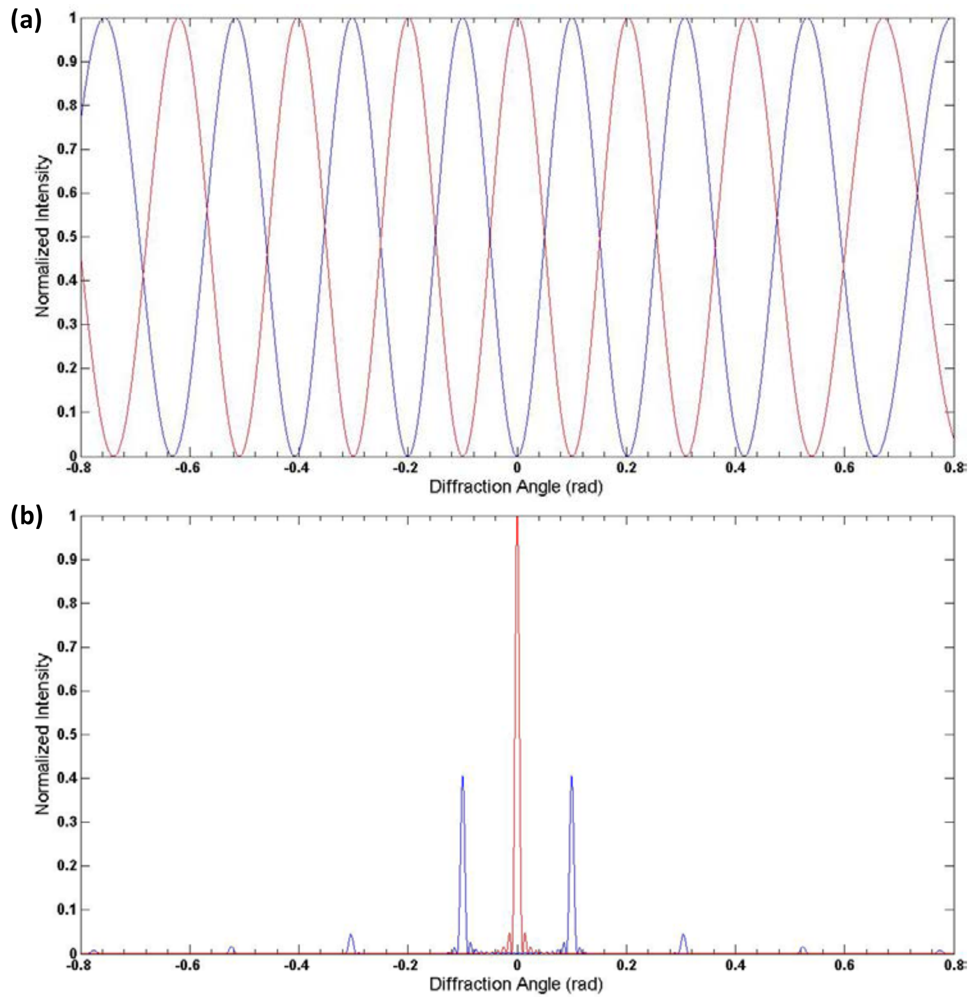

Figure 1.10 (a) Term C for $d = \lambda/4$ (blue) and $d = \lambda/2$ (red). (b) Multiplication of all terms for $d = \lambda/4$ (blue) and $d = \lambda/2$ (red).

Since the 0th order's position is independent of the parameters and has the highest intensity compared to the odd orders of which the position is changing according to the wavelength and the intensity is lower than half of the 0th, the 0th order is used in lamellar grating interferometers. The working principle is summarized in Figure 1.4 (b).

1.3 MEMS-based LGI Devices in the Literature

The lamellar grating interferometer was first introduced in MEMS literature by O. Manzardo [9]. The device was electrostatically actuated with a maximum optical path difference of 145µm. The size of the lamellas in one dimension was limited by the thickness of the wafer, therefore, the aperture area and light collection was quite limited. The technology was commercialized by ARCoptix (www.arcoptix.com), Switzerland as a fiber-coupled FTIR system. It had an optical path difference of more than 1mm corresponding to a resolution of $8cm^{-1}$ which works in 2-4.5µm wavelength range [10], Figure 1.11.

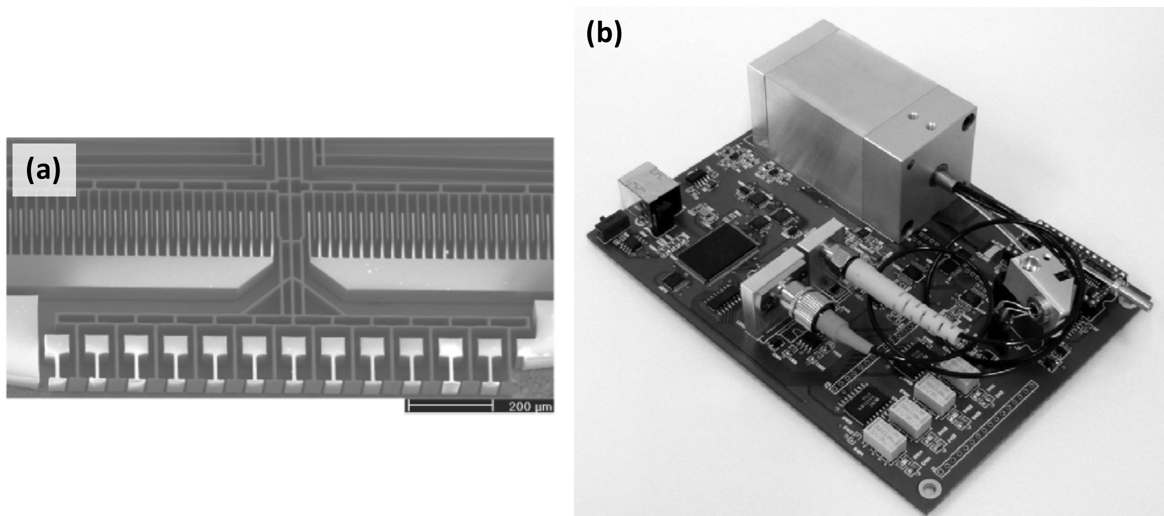

Figure 1.11 (a) LGI MEMS device by O. Manzardo [9]. (b) ARCoptix spectrometer installed on an electronic board [10].

Our group developed the first large clear aperture electrostatically actuated lamellar grating interferometer MEMS device with 106µm peak-to-peak out of plane deflection [11]. The device shown in Figure 1.12 used the top surface of the wafer. Further details are explained in the following section.

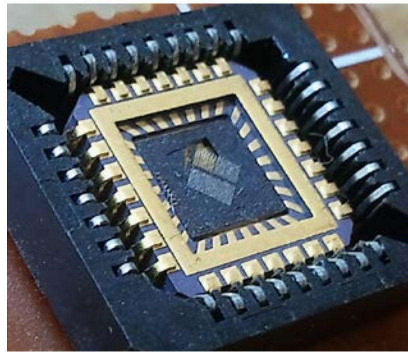

Figure 1.12 LGI MEMS device by KOC University.

Another lamellar grating based spectrometer is reported by National University of Singapore in [12] and [13], Figure 1.13 (a). The MEMS is actuated electromagnetically and works in the resonance mode according to the latter publication. A maximum deflection of ±62.5µm is achieved. The same group later introduced an improved device that moves 100µm bidirectional with electrostatic actuation Figure 1.13 (b).

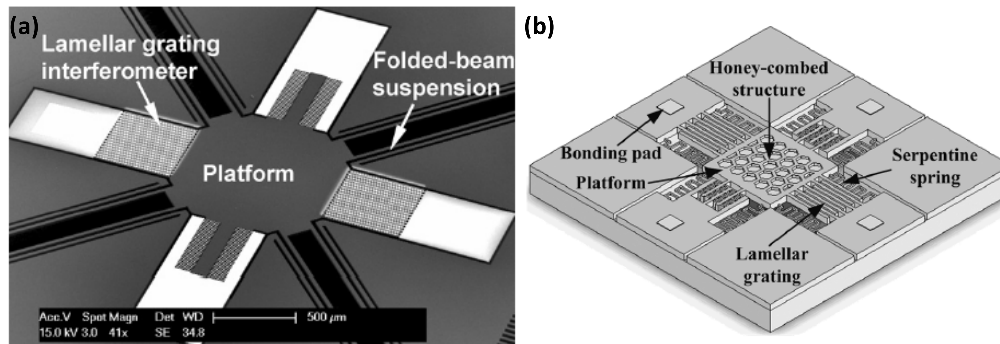

Figure 1.13 LGI MEMS devices by National University of Singapore with (a) electromagnetic actuation [12] and (b) electrostatic actuation [14].

1.4 LGI MEMS Devices Developed at KOC

LGI MEMS devices developed at KOC University are parametrically excited systems based on electrostatic comb actuation. Electrostatic comb actuation is a widely used actuation method in MEMS for not only translational but also rotational and in-plane motions. The oscillation of comb actuated devices depends on the excitation frequency and the eigenmode of the structure [15].

The coefficients of the equation of motion are time dependent in parametrically excited systems. Such systems exhibit multiple resonances, hysterical frequency response and subharmonic oscillations. A small parametric excitation can produce a large response when frequency of the excitation is close to twice the natural frequency of the system. Thus, the excitation signal frequency should be around twice the mechanical eigenmode frequency in order to obtain maximum deflection from the device. As a result, LGI MEMS devices are designed such that the excitation frequency is double the vibration frequency and other modes are shifted such that they are not at integer fractions of double the excitation frequency [11], [16], [17].

Note that LGI MEMS devices are symmetric structures, hence they do not respond to DC actuation. They are driven with square waves instead of sinusoidal to maximize the power delivered to the system. An experimental comparison of square and sinusoidal excitation will be provided in Chapter 2.

Developing an LGI based FT spectroscopy was an ongoing project before MEMFIS project started. The two main MEMS designs completed at Optical Microsystems Laboratory that share the properties described above with different spring designs are explained in [18] and [19] in detail. In this thesis the latter design is characterized and used in the spectrometer system integration.

1.4.1 LGI Design with Serpentine Springs

The first design developed by Dr. Çağlar Ataman has a rectangular grating area and the moving set of fingers is connected to the substrate by 45° serpentine springs on each corner as shown in Figure 1.14.

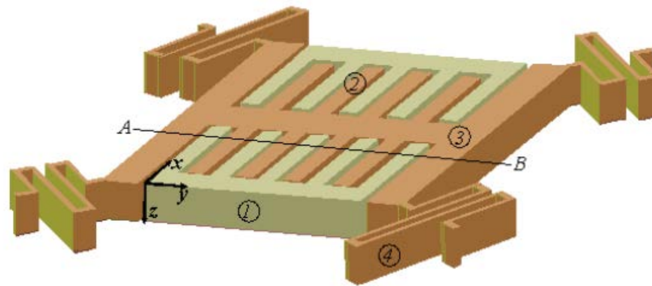

Figure 1.14 LGI MEMS design with serpentine springs. (1) Stationary grating fingers. (2) Moving grating fingers. (3) Rigid backbone. (4) Serpentine springs.

Grating fingers are used for both interferometric and actuation purposes. In order to increase the robustness and keep the dynamic deformation at an acceptable level, the moving grating fingers are placed on a rigid backbone. Grating period is optimized for high optical efficiency and good order separation. The fingers are coated with 100nm aluminum to enhance the reflectivity for infrared illumination. Serpentine springs are designed with varying cross-sectional width to attain uniform stress distribution and low stiffness.

The device is designed such that out-of-plane mode is the first mode, while the closest mode is kept around 1.5 times higher frequency. The maximum stress is simulated as 1.25GPa at the corner of the serpentine springs.

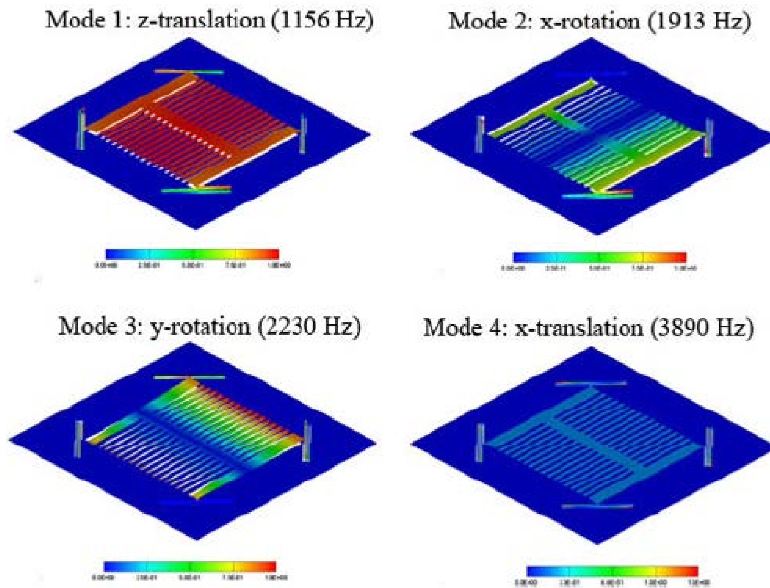

Figure 1.15 First four natural oscillation modes of LGI with serpentine springs.

The device was fabricated by Fraunhofer IPMS on a 30µm thick SOI wafer. An experimental deflection of ±53µm is obtained with 28V sinusoidal excitation.

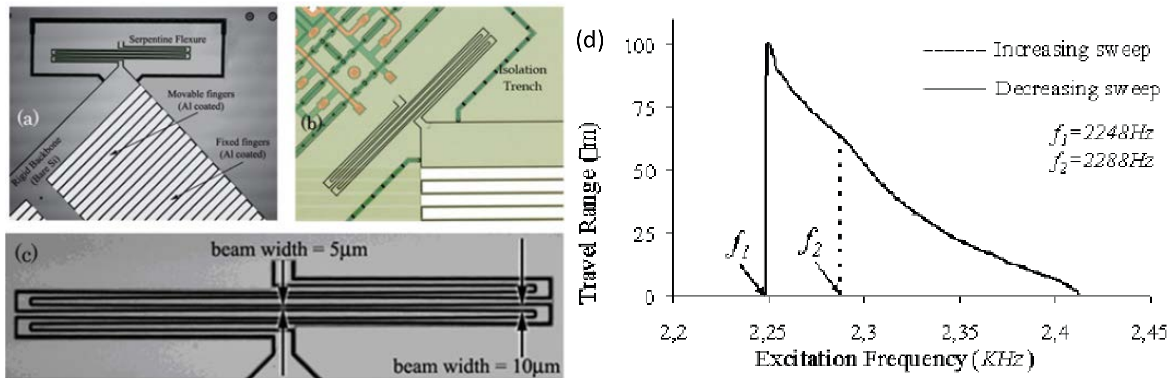

Figure 1.16 (a)-(c) Microscope images of the fabricated device. (d) Frequency response with 28V sinusoidal excitation.

1.4.2 LGI Design with Pantograph Springs

In this approach, pantograph type of springs as originally introduced by Fraunhofer IPMS are used [20], [21]. Pantograph springs translate torsional bending into translational motion with higher deflection compared to flexure bending. Two prototypes using pantographs are designed by Hüseyin R. Seren and fabricated by Koc researchers.

In the first prototype, a rectangular grating area (2.5mmx5mm) including a 0.5mm wide backbone is used. Instead of one spring, two parallel torsional springs on each side are used in order to increase the overall stiffness of the system while keeping soft springs that can handle torsional bending. The first mode is designed as out-of-plane at 500Hz. The first four modes are given in Figure 1.18.

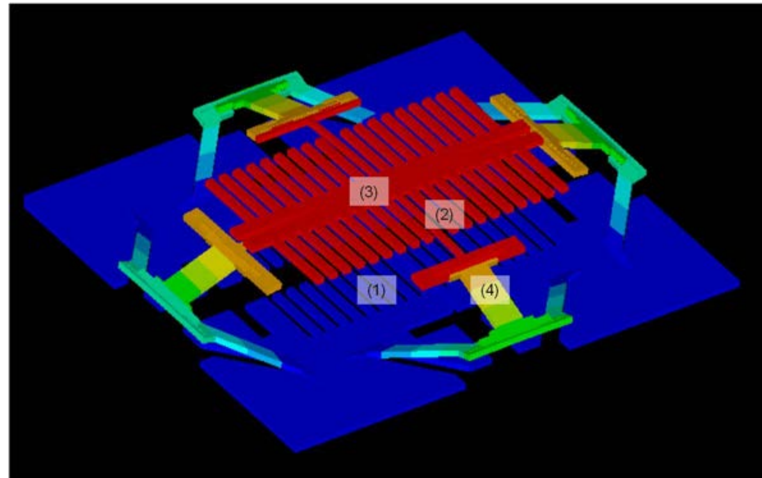

Figure 1.17 LGI MEMS design with pantograph springs (1st prototype). (1) Stationary grating fingers. (2) Moving grating fingers. (3) Rigid backbone. (4) Pantograph spring.

Maximum stress for 533µm deflection is simulated as 1.44GPa which is within the stress limits of silicon. Mechanical stops are added around torsional springs to avoid fracture. Dynamic deformation as well as static bending is an important factor determining the optical efficiency. The limit for deformation is λ/2 where a destructive interference

occurs and degrades the interferogram. Also, a beam reflecting off a bent structure diverges, which as a results decreases optical throughput. The MEMFIS project requirement for dynamic deformation is set as λ/10 as a rule of thumb, which is equal to 250nm for the shortest wavelength in the mid-IR range. In this design, dynamic deformation is reduced to 300nm at the intended maximum deflection along the grating fingers by introducing deformation absorbing suspensions.

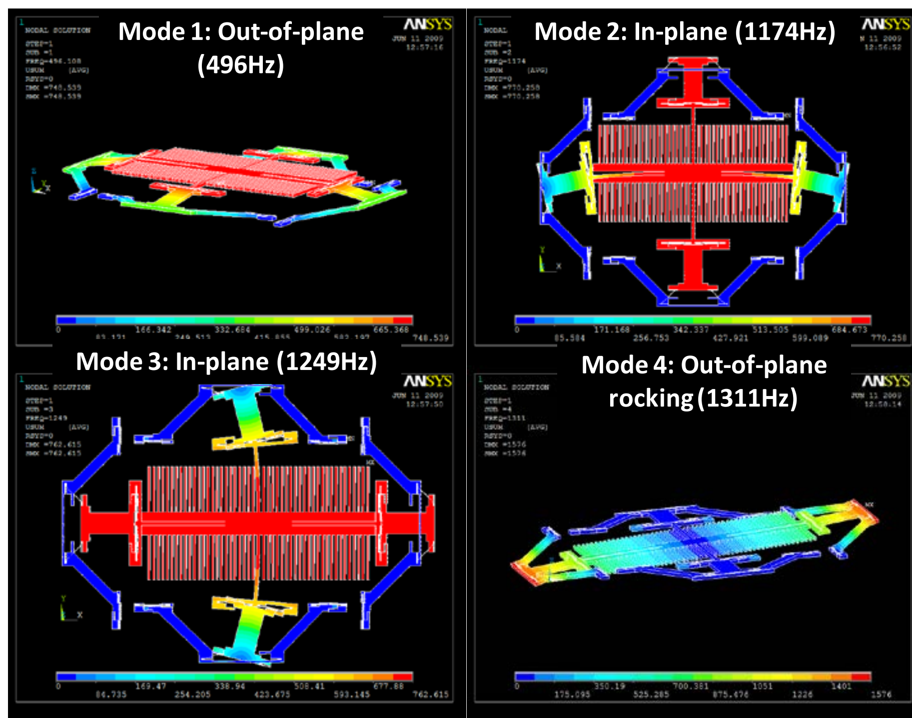

Figure 1.18 First four natural oscillation modes of LGI with pantograph springs (1st prototype).

In the second prototype, the grating area is converted from a rectangular shape to a diamond shape to lower the dynamic deformation even further. Actually the grating area should be close to a circular shape to adjust with the remaining optical components, which are circularly shaped. The reason for using a diamond shaped grating was the fact that a

higher dynamic deformation was observed on the outer fingers compared to the ones closer to the center. Active area is decreased to 9.6mm^2 approximately. Also, a more curved pantograph spring is introduced Figure 1.19.

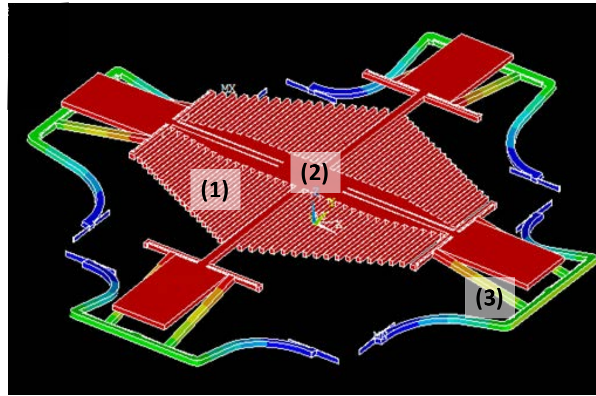

Figure 1.19 LGI MEMS design with pantograph springs (2nd prototype). (1) Moving grating fingers. (2) Rigid backbone. (3) Pantograph spring.

The first mode is out-of-plane at 462Hz. The closest rocking mode is shifted 2.5 times away. First four modes are summarized in Table 1.2.

Mode Number	Resonance Frequency (Hz)	Mode Shape
1	462	Out-of-Plane
2	1160	Rocking
3	1183	Rocking
4	1422	Pantograph Out-of-Plane

Table 1.2 First four natural oscillation modes of LGI with pantograph springs (2nd prototype).

Dynamic deformation at maximum deflection is reduced to 230nm by using variable grating finger length and a non-rectangular backbone. A maximum stress level of 1.1GPa is obtained at the corner of the torsional spring.

Both mechanical and optical characterization of the two latter designs will be investigated in the next chapter in detail.

1.5 Contributions of the Thesis

Main contributions of this thesis are in the methods and apparatus developed for optical and mechanical characterization of MEMS-based LGI devices and in system design and integration to demonstrate an FTIR system based on MEMS devices.

Two separate LGI MEMS designs with pantograph type of suspensions are characterized both mechanically and optically using automated characterization setups and two new actuation methods are introduced to test the existing designs without requiring electrical connections to the device. A miniaturized IR source and IR detector developed within the MEMFIS project by our partners are used for system testing. A fully functional LGI based FTIR spectrometer system is demonstrated on an optical table and successfully benchmarked with other FTIR systems for the first time within our group. The optical system analysis and optimizations are performed using both physical optics simulations (in MATLAB) and ray tracing simulations (in ZEMAX).

Chapter 2 explains the automatized mechanical characterization methods and test results. Electrostatic actuator has nonlinear response and has some inherent problems: electrostatic stiction and pull-in problems limit the actuation voltages to about 70V, which in turn limit the maximum achievable displacement and the spectral resolution. Two alternative actuation methods are tried in this research: acoustic excitation using a speaker and mechanically-coupled excitation using a piezoelectric-vibrator, which worked well and improved the mechanical deflection and allowed us to test devices without requiring wire-bonding. In Chapter 3, optical characterization work using a fringe counting setup and Labview based controller is described in detail. In the fourth chapter, the theory and

limitations of LGI are explained. The system analysis and optimization are performed using (i) physical optical simulations using Fresnel beam propagation method and (ii) ray-tracing analysis in ZEMAX optical design software. The system integration and sample measurements with detailed data analysis are investigated in Chapter 5. Also a possible application of LGI, thin film thickness measurement is explained in this chapter. Finally, the thesis is summarized in the conclusion chapter.

2 MECHANICAL CHARACTERIZATION

In this chapter, the mechanical characterization results of the LGI MEMS devices are provided. For fast and reliable testing, two automatized systems based on laser Doppler vibrometry and laser fringe counting are developed in Labview. Devices fabricated in five separate fabrication runs are mechanically characterized using these systems. Also, the effect of the driving signal's shape is experimentally investigated. Finally, two alternative actuation methods with sound pressure and piezoelectric-vibrator are introduced in addition to electrostatic actuation.

Devices are wirebonded on specifically designed and fabricated PCBs as shown in Figure 2.1 (a) to ease the handling of MEMS and to avoid electrical connection problems during characterization and system integration. The center of these PCBs where the moving part of the MEMS resides on is intentionally left blank to avoid air damping. The pins on the sides of the PCB are connected to certain pads which are wirebonded to the electrical connection pads on the MEMS device. This board with MEMS on it is mounted on another PCB as given in Figure 2.1 (b) with a hole in the center and pins and female headers on the upper and lower sides for electrical connection. This PCB is designed such that the pins in the middle row of three-row sets on both the upper and lower parts are connected to the headers one by one. Every five pins of the rest of the rows are shorted and a row on the upper part is connected to another row on the lower part. The same is applied to the remaining two rows. A pin in the middle row can be connected to the upper or the lower row with the help of a jumper. As a result two separate voltage levels can be applied to the MEMS device according to the position of the jumper.

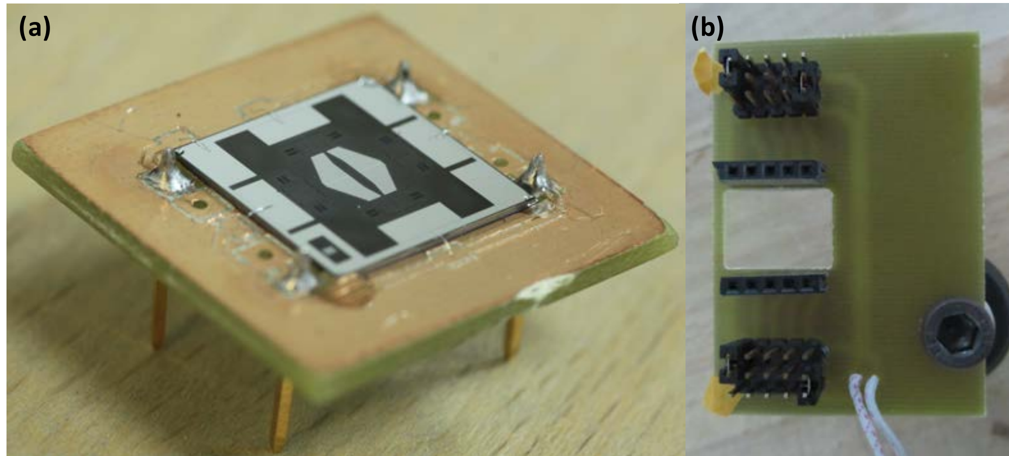

Figure 2.1 (a) MEMS device mounted on specifically designed PCB. (b) PCB designed for MEMS testing.

MEMS mirrors in an FTIR spectrometer must avoid mode coupling and sustain dynamic deformation at tolerable levels. Optical path difference (OPD), which is double the deflection of an LGI MEMS device, defines the resolution of an FTIR spectrometer as described in the following chapter among other factors such as incidence angle of IR beam on the grating, mode coupling and dynamic deformation. In order to be able to use the MEMS device as the interferometer part of an FTIR spectrometer, frequency and voltage responses are obtained.

2.1 Mechanical Characterization Methods

MEMS devices are mechanically characterized by both laser Doppler vibrometer and a custom built fringe counting based setup.

2.1.1 Laser Doppler Vibrometry Setup

A laser Doppler vibrometer (LDV) measures the velocity and deflection based on the Doppler effect; sensing the frequency shift of back scattered light from a moving surface.

The instrument is composed of an interferometer and an acousto-optic modulator (Bragg cell) to detect both the amplitude of the movement and the direction of it. A HeNe laser is used as the light source which limits the theoretical resolution to half the wavelength, 316nm. However, Polytec laser Doppler vibrometers are claimed to have an improved resolution of 2nm with the help of suitable interpolation techniques.

For the measurements, Polytec OFV-2500 vibrometer controller and OFV-534 sensor head are used. A Labview program is prepared for controlling the instruments and plotting the output. The automatized setup is shown in Figure 2.2. The device is actuated with a square wave of 50% duty cycle with half of its amplitude given as offset. The sinusoidal vibration at half the excitation frequency is measured by the oscilloscope and sent to the computer.

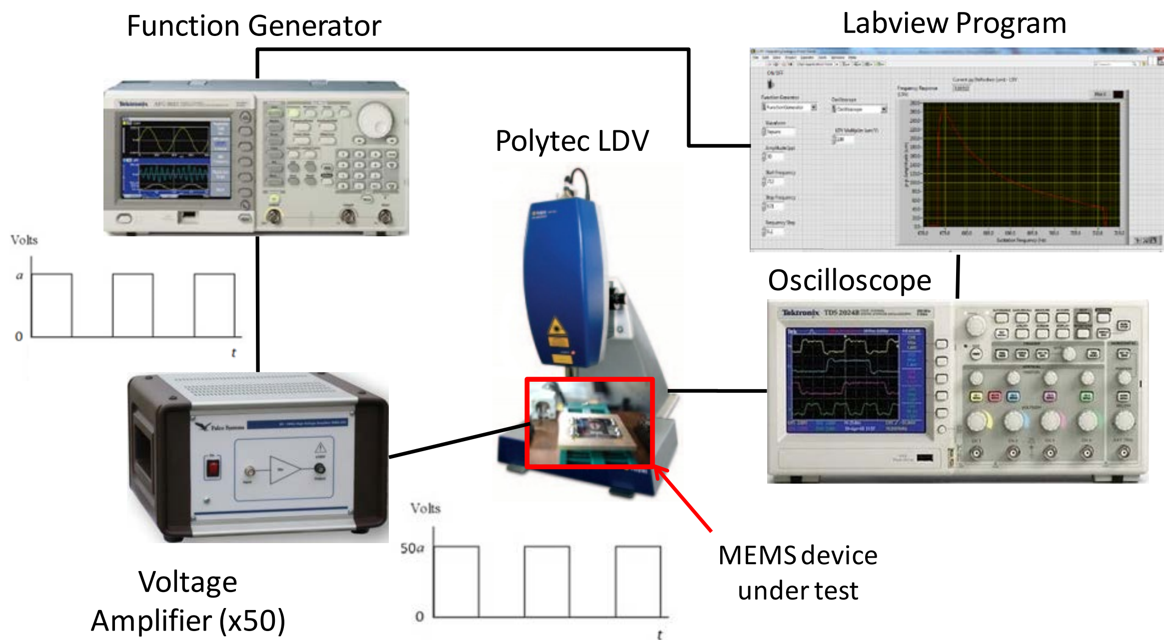

Figure 2.2 Mechanical characterization setup with laser Doppler vibrometer.

The left part of the program controls the function generator. Waveform, start and stop frequencies, frequency step and the applied voltage can be set via this part. The switch on the corner is for turning the channel on and off. The middle part is in charge of the LDV. Since this is a passive system in terms of vibrometer control, only the LDV multiplication factor, which is already set in the instrument is entered by the user. Lastly in the rightmost part, excitation frequency vs. p-p deflection curve is plotted. Current p-p deflection value is printed on the screen at each frequency.

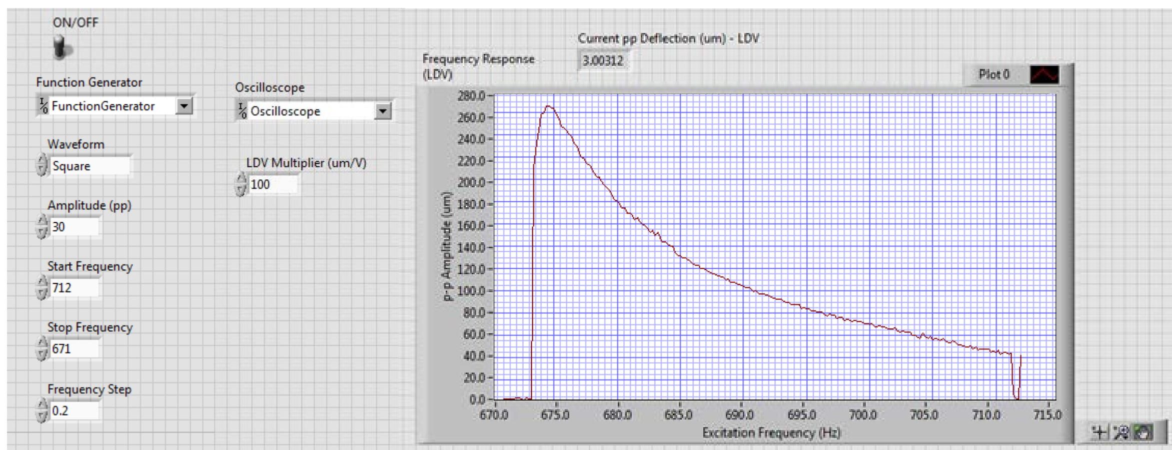

Figure 2.3 Front panel of laser Doppler vibrometer based Labview program.

The whole program runs in a while loop which is terminated if the stop frequency is equal to the frequency at that time. The program waits for 5000ms at each step, which can be set as a constant on the upper right-hand side. Voltage amplitude is calculated assuming that an amplifier with a gain of 50 is used. So; if the user enters 30V as the input voltage, the program divides it by 50, sends the result to the instrument as amplitude and uses half of this result as offset. At each cycle, the displacement output of LDV is sent to the oscilloscope. The peak-to-peak voltage measured in the oscilloscope is sent to the computer and multiplied with the LDV multiplication factor entered by the user. The

current frequency and corresponding p-p amplitude is plotted on the screen until the loop is terminated.

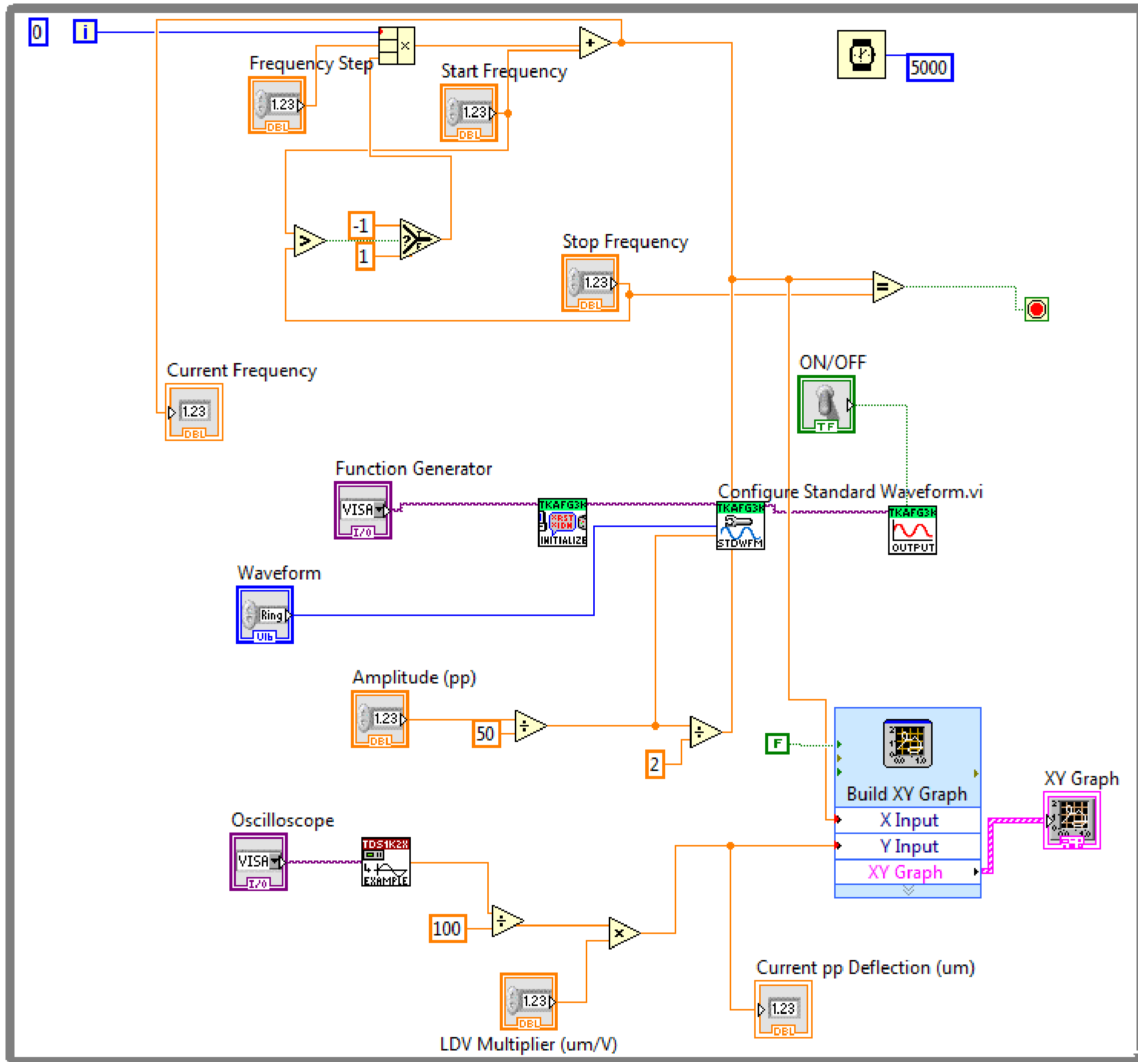

Figure 2.4 Block diagram of LDV based Labview program.

2.1.2 Laser Fringe Counting Setup

The laser fringe counting setup relies on the interferometric nature of the MEMS device. Stationary and moving grating fingers act as an interferometer by creating optical path difference thus resulting in constructive and destructive interference patterns at well defined distances in terms of wavelength of the illumination. The deflection of moving grating fingers can be calculated using this distance since optical path difference and deflection are directly related.

In the setup, a square voltage signal is generated in the function generator and then sent to the amplifier. The amplified signal is used for exciting a device that is wirebonded and mounted on a PCB. In the optical setup, a red HeNe laser with 632.8nm wavelength is directed at the MEMS device as given in Figure 2.5.

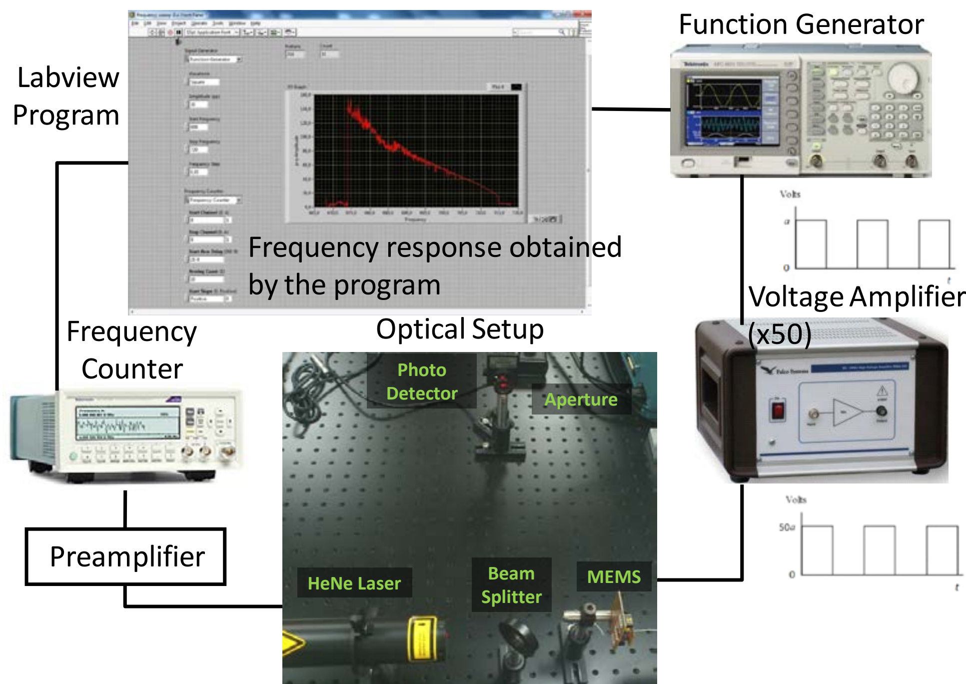

Figure 2.5 Fringe counting based mechanical characterization setup.

On the way, it passes through a beam splitter at 45° angle. After the beam is reflected from the device, it goes through the beam splitter again and gets imaged onto the detector. An aperture is used for blocking orders other than the 0th order. (Figure 2.6) The output of photodetector is a chirped sinusoidal signal, which is made up of fringes. After DC cancellation, the signal is amplified if needed and then sent to the frequency counter, which is set to work in count event mode in order to count fringes. In the Labview program, these instruments are controlled from the computer and excitation frequency vs. p-p deflection curve is plotted by multiplying the number of fringes with half of the wavelength of the laser used.

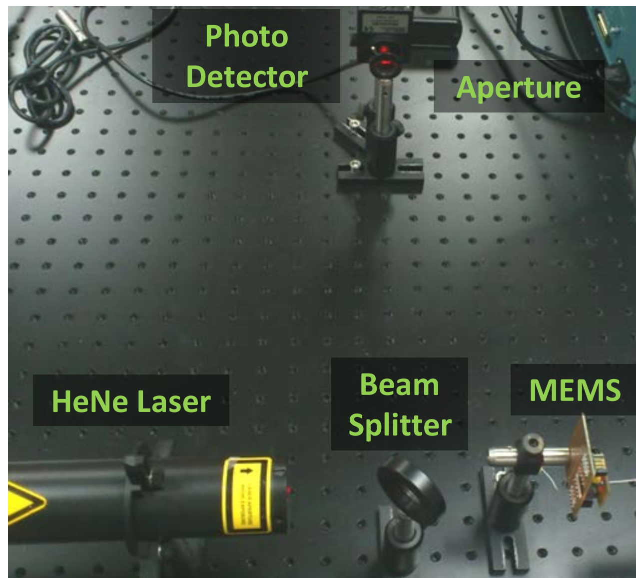

Figure 2.6 Optical part of laser fringe counting setup.

The front panel of the laser fringe counting based Labview program is given in Figure 2.7. The left part of the program controls the function generator. Waveform, start frequency, stop frequency, frequency step and the applied voltage can be controlled via this part. The switch on the corner is for turning the channel on and off.

The part in the middle of the program is in charge of the frequency counter. Start and stop channels are used for triggering purposes. Channel B is chosen for both of them for which a 5V p-p square signal with the same frequency as the input voltage is applied. Also, start and stop slopes are set as positive, meaning that the measurement is done in one period of the input voltage. (Setting both of them as negative will work as well.) If excitation at $f_{vibration}$ instead of $2f_{vibration}$ is used, which is the case in speaker actuation, start and stop slopes should be set as positive and negative respectively or vice versa. 20ns is used as start channel delay, which is the smallest possible value.

Last part on the right-hand side of the program is the frequency response curve.

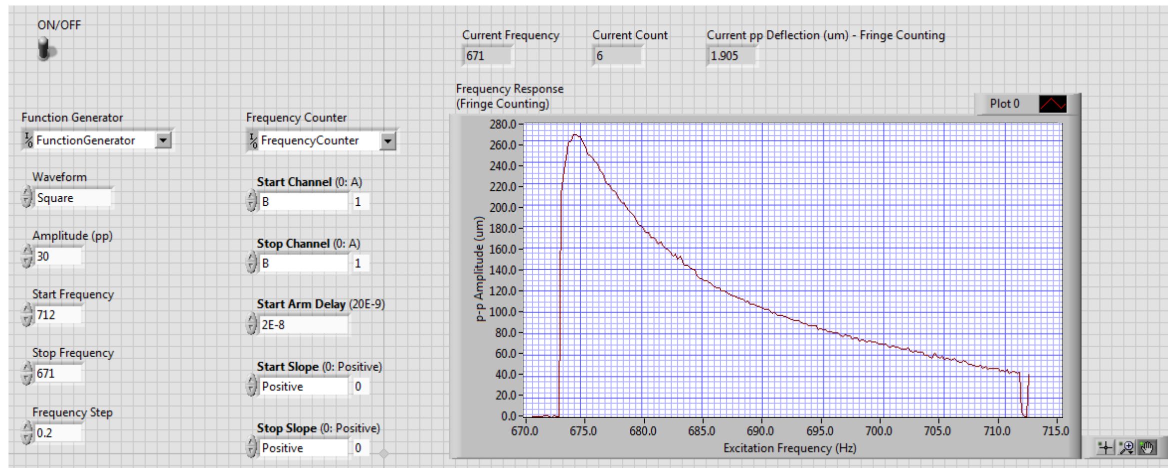

Figure 2.7 Front panel of laser fringe counting based Labview program.

Below is the block diagram of laser fringe counting based Labview program (Figure 2.8). The program runs in a while loop as explained before for LDV based system. The upper part controls the function generator, while the lower controls the frequency counter and plots the graph of excitation frequency (Hz) vs. p-p deflection (μm). In "FCA Counter" block, the frequency counter is set to work in the event count mode as default.

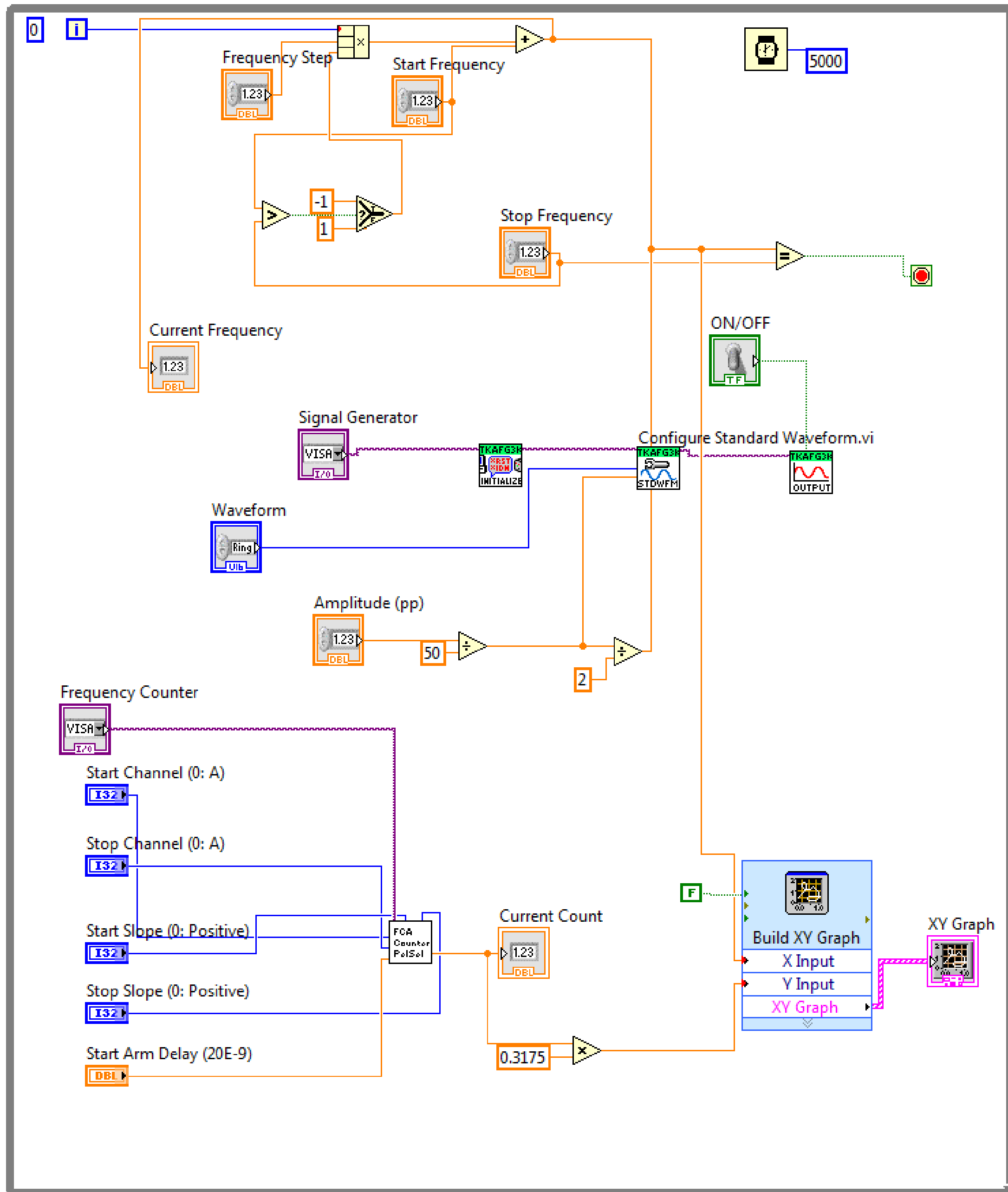

Figure 2.8 Block diagram of laser fringe counting based Labview.

These two systems are compared by integrating two separate programs in one Labview program and combining the optical setups as given in Figure 2.9. Since resonant behavior changes in terms of deflection and frequency according to how the device is mounted, the comparison is made by capturing the data simultaneously. A vertically mounted MEMS device is illuminated by the LDV from the front side and by the HeNe laser from the backside. The deflection is captured simultaneously from both systems and plotted on the same graph as in Figure 2.10. It is obvious from this data that the fringe counting setup works as good as LDV if the optical alignment is done properly. However, at large deflections the fringe pattern deteriorates, which results in fluctuations in measurement.

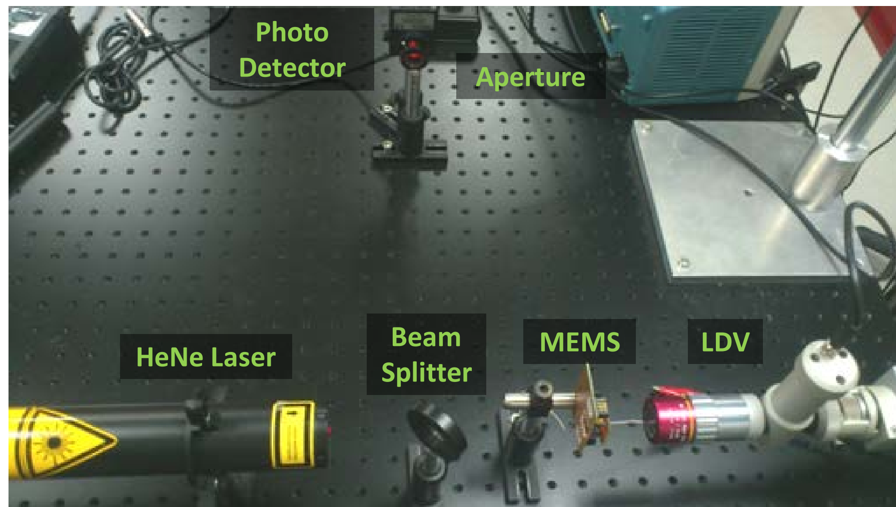

Figure 2.9 Optical setup for comparison of laser fringe counting and LDV based systems.

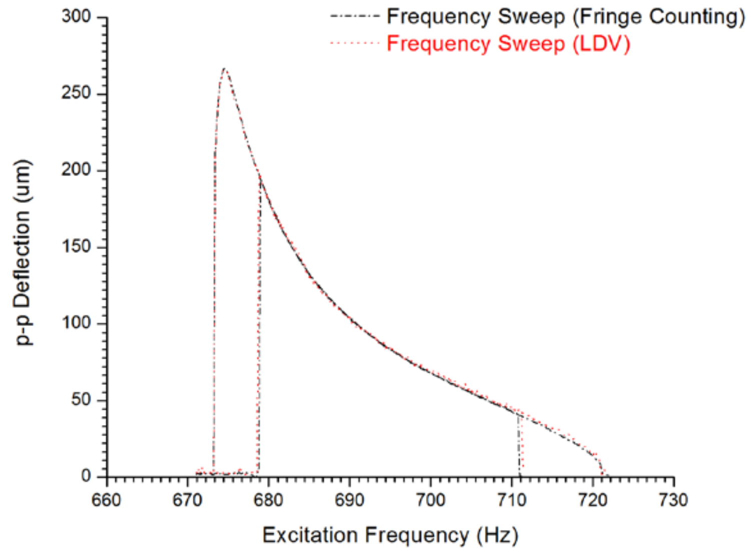

Figure 2.10 Frequency sweeps obtained from both laser fringe counting and LDV based systems simultaneously.

2.2 Mechanical Characterization Results

The two prototypes introduced in section 1.4.2 are fabricated by both OML researchers at EPFL and Fraunhofer IPMS, one of our MEMFIS project partners. Design variations and fabrication runs are summarized in Table 2.1 and Table 2.2.

	Design name	**Grating period (µm)**	**Die size (mm^2)**
Prototype 1	**LGI_D1**	60	11x11
	LGI_D2	80	
	LGI_D3	100	
	LGI_D4	30, 50, and 130 (variable)	
Prototype 2	**LGI_D5**	130	13x13

Table 2.1 Design variations.

Fabrication run	Designs included	Remarks
FabRun 1_KOC (fabricated by KOC researchers at EPFL)	LGI_P1_Koc_D1 LGI_P1_Koc_D2 LGI_P1_Koc_D3 LGI_P1_Koc_D4	
FabRun 1_IPMS	LGI_P1_IPMS_D1 LGI_P1_IPMS_D2 LGI_P1_IPMS_D3 LGI_P1_IPMS_D4	Same designs as above; masks are different due to Stepper used at IPMS.
FabRun 2_IPMS	LGI_P1_IPMS_D1 LGI_P1_IPMS_D2 LGI_P1_IPMS_D3 LGI_P1_IPMS_D4	**Same masks as previous IPMS run, dicing problems solved to improve yield.** *Pull-in is observed in grating fingers at 50V. The input voltage could be increased up to 60V if comb fingers are used for actuation only. At 70V, comb fingers are burnt.
FabRun 2_KOC	LGI_P2_Koc_D4 LGI_P2_Koc_D5	**Au is replaced by Al.** All comb-finger corners are rounded. **The D5 five devices with improved mechanical design are fabricated for the first time.**
FabRun 3_KOC	LGI_P1_Koc_D3 LGI_P1_Koc_D4 LGI_P2_Koc_D5 (T3/T4)	**Reduced Al thickness on grating fingers to reduce static deformation.** Two different types of D5 devices are made: T3 and T4. In T3 the static grating fingers are shorted with the moving part to easier avoid grating finger pull-in.

Table 2.2 LGI MEMS device fabrication summary.

The devices fabricated in FabRun 1_KOC were initially characterized using electrical probes in ambient pressure. Maximum peak-to-peak deflection observed at the center of the device is 400µm with 80V input voltage. Both excitation and vibration frequency is around f=550Hz. Excitation at 2f resulted in coupling with a rocking mode. Most of the devices suffered from short circuit and got broken during characterization. Limited mechanical characterization data acquired in ambient pressure is shown in Figure 2.11.

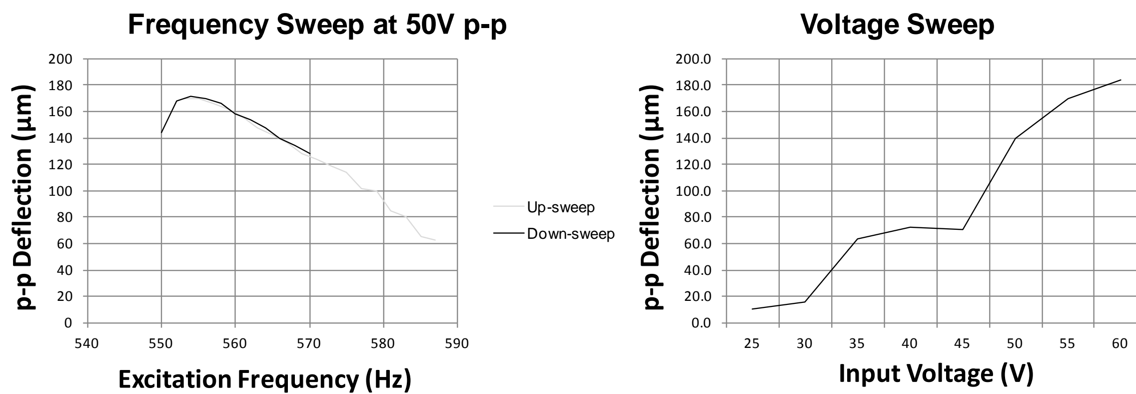

Figure 2.11 Mechanical characterization results of FabRun 1_KOC.

For vacuum testing, where the air damping effect is avoided, the devices were wirebonded at Bogazici University since the wire bonding machine in our laboratory was not functional at that time. A maximum peak-to-peak deflection of 600µm is obtained at 60mTorr with an excitation voltage of 42V.

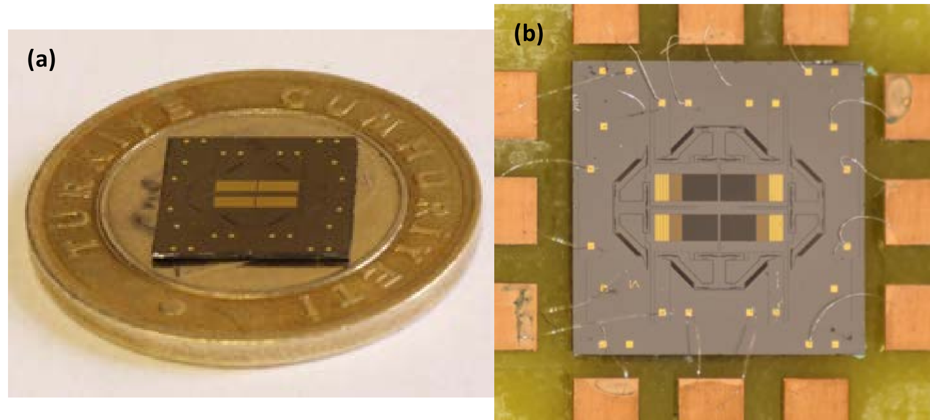

Figure 2.12 (a) A bare LGI MEMS device from FabRun 1_KOC on a coin. (b) Wirebonded device.

Devices fabricated in this run had problems such as early comb finger pull-in, fragile flexures, mode coupling and low metal quality. The design and layout were accordingly updated for the following fabrication runs.

The same design is also fabricated by Fraunhofer IPMS twice. The devices obtained from FabRun 1_IPMS were mechanically characterized and the results were presented in [22]. These devices only worked in vacuum and a maximum peak-to-peak deflection of 355µm was achieved with an input voltage of 76V at 0.15mTorr (=20mPa). The excitation was double the vibration frequency of 485.5Hz. SEM picture of a pre-deflected device and a frequency sweep at 62V input voltage is given in Figure 2.13.

Only two out of four comb finger sets were used in these experiments since wirebonding was done so. Deflection was expected to be higher if all comb fingers were used for actuation. Mode coupling was not observed and 2f excitation was achieved. However, ambient operation was not possible.

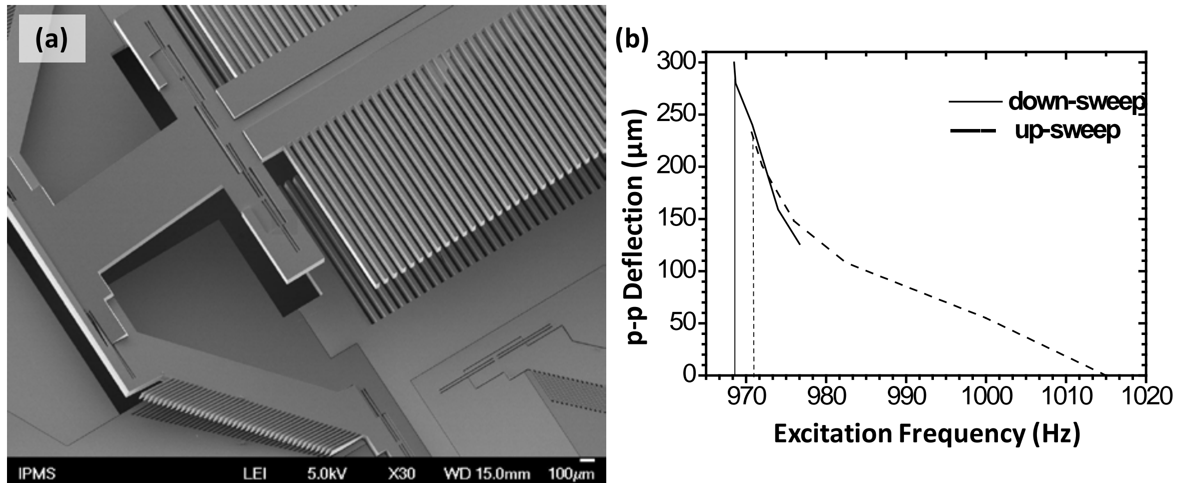

Figure 2.13 (a) SEM picture of a pre-deflected LGI MEMS device from FabRun 1_IPMS. (b) Frequency response at 62V input voltage.

Later, Fraunhofer IPMS made another fabrication run for the same design. Mechanical characterization of FabRun 2_IPMS devices was performed by the author during her internship at Fraunhofer, IPMS in Dresden, Germany. A maximum deflection of 320μm peak-to-peak is obtained with 60V input voltage in ambient conditions. The frequency responses for this particular device at various pressures are plotted in the figure below. The movement gets problematic at 1KPa but a maximum peak-to-peak deflection of 440μm is observed 50Pa with 30V input voltage while only 144μm peak-to-peak deflection is obtained with the same voltage in ambient pressure. All comb fingers are used for actuation compared to the characterization of previous fabrication run.

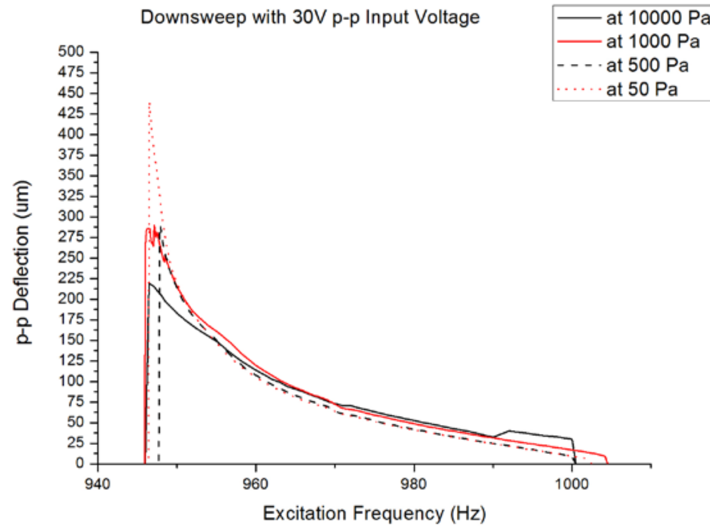

Figure 2.14 Frequency response of an LGI device from FabRun 2_IPMS at various pressures.

In FabRun 2_KOC, the improved design (2nd prototype) discussed in section 1.4.2 was fabricated with aluminum coating on grating instead of gold. The devices exhibited stable vibration at f when excited at 2f. A maximum peak-to-peak deflection of 712µm is achieved at 340Hz with an input voltage of 71V in ambient. However, they suffered from static bending of grating fingers which deteriorates the interference pattern quality substantially.

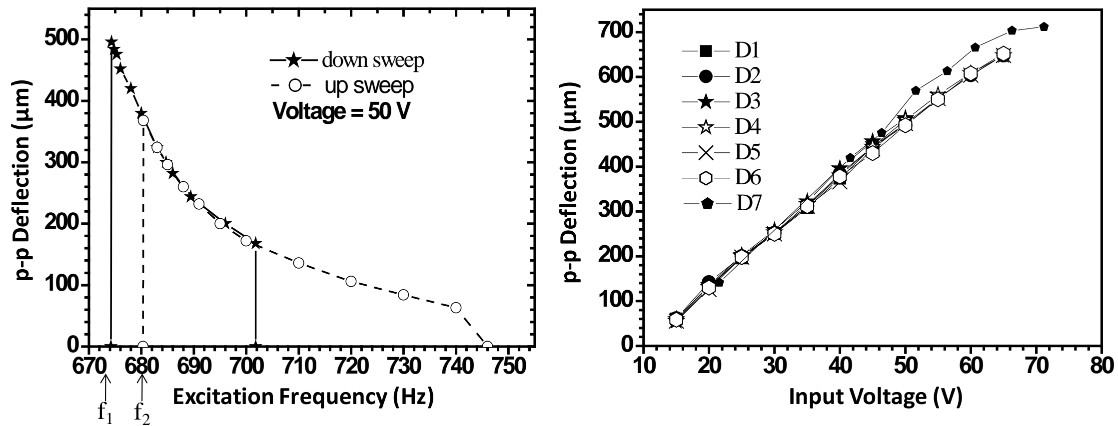

Figure 2.15 Frequency and voltage responses of FabRun 2_KOC devices.

Lastly in FabRun 3_KOC, 2nd prototype devices are fabricated with thinner aluminum coating on grating fingers to avoid static bending. As a result, these devices are decided to be suitable for optical characterization and integration with IR optics [23]. A similar frequency response was obtained from FabRun 3_KOC devices as the previous fabrication run.

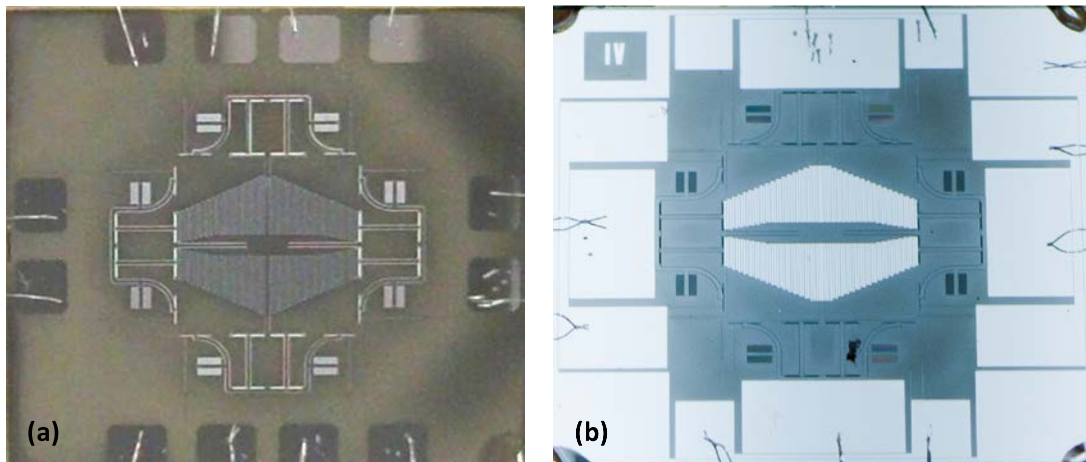

Figure 2.16 LGI MEMS device fabricated in (a) FabRun 2_KOC, (b) FabRun 3_KOC.

The vibration frequency turned out to be lower than the designed value due to thinning of the comb fingers in both prototypes fabricated in FabRun 3_KOC. An extra version of LGI_P2_Koc_D5 was fabricated with additional grating finger actuation option. A larger deflection was expected with grating finger actuation in addition to comb fingers however pull-in was observed at very low voltages.

All the aforementioned mechanical characterization is done by electrostatic actuation applying a square voltage with half of its amplitude applied as offset. A square wave is used instead of sinusoidal because a square wave has more power than a sinusoidal with the same amplitude. This is experimentally shown in the following figure where the device is actuated with a 30V signal and a frequency sweep is performed.

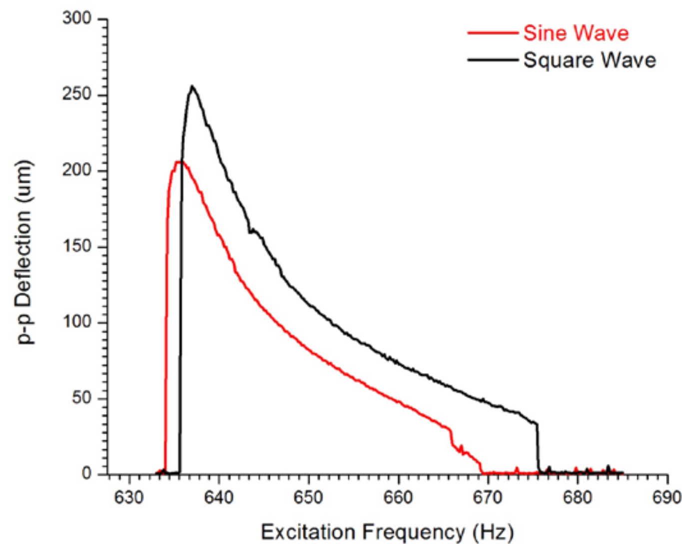

Figure 2.17 Frequency sweeps with square and sine wave actuation, respectively.

Natural oscillation modes of a 2nd prototype device are extracted experimentally. The device is driven with 25V sinusoidal signal to make sure that the device is excited exclusively at the desired frequency. Square wave actuation is intentionally avoided in this experiment since harmonics of a square wave could excite other modes as well.

Mode Number	Resonance Frequency (Hz)	Mode Shape
1	335	Out-of-Plane
2	948	Rocking
3	974	Rocking
4	1322	Pantograph Out-of-Plane

Table 2.3 First four experimental oscillation modes of LGI_P2_Koc_D5 devices.

2.3 Alternative Actuation Methods

The deflection required for $10cm^{-1}$ resolution could not be met with electrostatic actuation. Two different alternative actuation methods are proposed to meet the project specifications: air pressure and piezoelectric-vibrator.

Air pressure actuation is done with the help of a speaker. The device is mounted on the previously described PCB which is placed on the speaker such that the moving part of the MEMS device is located at the center Figure 2.18 (a). The speaker is driven with a sinusoidal signal at the resonance frequency. The system behaves in a more linear fashion with a small spring hardening effect clearly seen in Figure 2.18 (c) while spring softening is dominant in electrostatic actuation shown in the same figure. Spring hardening and softening effects are explained in [24] in detail.

When actuated with speaker a maximum peak-to-peak deflection around 700µm is obtained with LGI_P2_Koc_D5 devices. Deflection is limited by the mechanical stoppers

in the 2nd prototype. LGI_P2_Koc_D3-4 devices on the other hand functions in a stable fashion up to approximately 1mm p-p deflection, while fracture is observed at 1.4mm.

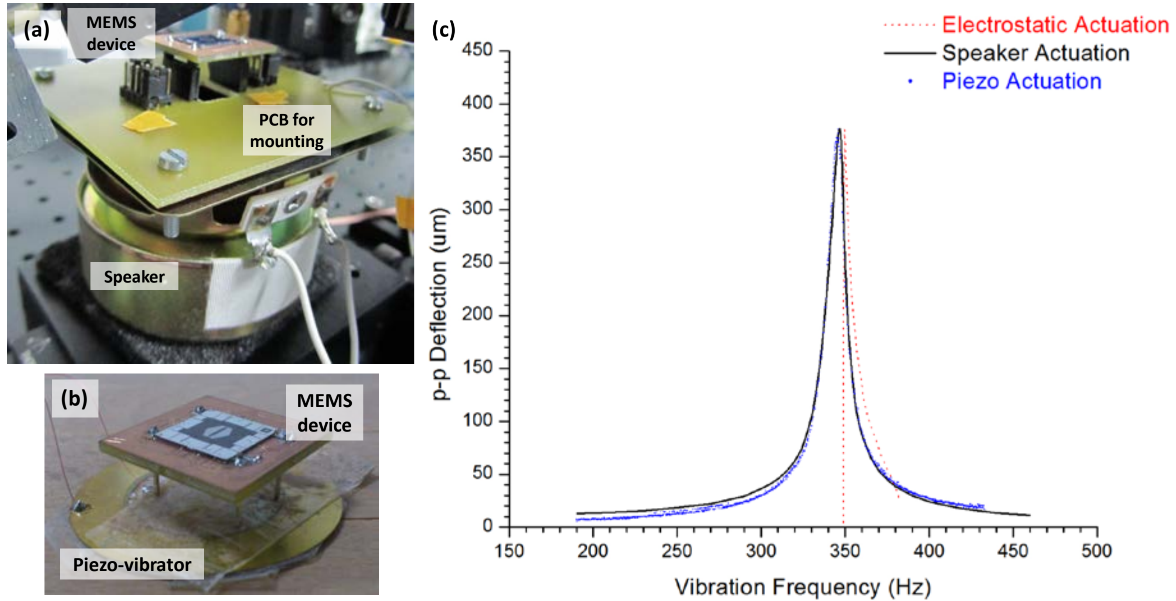

Figure 2.18 (a) Speaker actuation setup. (b) Piezoelectric actuation setup. (c) Frequency responses with all actuation methods.

The second alternative actuation method makes use of piezoelectricity. A piezoelectric material produces a mechanical stress (extracts or contracts) when an electric field is applied or vice versa. If an AC signal is applied, the material vibrates at the excitation frequency. Actuation with piezoelectric-vibrator is done by mounting the device on the vibrator with a double sided tape in-between (Figure 2.18 (b)). A sinusoidal signal without offset at the resonance frequency is applied to the piezoelectric material and a frequency response very similar to speaker actuation is obtained (Figure 2.18 (c)). Note that some space is left intentionally between the MEMS device and piezoelectric-vibrator to avoid air damping.

3 OPTICAL CHARACTERIZATION

It was stated in the previous chapter that factors such as optical path difference and the incidence angle of the source determine the resolution in FTIR spectrometers. In this chapter, these factors are firstly formularized and then experimentally observed using a collimated HeNe laser.

3.1 Resolution in FT Spectroscopy

Assume an interferogram obtained by illuminating an LGI MEMS device moving d=500µm zero-to-peak at f=350Hz with a monochromatic source of 10µm wavelength. Below is the half of this interferogram illustrating the signal taken while the MEMS device deflects from peak-to-peak. Three subplots show the signal before resampling, after resampling, and the magnitude of the computed Fourier spectrum.

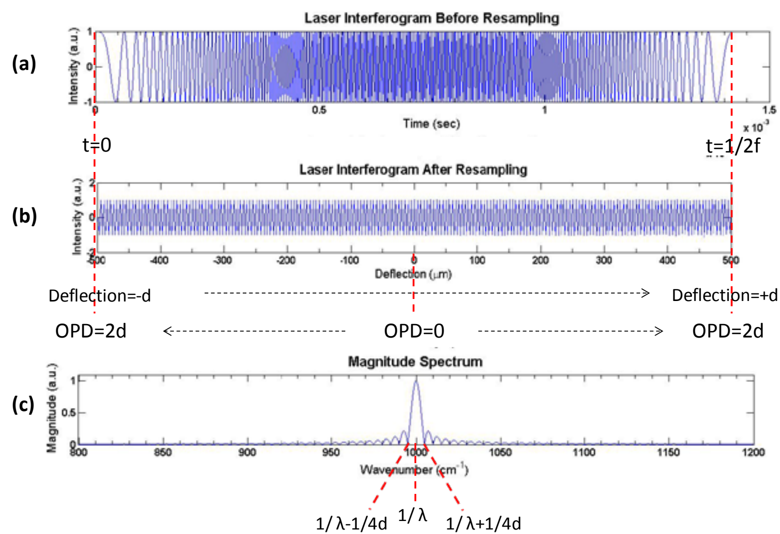

Figure 3.1 (a) Interferogram before resampling. (b) Interferogram after resampling. (c) Spectrum.

It was previously explained in Chapter 1 that 0th order was used in FTS systems since its location is independent of the light source's wavelength and it has the highest intensity. At the center of the diffraction plane (α=0° in Figure 1.6), where 0th order is observed, term A and term B in equation (1-11) becomes unity. The intensity at this point is described by term C as given below.

$$I(\rho) = \cos^2\left(\frac{\varphi}{2}\right) = \cos^2\left(\pi\frac{\rho}{\lambda}\right) = \frac{1}{2}\left[1 + \cos\left(2\pi\frac{\rho}{\lambda}\right)\right] \tag{3-1}$$

The spectral information regarding the source solely depends on the sinusoidal part of equation (3-1). However in practice, the intensity recorded at the detector is affected by wavelength dependant factors such as beam splitter efficiency, detector responsivity and amplifier characteristics. Therefore equation (3-1) can be simplified to the below equation where all wavelength dependant factors are combined.

$$I(\rho) = \mathrm{B}(\mathrm{k})\cos(2\pi\mathrm{k}\rho) \tag{3-2}$$

The spectrum is calculated from interferogram by computing the cosine Fourier transform of I(ρ), which is the reason that the technique is named Fourier transform spectroscopy [25].

Practically, complex Fourier transform is used instead of cosine Fourier transform due to asymmetry in the interferogram resulting from phase errors. The operation is performed on a double sided interferogram using fast Fourier transform (FFT) which reduces the computation time substantially. Zero padding is applied to increase the resolution and the size of data points to a power of two [26].

Fourier transform algorithm is based on transforming equally distanced time domain samples to the frequency domain, which can be correlated to transforming equally distanced optical path difference (or deflection) domain samples to wavenumber domain. However, due to sinusoidal speed variation of the LGI MEMS device, the interferogram of

a monochromatic source is a chirped sinusoid. This is fixed by interpolation and resampling to create a spatially equidistant interferogram with a period of λ in OPD domain.

Resampled interferogram and its Fourier transform can be defined as,

$$I(\rho) = \mathrm{rect}\left(\frac{\rho}{4\mathrm{d}}\right)\cos\left(2\pi\frac{\rho}{\lambda}\right)$$

$$\mathbf{I}(k) = FT\left\{\mathrm{rect}\left(\frac{\rho}{4\mathrm{d}}\right)\right\} * \mathrm{FT}\left\{\cos\left(2\pi\frac{\rho}{\lambda}\right)\right\} \quad (3\text{-}3)$$

$$= 4\mathrm{dsinc}(4\mathrm{d}k) * \frac{1}{2}\left[\delta\left(k+\frac{1}{\lambda}\right) + \delta\left(k-\frac{1}{\lambda}\right)\right]$$

Above convolution results in two sinc functions located on ±1/λ in the k-space, where k is called the wavenumber and defined as 1/λ (not as angular wavenumber 2π/λ) and expressed in cm^{-1}. Resolution is the distance between the first zero crossings of this sinc function which is called the main lobe width.

$$\mathrm{sinc}(4\mathrm{d}k) = \frac{\sin(\pi 4\mathrm{d}k)}{\pi 4\mathrm{d}k} \quad (3\text{-}4)$$

Equation (3-4) is equal to zero when $\pi 4\mathrm{d}k = n\pi$ for $n = \pm 1,2,3,\ldots$

Therefore, the first zero crossings are at $k_{\pm 1} = \frac{1}{\lambda} \pm \frac{1}{4\mathrm{d}}$

The resolution based on the main lobe width is given by:

$$\Delta k = k_1 - k_{-1} = \left(\frac{1}{\lambda}+\frac{1}{4\mathrm{d}}\right) - \left(\frac{1}{\lambda}-\frac{1}{4\mathrm{d}}\right) = \frac{1}{2\mathrm{d}} = \frac{1}{\mathrm{OPD}} \quad (3\text{-}5)$$

Another representation method for resolution is full-width-half-max (FWHM). Since the sinc function has a FWHM of 0.605, FWHM resolution of a monochromatic source can be described as:

$$\Delta k_{FWHM} = \frac{0.605}{\mathrm{OPD}} \quad (3\text{-}6)$$

However, resolution is a wavelength dependent value and this dependency could be introduced as $= \frac{1}{\lambda} \rightarrow \frac{dk}{d\lambda} = -\frac{1}{\lambda^2}$.

Ignoring the negative sign, $\Delta k = \frac{\Delta\lambda}{\lambda^2} = \frac{1}{\text{OPD}} \rightarrow \Delta\lambda = \frac{\lambda^2}{\text{OPD}}$.

Thus, FWHM representation is,

$$\Delta k_{FWHM} = 0.605 \frac{\lambda^2}{\text{OPD}} \tag{3-7}$$

Let's say single sided interferogram starting from resting point (zero deflection) to d=500μm is used. Then equation (3-3) and (3-4) become,

$$I(\rho) = \text{rect}\left(\frac{\rho}{2\text{d}}\right)\cos\left(2\pi\frac{\rho}{\lambda}\right)$$

$$\mathbf{I}(k) = FT\left\{\text{rect}\left(\frac{\rho}{2\text{d}}\right)\right\} * \text{FT}\left\{\cos\left(2\pi\frac{\rho}{\lambda}\right)\right\} \tag{3-8}$$

$$= 2\text{dsinc}(2\text{d}k) * \frac{1}{2}\left[\delta\left(k + \frac{1}{\lambda}\right) + \delta\left(k - \frac{1}{\lambda}\right)\right]$$

$$\text{sinc}(2\text{d}k) = \frac{\sin(\pi 2\text{d}k)}{\pi 2\text{d}k} \tag{3-9}$$

which results in a change in main lobe width. Similar to equation (3-3), $\pi 2\text{d}k = n\pi$ for $n = \pm 1,2,3, \ldots$ must hold for the zero crossings of the sinc function.

Therefore, the first zero crossings get shifted away such that $k_{\pm 1} = \frac{1}{\lambda} \pm \frac{1}{2\text{d}}$

The resolution gets twice worse than using double sided interferogram.

$$\Delta k = k_1 - k_{-1} = \left(\frac{1}{\lambda} + \frac{1}{2\text{d}}\right) - \left(\frac{1}{\lambda} - \frac{1}{2\text{d}}\right) = \frac{1}{\text{d}} = \frac{1}{\text{OPD}/2} \tag{3-10}$$

Above discussion about Fourier transform calculations is finalized with spectral results of an interferogram created in MATLAB for 1mm p-p deflection for a HeNe laser with 632.8nm wavelength. Figure 3.2 shows discrete cosine transform (DCT) of a single sided interferogram, fast Fourier transform (FFT) of a double and single sided interferograms

respectively. The results also suggest that the best resolution is achieved by applying FFT to a double sided interferogram.

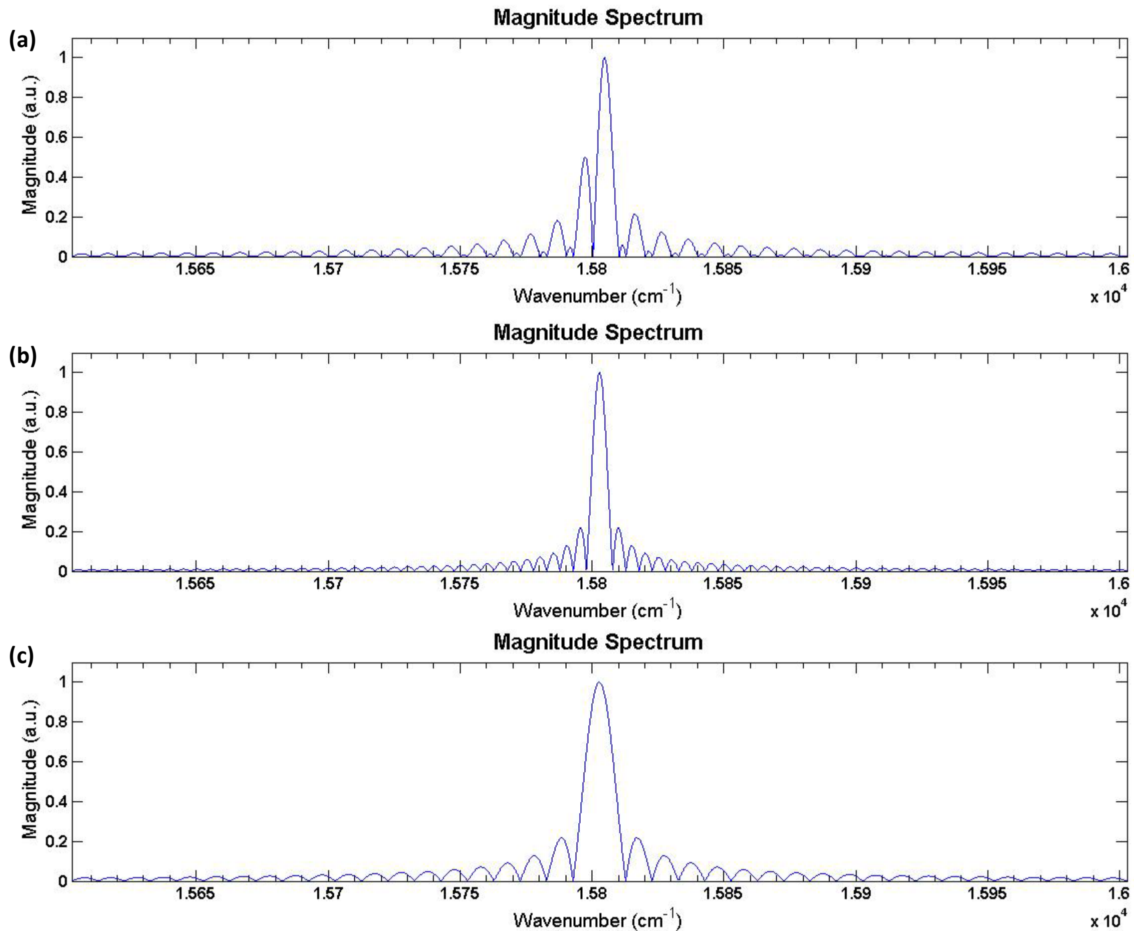

Figure 3.2 (a) Discrete Fourier transform of a single sided interferogram. (b) Fast Fourier transform of a double sided interferogram. (c) Fast Fourier transform of a single sided interferogram.

3.2 Effect of Incidence Angle on Resolution

One of the main advantages of LGI over Michelson configuration is that it requires less number of optical elements. Since no beam splitter is used in LGI, the incoming beam is

compelled to be sent with an incidence angle. A nonzero incidence angle changes the optical path difference, thus the resolution.

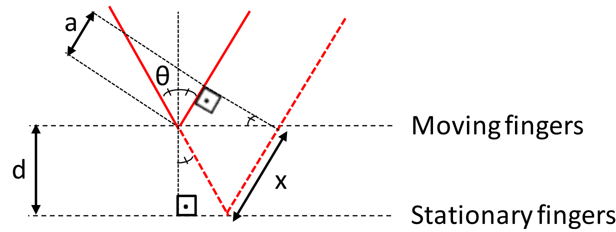

Figure 3.3 OPD calculation with nonzero incidence angle illumination.

$$\begin{aligned} \mathrm{OPD} &= 2\mathrm{x} - \mathrm{a} = 2\frac{\mathrm{d}}{\cos\theta} - 2\mathrm{d}\tan\theta\sin\theta \\ &= 2\frac{\mathrm{d}}{\cos\theta} - 2\mathrm{d}\frac{\sin\theta}{\cos\theta}\sin\theta = \frac{2\mathrm{d}}{\cos\theta}(1-\sin^2\theta) \\ &= \frac{2\mathrm{d}}{\cos\theta}\cos^2\theta = 2\mathrm{d}\cos\theta \end{aligned} \tag{3-11}$$

The effect of incidence angle can be observed experimentally in Figure 3.4. Note that the resolution (or main lobe width) deteriorates with increasing incidence angle. When the light impinges on the MEMS device perpendicularly ($\theta = 0$), the cosine term becomes unity and OPD will be calculated as double the deflection. As explained in the next section, optical characterization with monochromatic source is done with zero incidence angle using a beam splitter for the sake of simplicity. However, in the full system integration where no beam splitter is used, an incidence angle around 17º is introduced. Both theoretical and experimental resolution of the final system is discussed in Chapter 5 in detail.

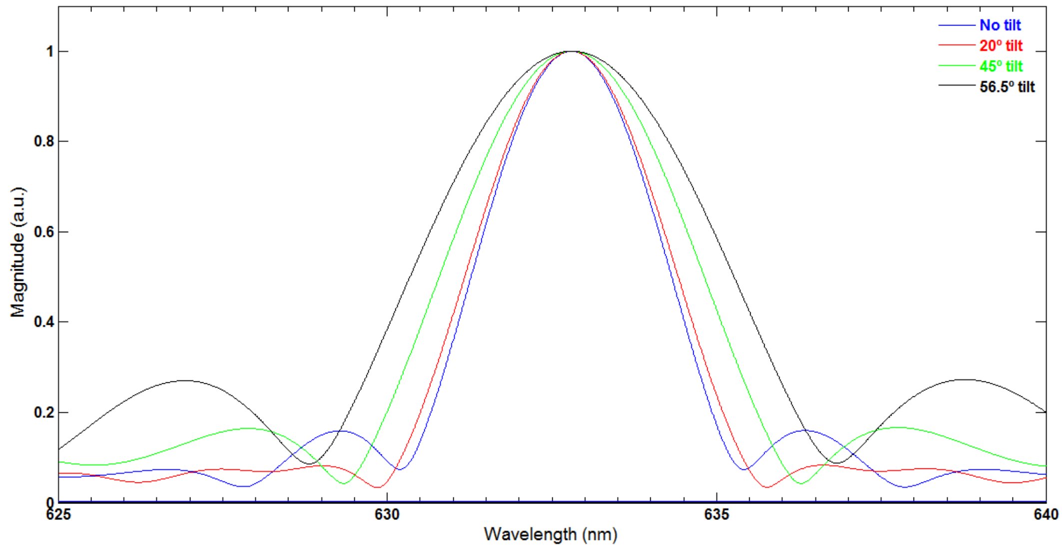

Figure 3.4 Device III-SM actuated with 30V at 667Hz at various incidence angles.

3.3 Optical Characterization Results

MEMS devices are optically characterized with a monochromatic source before integration with IR optics. Spatially equidistant sampling is assured by using a reference monochromatic light source with known wavelength. Since a constructive interference occurs when the optical path difference is equal to the wavelength of source, the distance between the peaks of sinusoids in the laser interferogram is equal to the wavelength of source. For optical characterization, a blue reference laser (λ=408nm) is used for sampling the interferogram of the unknown source which is a red HeNe laser (λ=632.8nm) in the experiment. The device is illuminated with HeNe laser on the front side while the blue laser is directed at the backside of the MEMS. 0th order interference patterns obtained from both lasers are recorded by separate photodetectors. Interferogram of the unknown source is sampled at the peaks and zero crossings of the reference source's interferogram. After interpolation, the Fourier transform is applied and the spectrum is acquired.

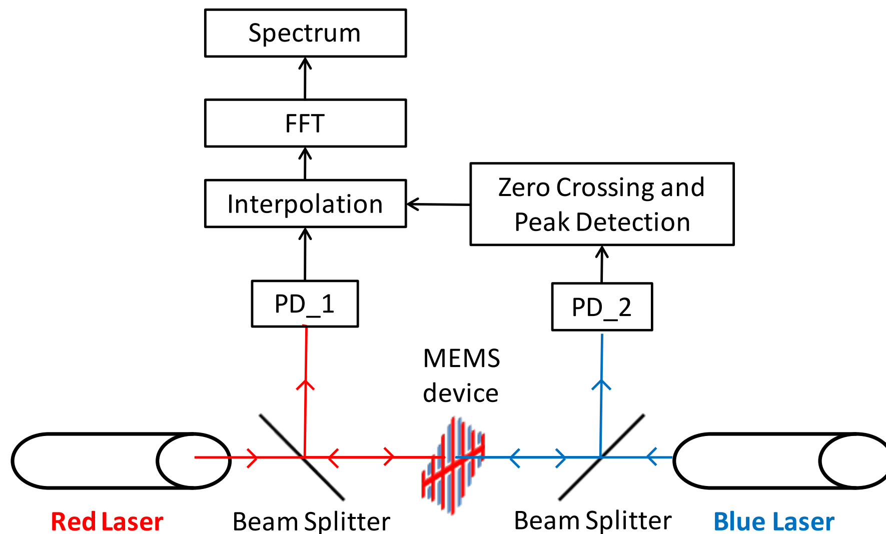

Figure 3.5 Optical characterization setup and data analysis algorithm.

Only a small part of the grating is illuminated since dynamic deformation is the key factor in the construction of the spectrum. As described in chapter 1, the targeted wavelength range gives an allowable dynamic deformation of 250nm, which is significantly over the limit for the visible range. Hence only a small part in the grating area of an LGI MEMS device is illuminated with aforementioned lasers.

In Figure 3.6 (a), interferograms measured with a red (λ=632.8nm) and reference blue (λ=408nm) lasers at small deflection are plotted to show the chirped nature of the signal before resampling. In subplots (b) and (c), interferogram before and after resampling for a 2nd prototype device that is deflecting 448µm p-p with 50V at 296Hz are given respectively. Note that the DC offset is subtracted from the interferogram before performing the Fourier transform.

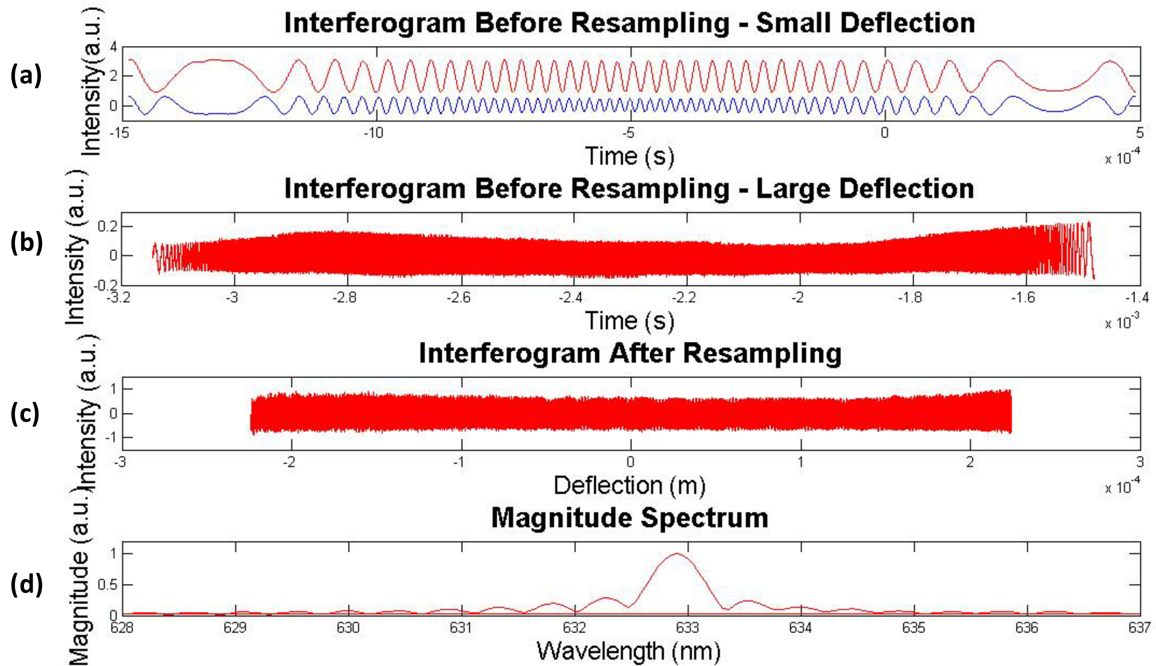

Figure 3.6 (a) Interferograms measured with a red (λ=632.8nm) and a reference blue (λ=408nm) laser at small deflection. (b) Interferogram before resampling at large deflection. (c) Interferogram after resampling. (d) Magnitude spectrum.

Theoretical FWHM resolution at this deflection is calculated as 0.54nm using equation (3-6). The experimental FWHM resolution of the spectrum shown in Figure 3.6 (d) is measured as 0.56nm which is consistent with the theoretical value.

Optical characterization with two lasers is performed at a relatively low deflection due to obligatory electrostatic actuation. The same test is done using only one laser source with speaker actuation, where a higher deflection could be achieved without pull-in risk but only one side of the device is suitable for illumination.

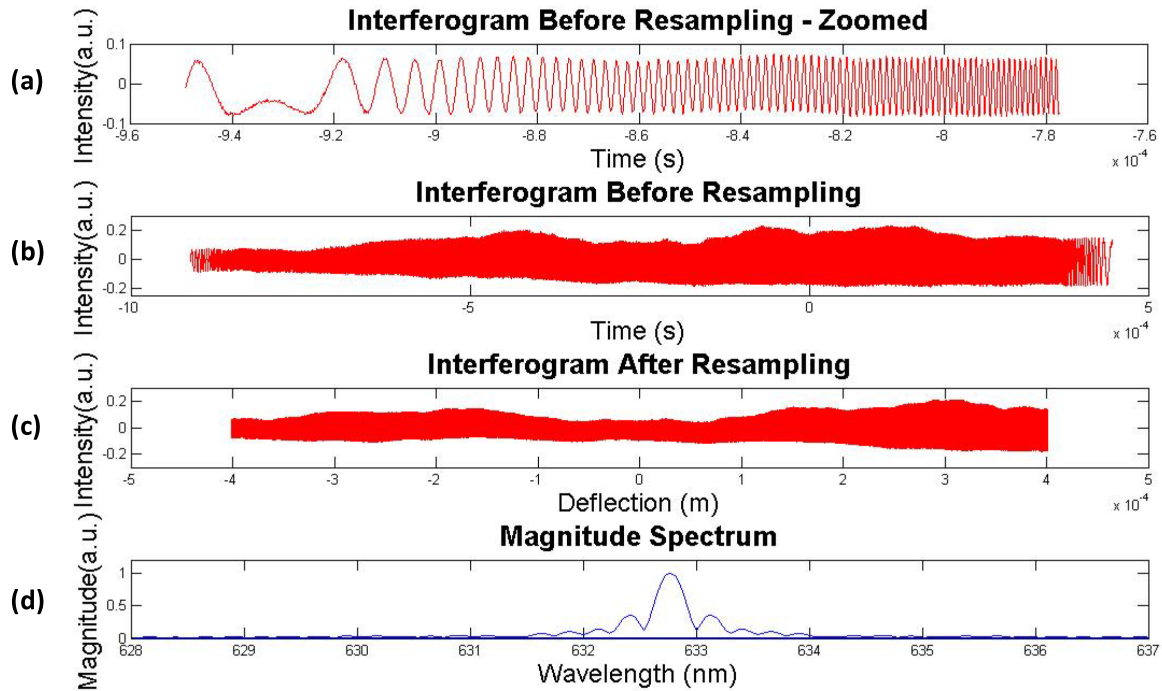

Figure 3.7 (a) Zoomed view of the laser interferogram. (b) Interferogram before resampling with its DC offset removed. (c) Interferogram after resampling. (d) Magnitude spectrum.

A prototype 1 device from the last fabrication run that deflects 803µm p-p at 361.7Hz with speaker actuation is used. In Figure 3.7 (a), zoomed view of the laser interferogram before resampling is shown. The signal in (b) is resampled at its own zero crossings and peaks to get equidistant sampling. Later, this resampled signal shown in (c) is transformed to Fourier domain and spectrum is obtained as shown in (d). Both experimental and theoretical FWHM resolutions are calculated as 0.3nm.

4 OPTICAL SIMULATIONS

LGI based spectrometer design is optically optimized as described in [27] by our group previously. Four main constraints discussed can be summarized as follows:

- Deflection (d): Since the resolution of a Fourier transform spectrometer is dependent on the optical path difference between two mirrors, which is double the deflection, a resolution limit of 10cm^{-1} set by MEMFIS project brings a minimum deflection requirement of 500µm as calculated by equation (3-3).
- Half divergence angle (θ_d): Divergence is a term used for quantifying the degree of collimation of a source. To obtain the desired resolution optical elements must be chosen such that the below criteria is satisfied. (Note that MEMFIS detector is designed to work in 2.5-16µm wavelength range which corresponds to 625-4000cm^{-1} in wavenumbers)

$$\theta_d \leq \sqrt{\frac{\Delta k}{k_{max}}} = \sqrt{\frac{10cm^{-1}}{4000cm^{-1}}} = 2.86° \quad (4\text{-}1)$$

  The half divergence angle is chosen as 2.5°.
- Order separation: 0th and 1st order separation is assured under the condition given below.

$$\sin(2\theta_d) \leq \frac{\lambda_{min}}{\Lambda} \quad (4\text{-}2)$$

  which requires that the grating period should be less than or equal to 28.6µm ($\Lambda \leq 28.6$µm).

- Talbot phase reversal: Phase reversed Talbot images appear at integer multiples of Λ^2/λ which deteriorates the interferogram if the deflection is smaller than this value. Therefore, the below equation must hold bringing the second condition for the grating period, $\Lambda > 89.4\mu m$.

$$\Lambda > \sqrt{\lambda_{max} d} \tag{4-3}$$

The optimization result showed that the Talbot phase reversal was the critical factor determining the resolution. Hence devices with Λ=100µm and Λ=130µm are fabricated.

In this chapter, optical simulations are ran to find out the best lens configuration taking into account the available optical elements, detector window size and properties of working MEMS devices.

4.1 Optical Setup Optimization

The current optical setup is simulated in MATLAB to find the optimum configuration using a Fresnel beam propagation code based on scalar diffraction theory. Firstly, a plane wave is created taking the divergence introduced by the collimating lens into account. The half divergence is defined as,

$$\theta_d = \tan^{-1}\left(\frac{D}{2f}\right) \tag{4-4}$$

where D is the diameter of the IR source and f is the focal length of the collimating lens.

Then, the beam is propagated through LGI which is done in a loop that describes the movement of the MEMS device. In LGI, the incoming beam is multiplied with the amplitude transmittance function of the moving grating, propagated for a distance x, multiplied with the amplitude reflection function of the fixed grating, propagated for a distance x again and then multiplied with the amplitude transmittance function of the moving grating for the last time. Afterwards, the reflected wave pattern from the moving

grating is added to the calculated diffracted pattern. There is some propagation distance to the focusing lens but the lens is assumed adjacent to the LGI since it has little effect on the result. Then, the resulting beam is passed through the focusing lens, where a phase factor is introduced. Later the beam is propagated from the focusing lens to the detector which is located at the focal point of the lens. Intensity at the detector is calculated by adding the amplitude squared beam pattern that fits in the detector window ($D_{detector}$=1.4mm, extracted from ZEMAX simulations) which is acquired in the steps repeated for a deflection of x=[-468µm – 468µm] with divergence angle ranging between $-\theta_d$ to θ_d . The propagation from both collimating lens to LGI and from LGI to focusing lens are skipped due to their negligible effects on resolution.

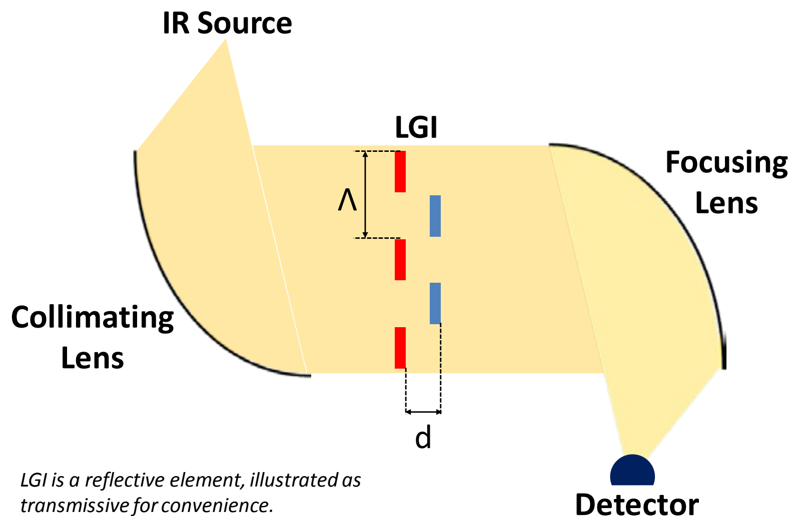

Figure 4.1 Schematics of simulated setup.

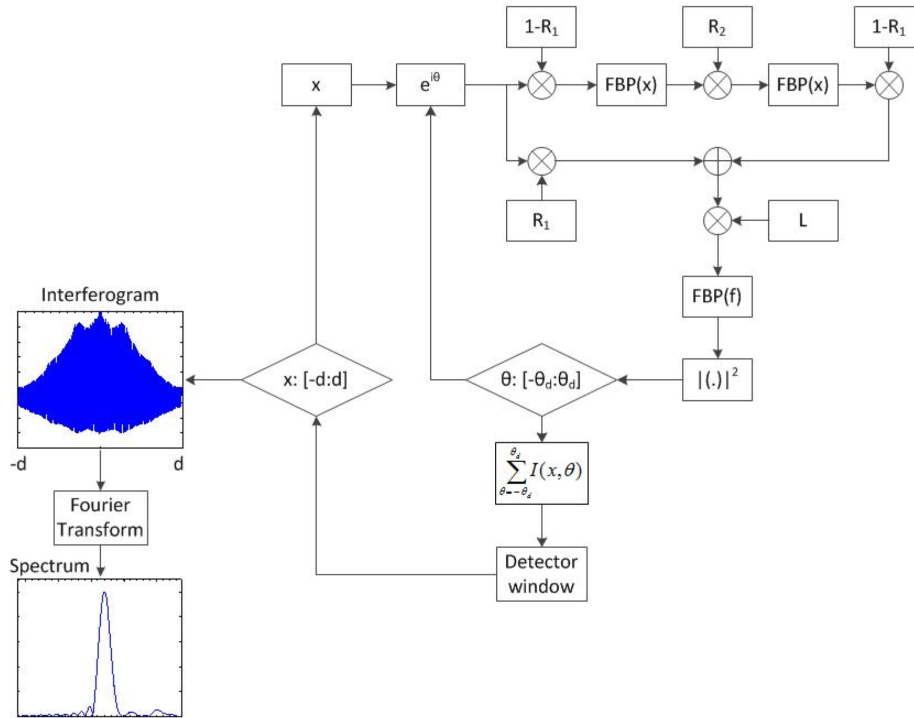

Figure 4.2 Flowchart of the algorithm. FBP(x): Fresnel beam propagation for distance x. R_1, R_2: Amplitude reflectance function of moving, stationary grating fingers. L: Amplitude transmittance function of lens.

The available lenses are summarized in the table below.

Lens Type	Focal Length (mm)	Available Quantity
Off-axis parabolic (90º)	5.8	1
Off-axis parabolic (90º)	10	1
Off-axis parabolic (90º)	20	3
Positive Meniscus	12.85	1

Table 4.1 Available optical components.

All the cases with available optical elements are investigated and summarized in the table below.

Case #	$f_{collimating}$ (mm)	$f_{focusing}$ (mm)	Half Divergence, θ_d (°)	Order Separation (µm)			Max. 0th order shift (µm)	Δk_{FWHM} (cm^{-1})			SBR		
				λ=3.3µm	λ=6.45µm	λ=16µm		λ=3.3µm	λ=6.45µm	λ=16µm	λ=3.3µm	λ=6.45µm	λ=16µm
1	20	5.8	0.71	191.43	374.36	932	72.5	23.22	17.74	8.52	0.01	0.05	0.79
2	12.85	5.8	1.11	191.43	374.36	932	112.84	22.82	12.66	8.53	0.01	0.05	0.78
3	20	12.85	0.71	424.12	829.4	2064.87	160.63	18.19	6.58	8.52	0.03	0.71	0.8
4	20	10	0.71	330.06	645.44	1606.91	125	17.54	10.6	8.52	0.03	0.17	0.73
5	12.85	10	1.11	330.06	645.44	1606.91	194.55	17.2	6.53	8.52	0.03	0.21	0.72
6	10	5.8	1.43	191.43	374.36	932	145	14.5	12.92	8.53	0.01	0.04	0.78
7	5.8	10	2.46	330.06	645.44	1606.91	431.03	8.07	7.63	8.49	0.03	0.22	0.71
8	5.8	12.85	2.46	424.12	829.4	2064.87	553.8	7.63	7.28	8.57	0.12	0.36	0.76
9	5.8	20	2.46	660.12	1290.89	3213.81	862.07	7.38	6.88	8.48	0.16	0.52	0.72
10	10	12.85	1.43	424.12	829.4	2064.87	321.25	7.3	6.75	8.57	0.04	0.46	0.79
11	10	20	1.43	660.12	1290.89	3213.81	500	7.12	6.7	8.54	0.25	0.91	0.74
12	12.85	20	1.11	660.12	1290.89	3213.81	389.11	7.03	6.64	8.54	0.25	0.92	0.74
13	20	20	0.71	660.12	1290.89	3213.81	250	6.86	6.59	8.52	0.26	0.93	0.73

Table 4.2 Physical optics simulation results.

Simulation is ran for both short (λ=3.3µm, corresponds to k=3030cm^{-1}) and moderate (λ=6.45µm, corresponds to k=1550cm^{-1}) and long (λ=16µm, corresponds to k=625cm^{-1}) wavelengths. 1st and 0th order separation and maximum 0th order shift due to divergence are calculated as well as FWHM resolution and signal-to-bias ratio. Order separation is reported as the distance between the 0th and the 1st orders at the detector plane. It is calculated by multiplying angular order separation with the focal length of the collimating mirror as given in equation (4-5).

$$Order\ separation = \sin^{-1}\left(\frac{\lambda}{\Lambda}\right) * f_{focusing} \tag{4-5}$$

Maximum 0th order shift stems from the divergence introduced by the collimating mirror. It is calculated by the formula given below.

$$\begin{aligned} Max.\,0^{th}\ order\ shift &= \tan(\theta_d) * f_{focusing} \\ &= \tan\left(\tan^{-1}\left(\frac{D}{2f_{collimating}}\right)\right) * f_{focusing} \\ &= \frac{D}{2f_{collimating}} * f_{focusing} \end{aligned} \qquad (4\text{-}6)$$

The latter two parameters are important factors for determining SBR. For a high SBR, order separation should be large enough to avoid order mixing when divergence is introduced. At the same time, the maximum 0th order shift should be smaller than half the detector window size so that none of the 0th orders leak.

In SBR calculation, signal (S) is defined as the amplitude of the resulting spectral component at the source wavelength while bias (B) is the amplitude of interferogram's DC offset at the frequency domain as shown in Figure 4.3. Due to sinusoidal nature of the interferogram, two symmetric peaks, previously defined as signal, are observed at $\pm\lambda_0$. Thus, for SBR calculation these signals are added together or equivalently one of them is doubled since they are identical.

$$SBR = \frac{2S}{B} \qquad (4\text{-}7)$$

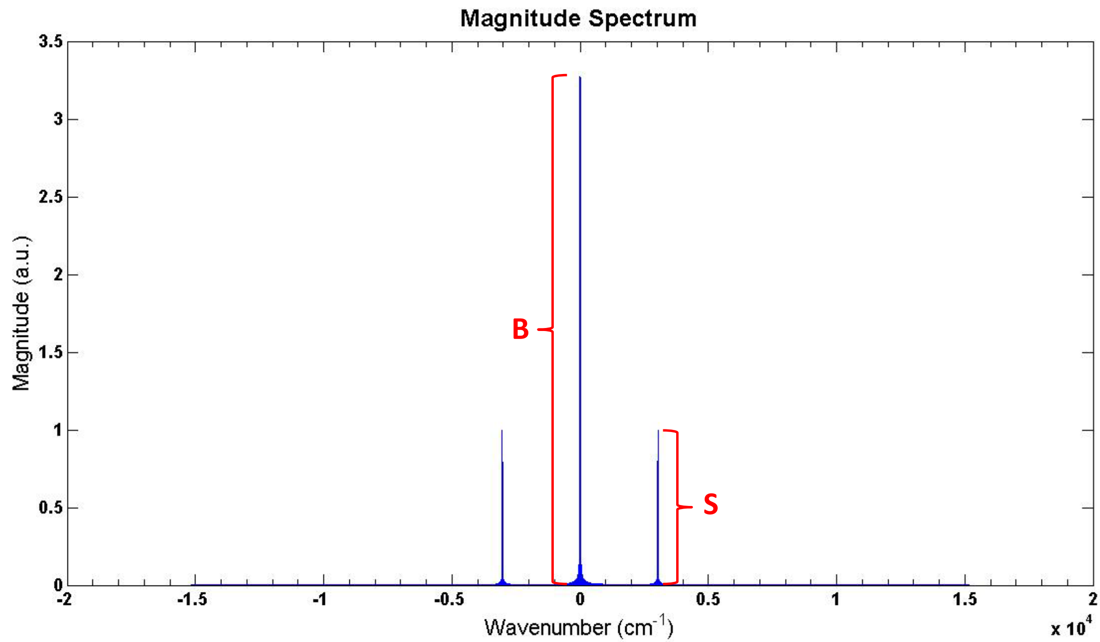

Figure 4.3 Exemplary spectrum for SBR definition.

IR experiments are conducted for case#3, case#8 and case#13 to compare the optical simulations with actual measurements. The simulation results are shown for these cases in Figure 4.4 to Figure 4.12 while the experimental results are explained in the next chapter in detail.

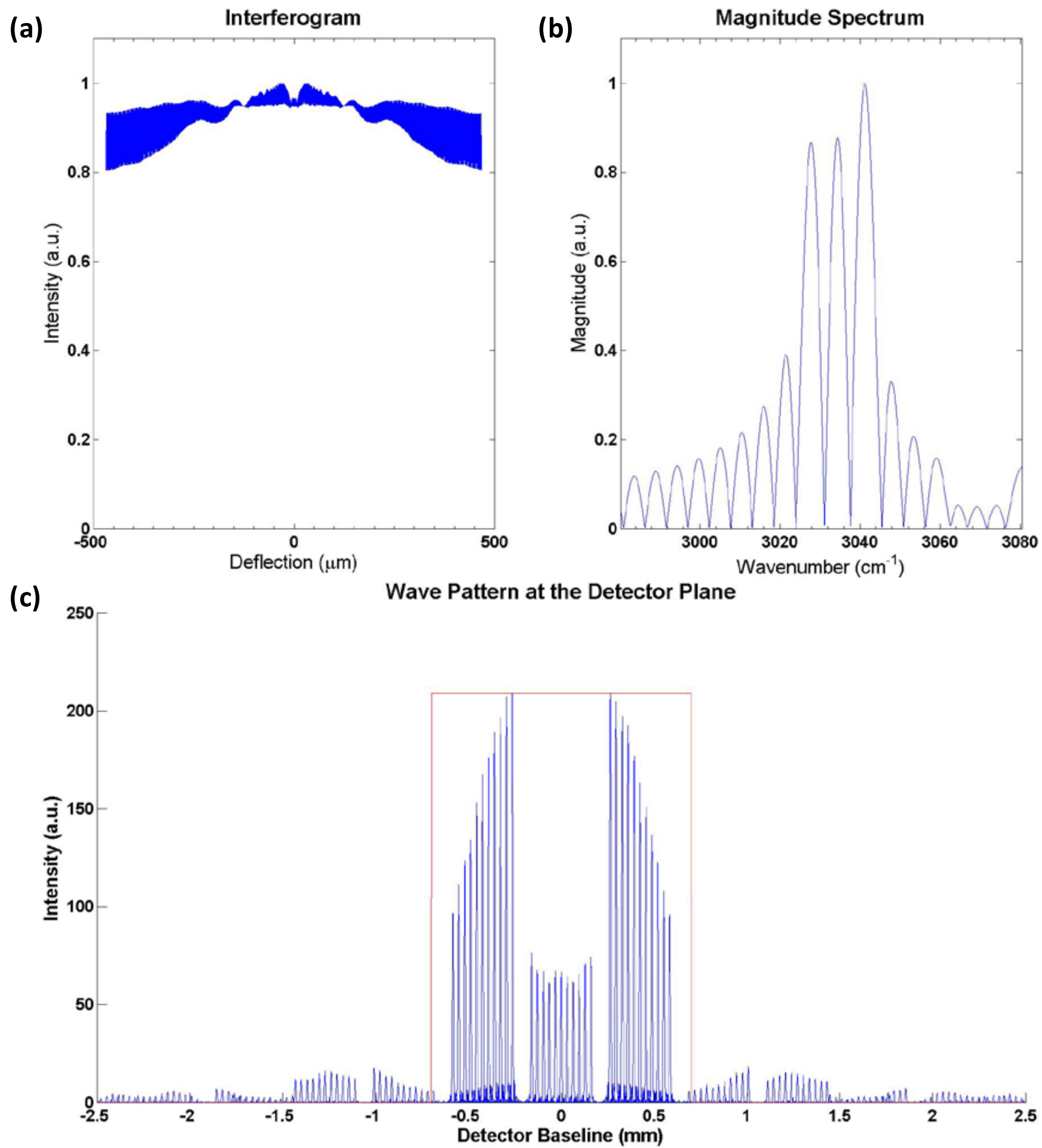

Figure 4.4 Physical optics simulation results of case#3 for λ=3.3µm. (a) Interferogram. (b) Magnitude spectrum. (c) Wave pattern at the detector plane at the highest deflection. The red box represents detector window.

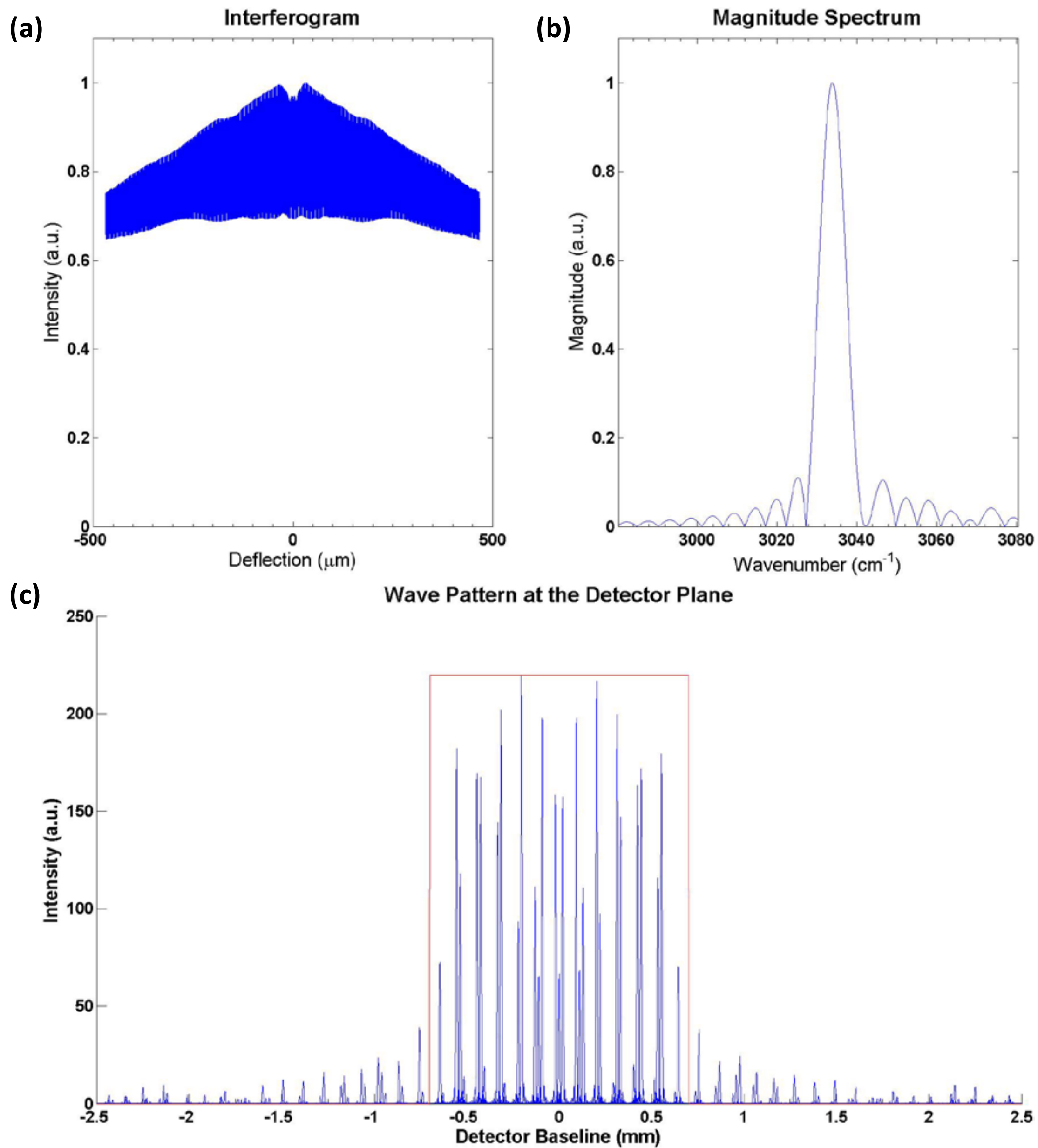

Figure 4.5 Physical optics simulation results of case#8 for λ=3.3µm. (a) Interferogram. (b) Magnitude spectrum. (c) Wave pattern at the detector plane at the highest deflection. The red box represents detector window.

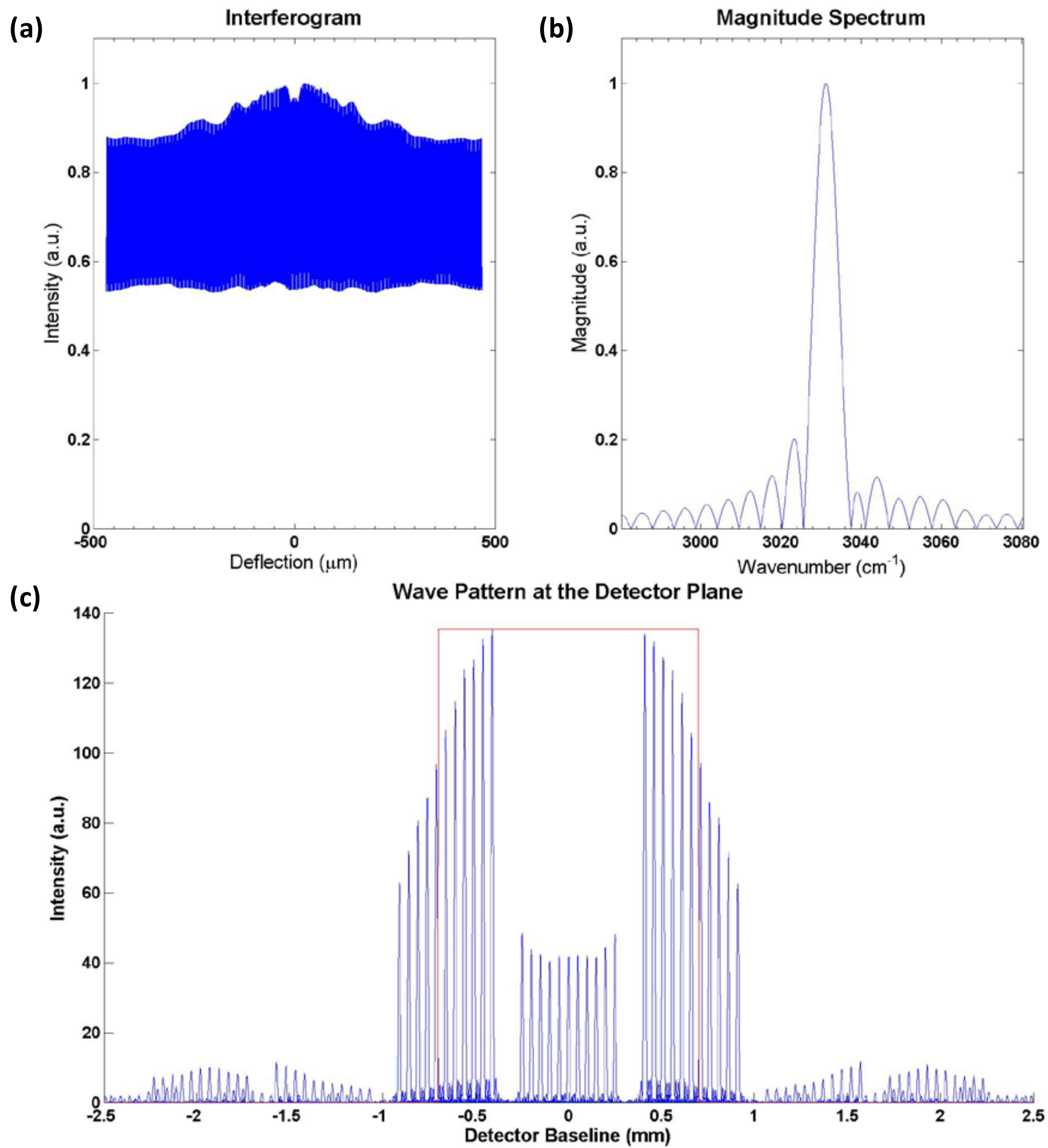

Figure 4.6 Physical optics simulation results of case#13 for λ=3.3μm. (a) Interferogram. (b) Magnitude spectrum. (c) Wave pattern at the detector plane at the highest deflection. The red box represents detector window.

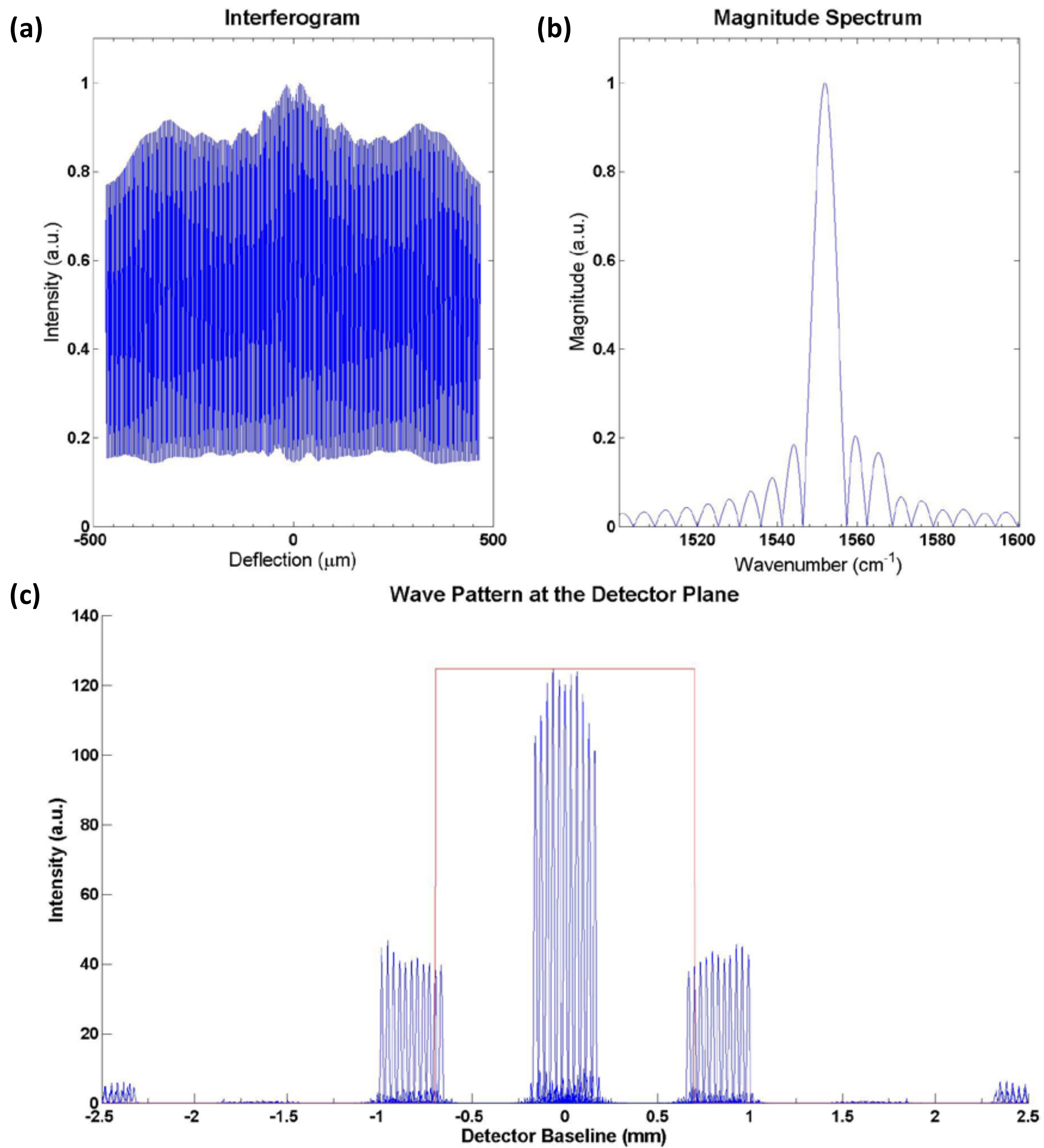

Figure 4.7 Physical optics simulation results of case#3 for λ=6.45μm. (a) Interferogram. (b) Magnitude spectrum. (c) Wave pattern at the detector plane at the highest deflection. The red box represents detector window.

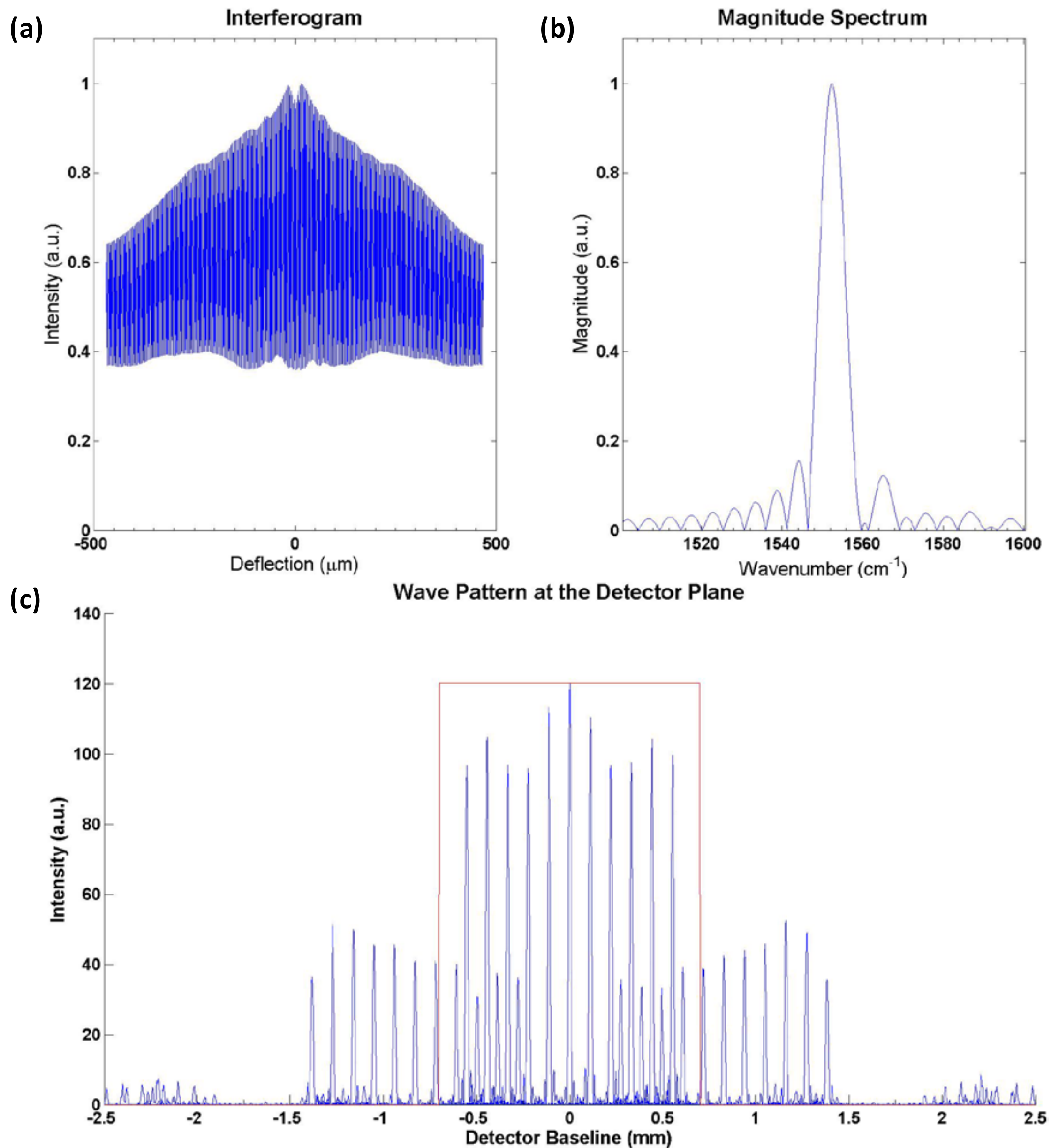

Figure 4.8 Physical optics simulation results of case#8 for λ=6.45μm. (a) Interferogram. (b) Magnitude spectrum. (c) Wave pattern at the detector plane at the highest deflection. The red box represents detector window.

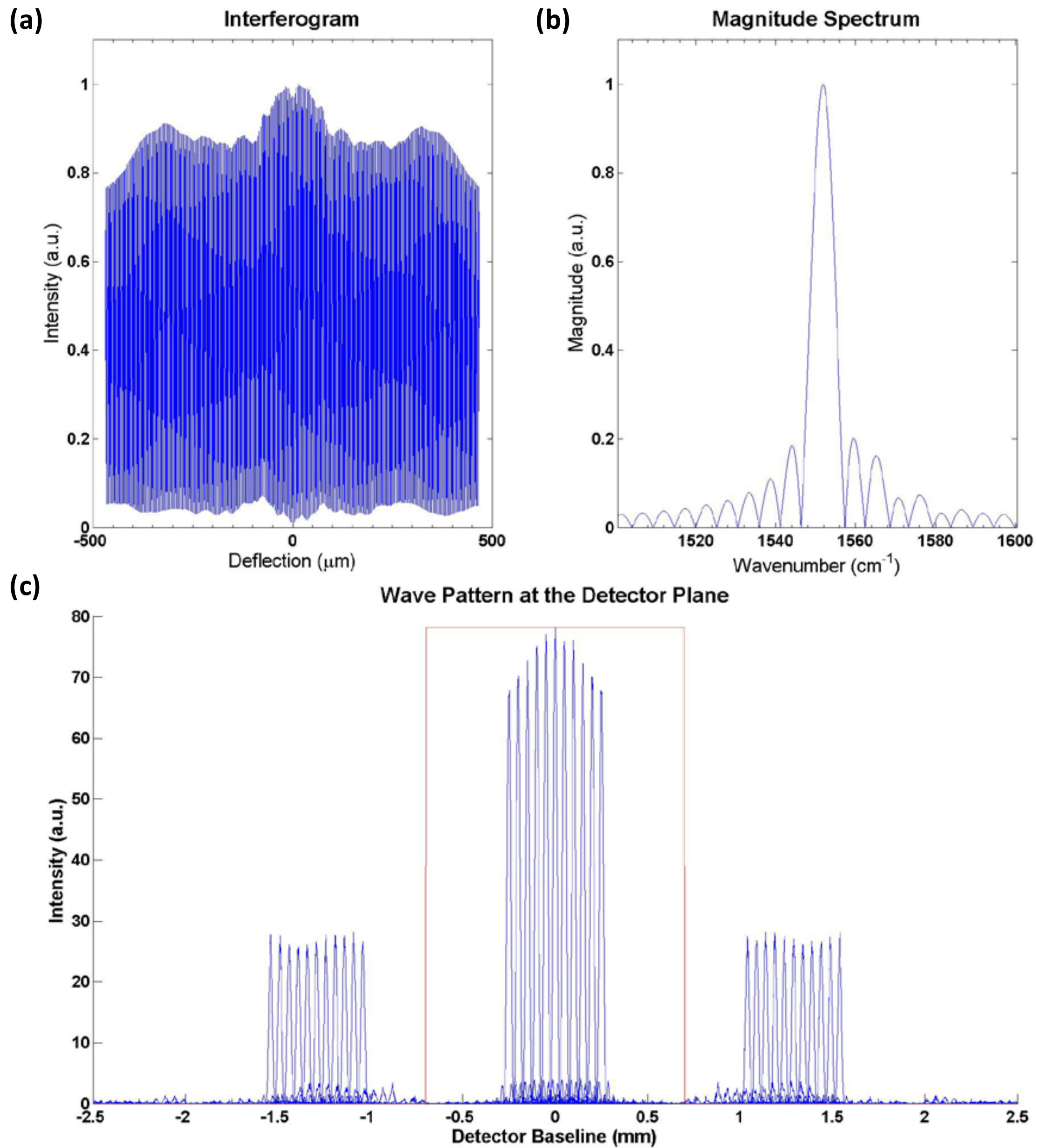

Figure 4.9 Physical optics simulation results of case#13 for λ=6.45μm. (a) Interferogram. (b) Magnitude spectrum. (c) Wave pattern at the detector plane at the highest deflection. The red box represents detector window.

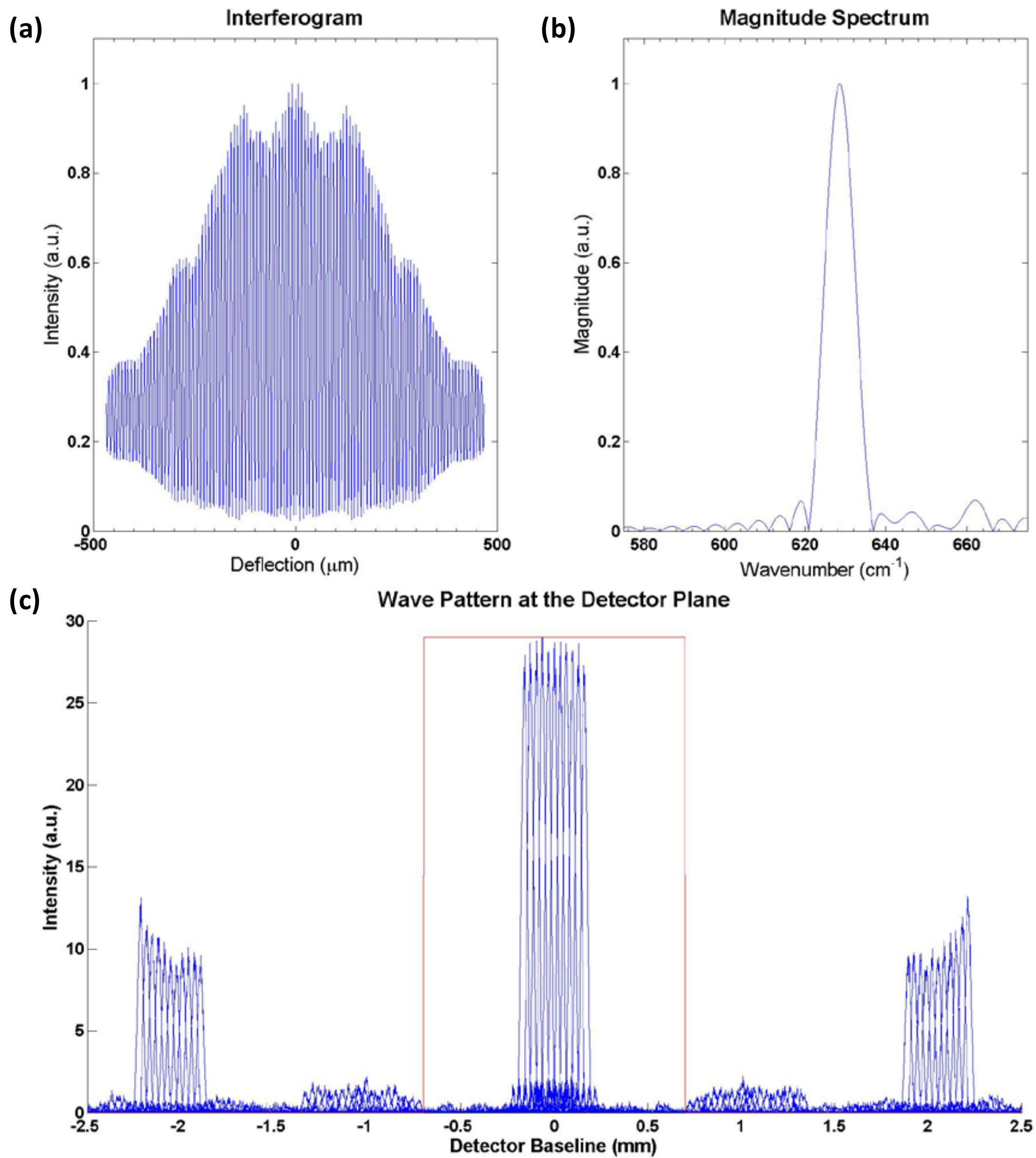

Figure 4.10 Physical optics simulation results of case#3 for λ=16μm. (a) Interferogram. (b) Magnitude spectrum. (c) Wave pattern at the detector plane at the highest deflection. The red box represents detector window.

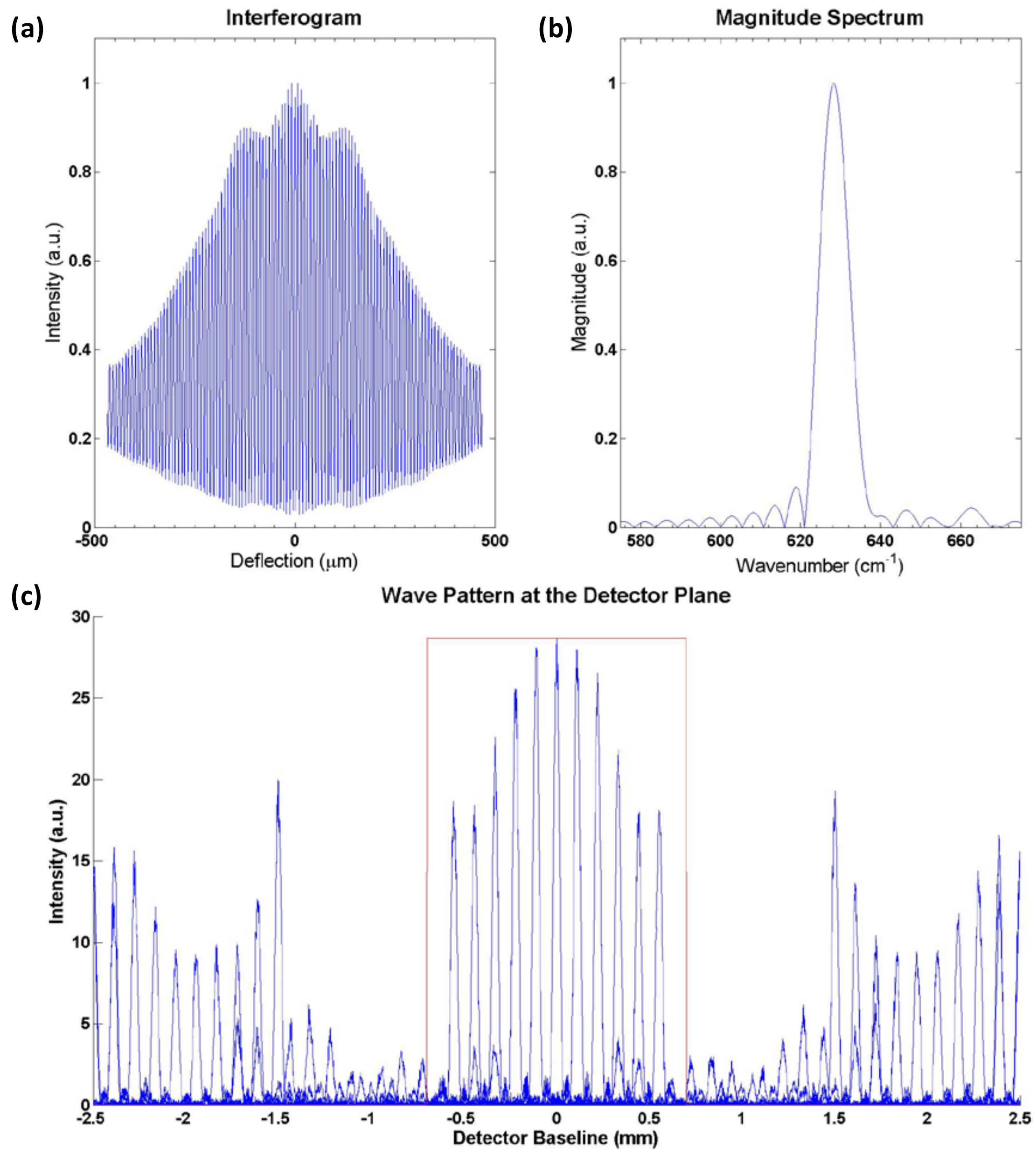

Figure 4.11 Physical optics simulation results of case#8 for λ=16μm. (a) Interferogram. (b) Magnitude spectrum. (c) Wave pattern at the detector plane at the highest deflection. The red box represents detector window.

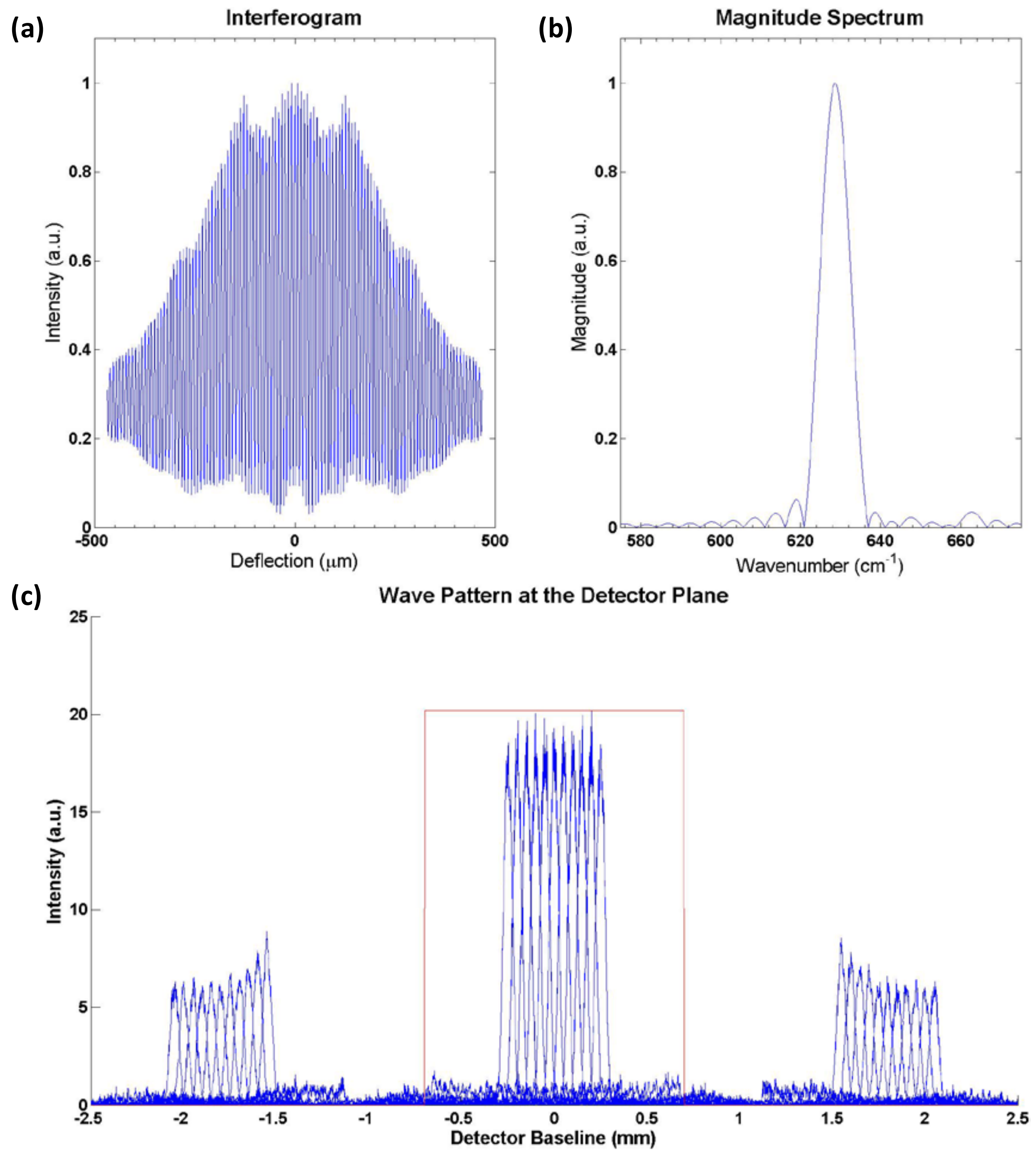

Figure 4.12 Physical optics simulation results of case#13 for λ=16μm. (a) Interferogram. (b) Magnitude spectrum. (c) Wave pattern at the detector plane at the highest deflection. The red box represents detector window.

FWHM resolution and SBR values calculated for all lens combinations are summarized in Figure 4.13. It is clearly seen that the order separation is very large for longer wavelengths and the mixing of the 0th and 1st orders is not a problem. For shorter wavelengths on the other hand, the order mixing partly cancels the interference and reduces the signal-to-bias ratio. From case#1 to case#13, SBR of shorter wavelengths exhibits an improving trend however remains worse than that of longer wavelengths. For λ=3.3µm, case#13 gives the best results in terms of both resolution and SBR. These results are experimentally verified as explained in the next chapter.

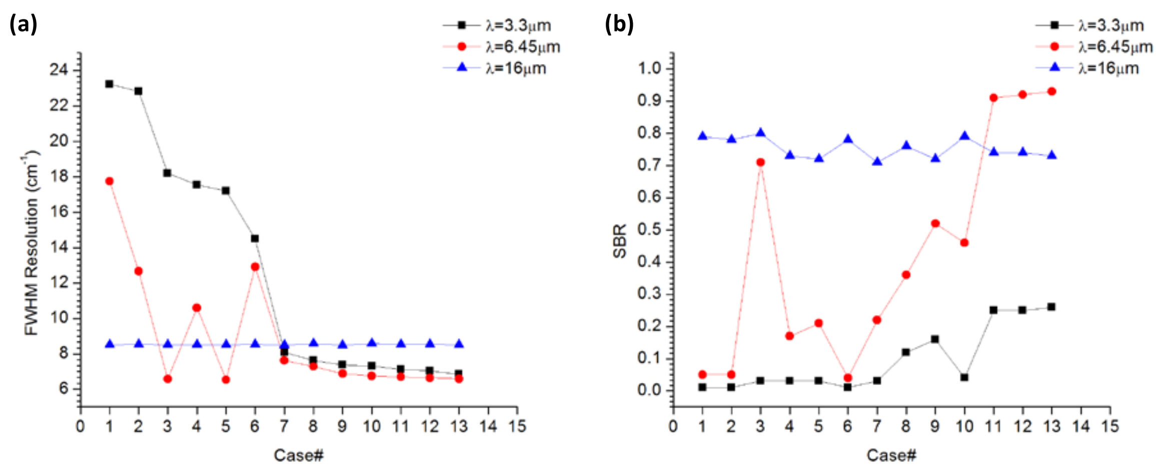

Figure 4.13 Physical optics simulation results for all lens combinations.

4.2 Optical Setup Power Calculations

Non-sequential ray tracing is performed in ZEMAX for case#3, case#8 and case#13 to compare the power acquired at the detector. An MIR source with 0.5mmx0.5mm size is created at 5µm wavelength. The half angle of cone of rays is assumed to be 25°. The off-axis parabolic mirror is placed 20mm away from the source where the beam gets partially collimated. Then the beam impinges on the MEMS device which is defined as a rectangular reflective surface of 2.5mmx5mm. The distance between the mirror and LGI is

approximately 2cm as measured in the experimental setup. Later, the reflected beam propagates for 6cm as in the actual setup and gets focused on the detector by a positive meniscus lens which is followed by a hyperhemispherical GaAs immersion lens. Note that the LGI device is tilted 17°. The power of the source is assumed to be 175mW.

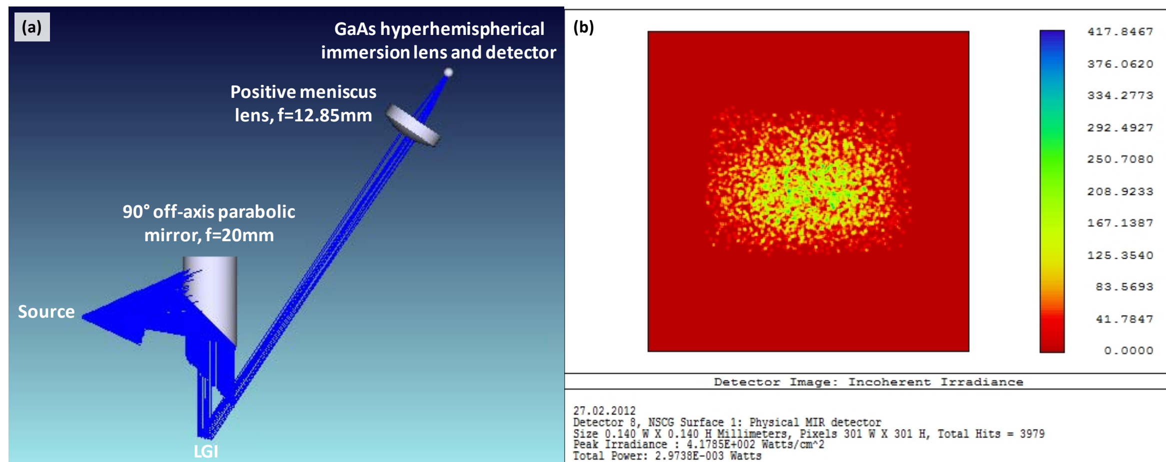

Figure 4.14 (a) ZEMAX design and (b) Detector view of case#3.

In case#8, the collimating mirror is replaced by an off-axis parabolic mirror with 5.8mm focal length. The distance between the source and the collimating mirror is decreased to 5.8mm and the rest of the layout remains the same as in the previous case.

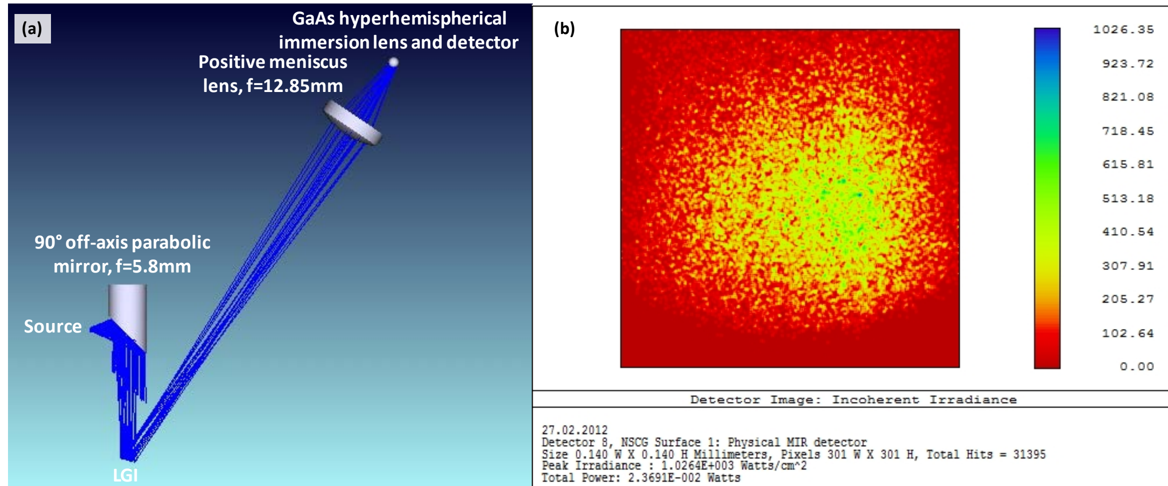

Figure 4.15 (a) ZEMAX design and (b) Detector view of case#8.

In case#13, the first off-axis parabolic mirror is placed 20mm away from the source. The propagation until the second and last off-axis parabolic mirror is the same as the previous cases. Focusing is done by an off-axis parabolic mirror followed by a GaAs hyperhemispherical lens. The ZEMAX design and the detector view are given in the following figures.

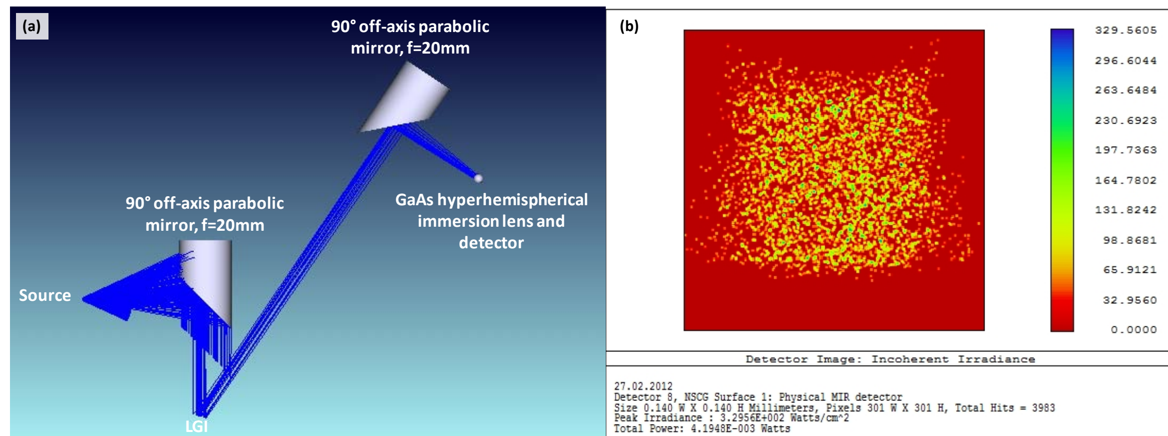

Figure 4.16 (a) ZEMAX design and (b) Detector view of case#13.

The power calculated by ZEMAX simulations and the voltage measured in the actual setup without sample is summarized below. Although the low detector signal level might be misleading, the total power calculated in ZEMAX is in accordance with the experimentally measured IR signal level at the detector.

Case #	**Total power at the detector, ZEMAX (mW)**	**p-p IR signal at the detector (mV)**
3	2.9	22
8	23.7	141
13	4.2	24

Table 4.3 Simulated detector power and experimentally detected signal amplitude for case#3, case#8 and case#13.

The ray tracing simulations suggest that case#8 is the best case due to high power obtained at the detector. However, physical optics simulations show that source wavelength and the grating period of the LGI MEMS device have dominating effects in terms of resolution and SBR. Despite the low power acquired at the detector, case#13 provides the best resolution and SBR for all wavelengths.

5 SPECTROMETER SYSTEM INTEGRATION

A bench top LGI based FTIR spectrometer is built using a MEMS device with good mechanical and optical performance. A broadband source and a mid-IR detector developed by Bruker Optics and Vigo Systems, respectively, are employed in the system. The rest of the optical components are provided by another MEMFIS project partner, CTR. In this chapter, details of the system will be explained as well as the spectral performance.

5.1 Infrared Source and Detector

In infrared spectroscopy, thermal emitters are commonly used broadband sources. The spectrum of the source is defined by Planck's Law which describes the electromagnetic energy emitted in terms of temperature and wavelength. Conventionally, resistively heated emitters are used. However, these emitters suffer from heat leakage through electrical connections. In the MEMFIS source developed specifically for the project, an infrared laser diode at 808nm with 2W optical power is used to heat the emitter. The laser is focused on the emitter by two aspheric lenses. The emitter made of silicon carbide (SiC) which has a high thermal conductivity and good spectral emissivity is held by a zirconium oxide (ZrO_2) holder that has a very low thermal conductivity. Hence, heat leakage is reduced substantially. To further improve the emissivity, 40µm sized cavities are drilled and C ions are implanted for creating an anti-reflective layer. The 25mm long source has a diameter of 12.5mm with a circular emission surface of 0.5mm. The source connected to a heatsink and its spectrum are shown in Figure 5.1.

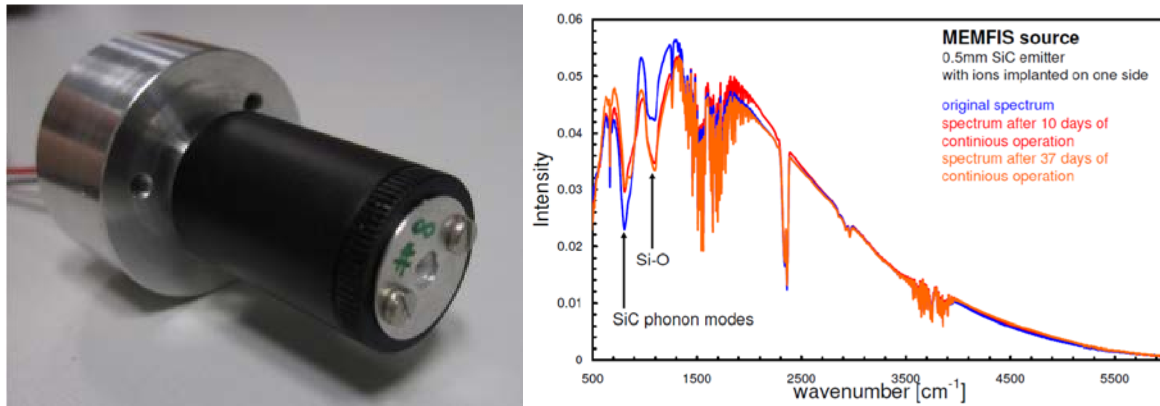

Figure 5.1 MEMFIS source and its spectrum.

The thermoelectrically cooled detector developed for MEMFIS project responds to wavelengths in the 2-16µm wavelength range. Incoming light is focused on the detector element by a ZnSe positive meniscus lens with 12.85mm focal length followed by a GaAs hyperhemispherical immersion lens with a radius of R=0.8mm. The size of the detector element is 140µmx140µm. The detector module provided to KOC by Vigo Systems does not include the positive meniscus focusing lens. Instead, it is separately employed in the optical system.

Figure 5.2 MEMFIS Detector.

5.2 LGI based FTS System Operation

LGI based FTS system operation is summarized in Figure 5.3. The MEMS device works in the out-of-plane mode with electrostatic actuation. The front side of the device is illuminated with an infrared source after collimation. The reflected light is then focused on the sample plane by an elliptic mirror, from which it is collected by another elliptic mirror which sends the light to the infrared detector. Thus, the IR interferogram is obtained. At the same time, the backside of the device is illuminated with a reference laser to create a nonuniform sampling clock. The 0th order is collected by the photodetector, which gives the reference laser interferogram, and a sampling clock is created by taking the zero crossings of this interferogram. After digitizing the IR interferogram with the nonuniform sampling clock, Fourier transform is applied and spectrum is acquired.

The spectrum is reported as percent transmittance and absorbance which are based on Beer-Lambert's Law. This law relates the absorption of the light to the properties of the material it is passing through. Its derivation as explained in detail in [28] is summarized as follows.

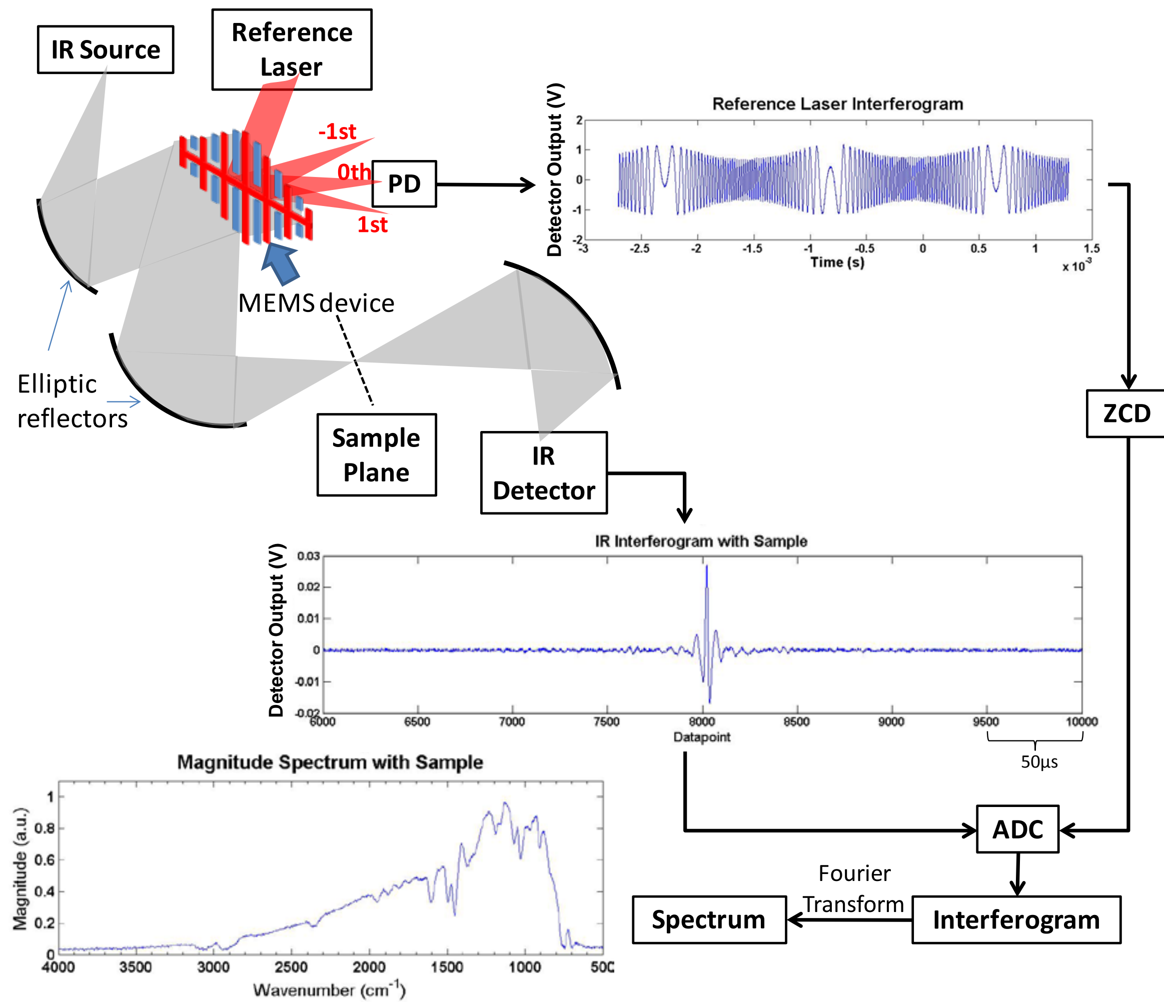

Figure 5.3 LGI based FTS operation. PD: Photodetector. ZCD: Zero-crossing detector, ADC: Analog-to-digital converter.

Assume that the light is propagating through a sample in x-direction (Figure 5.4). The change in intensity is proportional to the intensity by absorption coefficient, α, which has a measure of inverse length as given in equation (5-1).

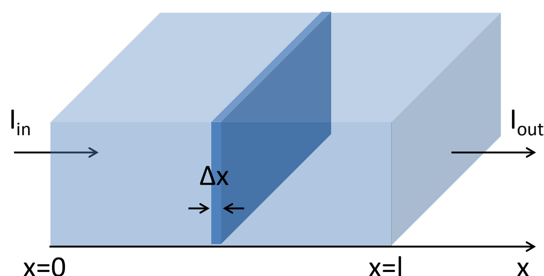

Figure 5.4 Light absorption in sample.

$$\frac{dI(x)}{dx} = -\alpha I(x) \tag{5-1}$$

After rearranging, this differential equation can be solved as shown below.

$$\frac{dI(x)}{I(x)} = -\alpha dx \tag{5-2}$$

$$\ln[I(x)] = -\alpha x + C \tag{5-3}$$

The constant C is determined by the initial condition which is $I_{in} = I(x = 0) = I_0$ in this case. Equation above can be written as the following instead. Note that $I_0 = e^C$.

$$I(x) = I_0 e^{-\alpha x} \tag{5-4}$$

If the light passes through a sample with thickness l, the intensity after the sample is,

$$I_{out} = I(l) = I_0 e^{-\alpha l} \tag{5-5}$$

Transmittance (T) is defined as the fraction of the light that passes through the sample such that,

$$T = \frac{I_{out}}{I_{in}} = \frac{I_0 e^{-\alpha l}}{I_0} = e^{-\alpha l} \tag{5-6}$$

Equation (5-5) can be written as below by introducing the complementary of transmittance, absorbance (A):

$$I_{out} = I(l) = I_0 e^{-A} \tag{5-7}$$

Practically, base 10 is used instead of e in most cases. Hence equation (5-7) becomes,

$$I_{out} = I(l) = I_0 10^{-A} \tag{5-8}$$

Then absorbance is defined as,

$$A = -\log\left(\frac{I_{out}}{I_{in}}\right) = -\log(T) \tag{5-9}$$

Thus, Beer-Lambert's Law can be extracted as follows where ε is molar absorption coefficient and c is molar concentration.

$$A = \varepsilon c l \tag{5-10}$$

In spectroscopy, transmittance is reported as percent transmittance (%T) and absorbance is calculated accordingly as given in equation (5-11).

$$\begin{gathered} \%T = \frac{I_{out}}{I_{in}} * 100 \\ A = -\log(T) \end{gathered} \tag{5-11}$$

For spectral measurements, first a measurement is done without the sample which is used as I_{in}. Then, another measurement with the sample placed in the optical path is run that is recorded as I_{out}. After data sampling and Fourier transform, percent transmittance and absorbance spectra are calculated by equation (5-11).

Interferogram of a broadband source is composed of individual contributions of all wavelengths in the range. This corresponds to addition of sinusoids with various frequencies. The resultant wave pattern is shown in Figure 5.5 (c). This figure is created in MATLAB for a device deflecting 400µm p-p at 350Hz with an input voltage of 20V. As shown in the first plot, the moving grating fingers get pulled to the level of the stationary grating fingers when the voltage is applied. After zero deflection level, the moving part goes with its own inertia until the voltage is applied again. When OPD is zero (both moving and stationary fingers are at the zero deflection level), all wavelength components

interfere constructively that results in the highest intensity in the interferogram which is called centerburst.

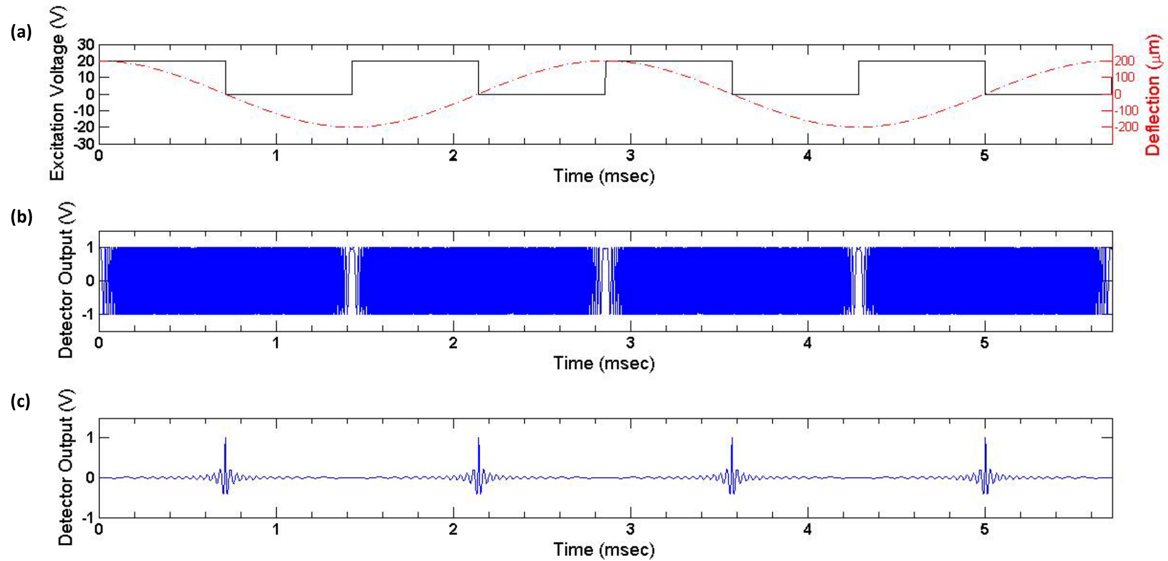

Figure 5.5 (a) Excitation voltage and deflection curve vs. time. (b) Laser interferogram. (c) IR interferogram.

The actual spectrometer setup built with LGI MEMS device and MEMFIS optical elements is shown in Figure 5.6.

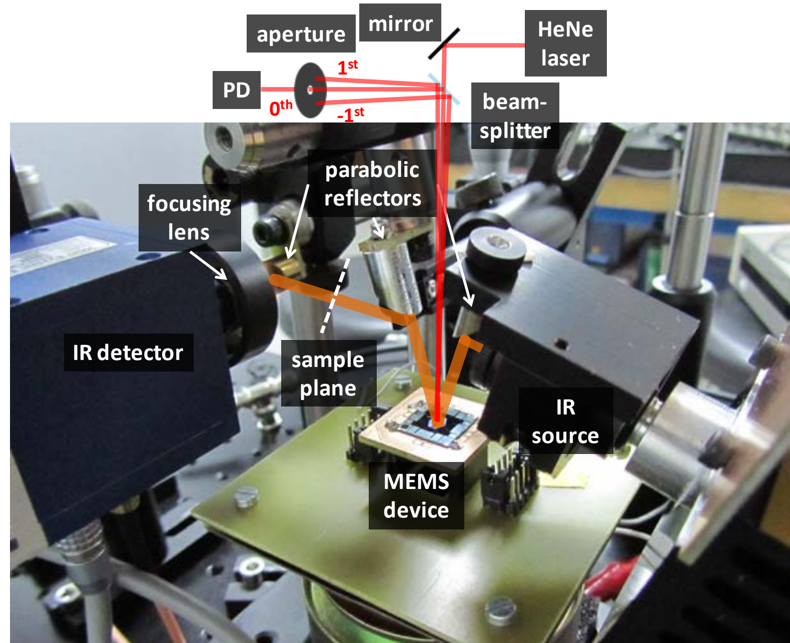

Figure 5.6 Actual LGI based FTIR spectrometer setup.

5.3 Data Acquisition and Analysis

The basic operation principle of LGI based FTIR was described in the previous section. There are two ways to capture and analyze the interferogram data. The first one is summarized in Figure 5.7. In this method, laser interferogram is passed through a zero crossing detector, which is a comparator with negative input connected to the ground, and then fed to the ADC clock input. At the same time, the MEMS driving signal is used as trigger to start/stop data acquisition. Then, digitized IR interferogram is sent to the computer and Fourier transform is applied. This method requires a comparator with a very small delay.

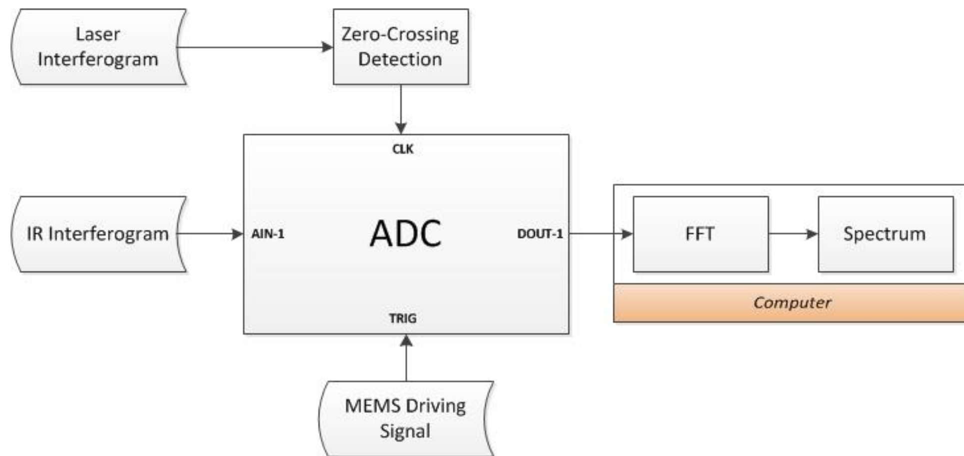

Figure 5.7 Data acquisition and analysis with chirped clock sampling.

The second method on the other hand, relies on digitizing both IR and laser interferograms and then computing the spectrum on computer. The method is summarized in Figure 5.8. This method requires more post processing than the first method, therefore takes more time to compute the spectrum.

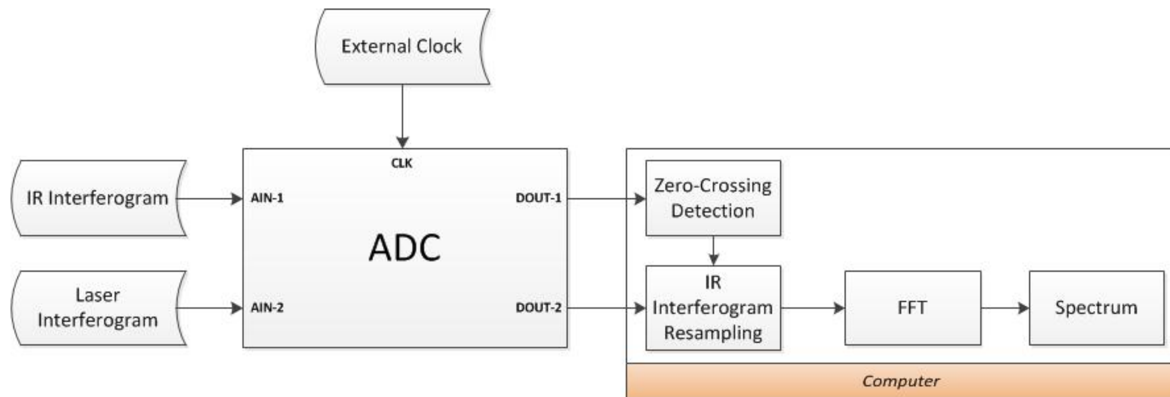

Figure 5.8 Data acquisition and analysis with interpolated zero-crossing detection sampling.

The Nyquist sampling theorem states that a band limited signal with B being the highest frequency, can be reconstructed if sampling frequency is at least 2B. B can be correlated to

the spectral domain where k_{max} is the maximum wavenumber at the detector. The frequency of the sine wave in the interferogram is then Vk_{max}, where V stands for the optical velocity. Therefore according to the Nyquist criterion, the interferogram must be sampled at $2Vk_{max}$ Hz or $1/(2Vk_{max})$ seconds. This corresponds to a sampling distance of $1/(2k_{max})$ in OPD domain [25]. The wavelength range of MEMFIS project is defined as 2.5-16μm, so the highest wavenumber is k_{max}=4000cm^{-1}. In order to meet the Nyquist criterion, the IR interferogram must be sampled at every 1250nm at least. In most FTIR systems, including our LGI based spectrometer as well, a HeNe laser with λ=632.8nm wavelength is used as reference. IR interferogram is sampled at every zero-crossing of laser interferogram that corresponds to a sampling distance of λ/2=316.4nm in OPD domain meaning that Nyquist criterion is met.

There are M resolution elements in a spectrum measurement for k_{min}-k_{max} range with Δk resolution such that,

$$M = \frac{k_{max} - k_{min}}{\Delta k} \tag{5-12}$$

From this, the resolution of the analog-to-digital converter (ADC) can be calculated by multiplying the dynamic range of the spectrometer with $M^{1/2}$ [25].

The desired dynamic range for MEMFIS spectrometer is defined as 500:1 while the wavenumber range is 625-4000cm^{-1}. As stated in the previous chapters, 10cm^{-1} resolution is aimed. The minimum required ADC resolution for MEMFIS can be calculated by multiplying the square root of number of resolution elements, M=(4000-625)/10=337.5, with the dynamic range of the spectrometer. Thus, ADC must have a resolution of approximately 9185 that corresponds to 14 bits at least.

For the electronics part of LGI based FTIR spectrometer, evaluation board for a 16 bit ADC from Analog Devices (AD9269) with internal clock of 80MSps is employed. To

transfer the digitized data to computer a compatible data capturing board, HSC-ADC-EVALC is acquired. These instruments are mainly targeted for telecommunication applications however; this was the only available 16 bit ADC data capturing system on the market at the time. Since the evaluation board was specialized for much higher frequencies, heavy filtering was built. To be able to detect our signals, we modified the evaluation board, particularly by-passed the filters.

To realize the first method for data acquisition and analysis with chirped clock sampling, a comparator from Linear Technology (LT1715) with a delay of 4ns is used. However, the evaluation board strictly required a noise free clock input. Any instrument connected to the evaluation board other than function generator introduced noise in the signal. On top of it, the output of the zero-crossing detector was not recognized by the evaluation board at all.

Although the computational time of the first method is less than the second, we were forced to use the second method with extensive post processing. In this method, both IR and laser interferograms are captured and transferred to computer by using the VisualAnalog software. Since the FPGA module on the data capturing board has a memory of 32kB and the data is not continuous, an external clock of 10MHz is applied to make sure that at least one double sided interferogram was involved in the captured data. 32kB memory corresponds to 32768 datapoints so, for LGI MEMS devices working at around 350Hz (T=2.8ms), 10MHz sampling frequency was enough. Not only for the continuity of the data but also for the sampling frequency to meet the Nyquist rate for the laser interferogram, 10MHz was suitable. Note that the most frequent sinusoid in the chirped laser interferogram of a HeNe laser with 632.8nm wavelength for an LGI MEMS device moving 1mm p-p at 350Hz has a frequency of 3.5MHz.

After the data both with and without sample is stored, it is imported to MATLAB for analysis.

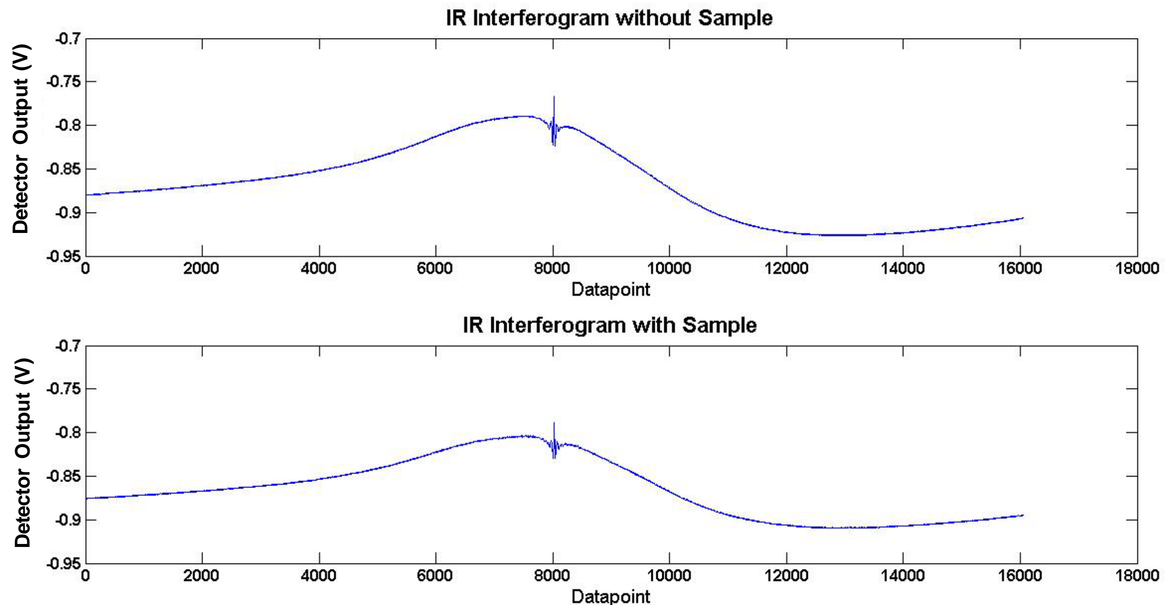

Figure 5.9 IR interferograms with and without sample before filtering.

Firstly, all data is filtered to remove the noise from both interferograms and especially to remove the sinusoidal noise on the IR interferogram. For this, a second order Butterworth filter is used. The cutoff frequencies are determined by trial and error. After that, data is cropped such that double sided interferograms from both IR and laser signals are obtained at each dataset where a dataset is defined as 32768 datapoints long data chunk. For data cropping, a peak detection algorithm is developed.

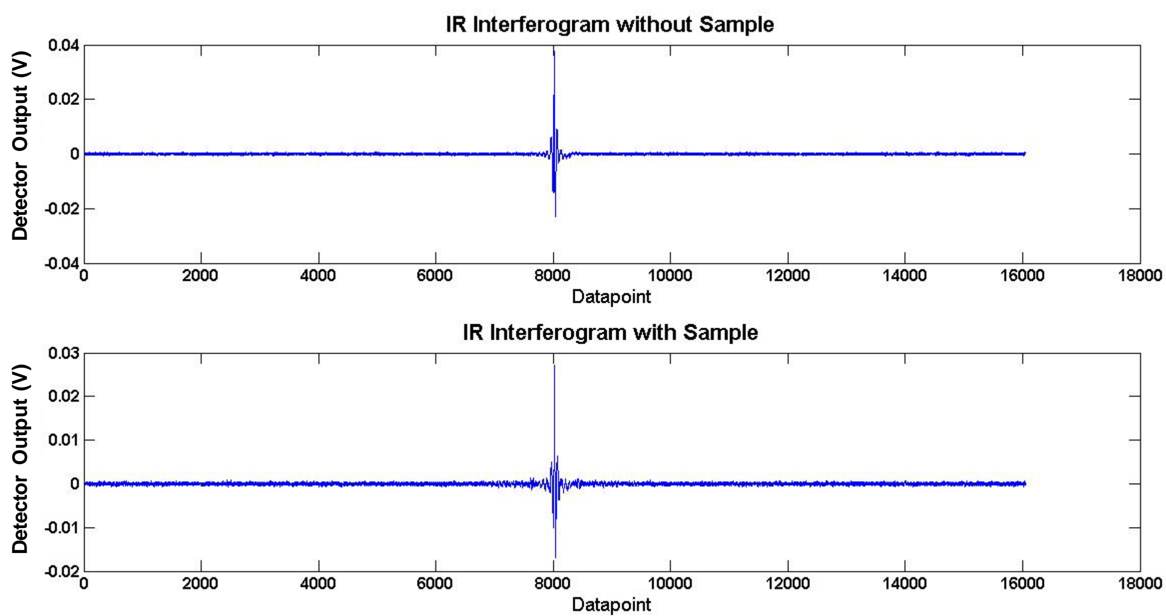

Figure 5.10 IR interferograms with and without sample after filtering.

The effect of sample is clearly observed when IR interferogram is zoomed in. Extra sidebursts emerge as seen in Figure 5.11.

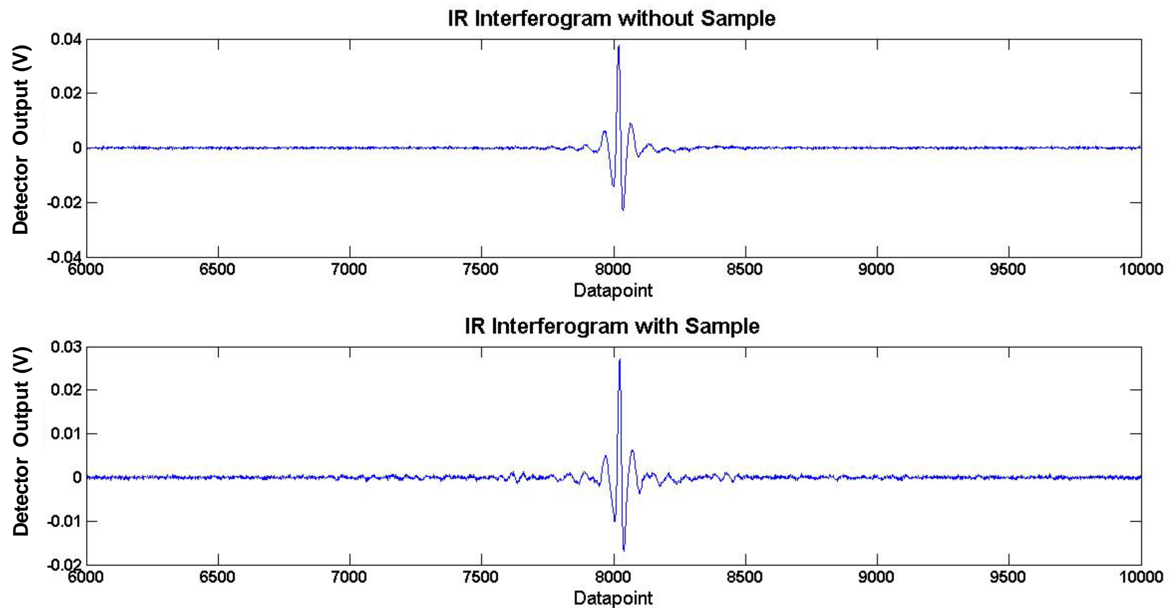

Figure 5.11 IR interferograms with and without sample after filtering – zoomed in.

Then, IR interferogram is resampled at the zero crossings of the laser interferogram to ensure equidistant sampling in OPD domain. After zero padding, Fourier transform of resampled IR interferogram is computed. This procedure is repeated many times and all the spectra acquired are averaged. These steps are performed for data both with and without sample. At the end, two spectra are obtained, one with sample and one without sample.

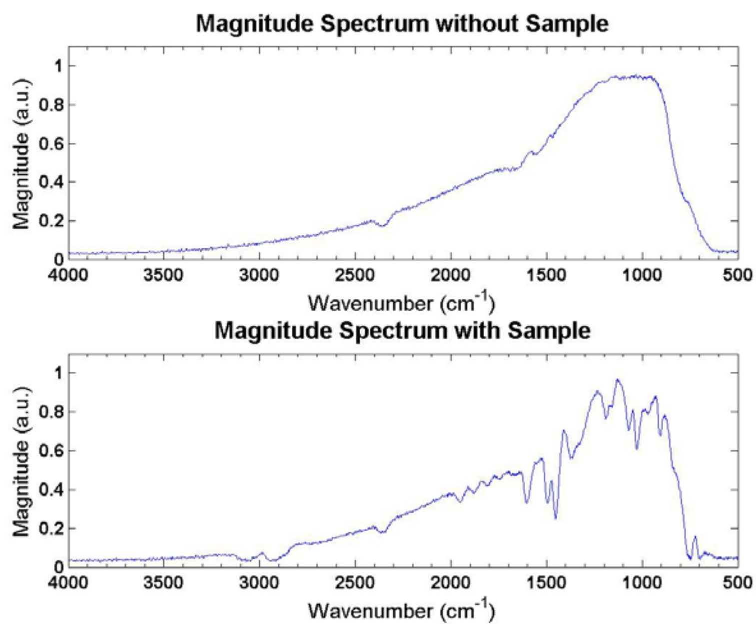

Figure 5.12 Magnitude spectrum with and without sample.

Finally, percent transmittance and absorbance spectra are calculated using equation (5-11).

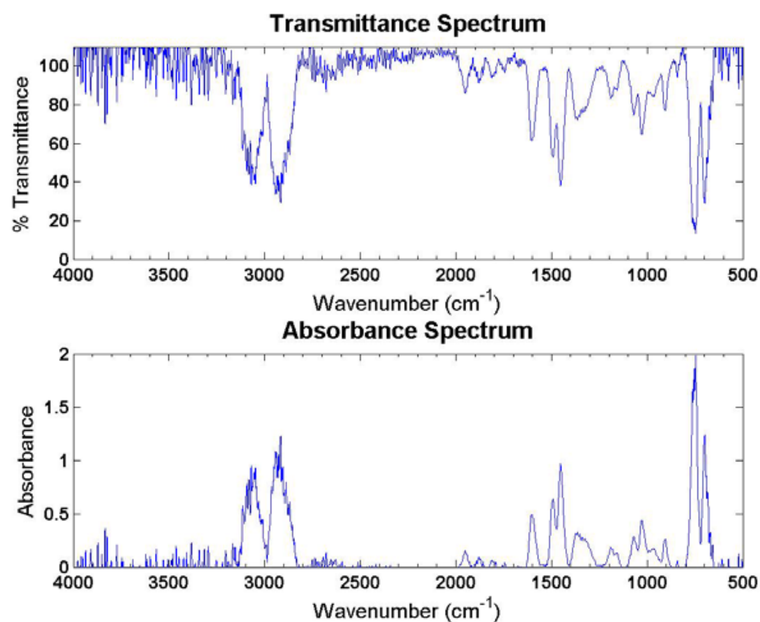

Figure 5.13 % Transmittance and absorbance spectrum.

For analysis, several computation options are investigated. These options will be explained in the next section with related spectrum results.

5.4 Spectrum of Polystyrene

Polystyrene is a polymer that is widely used as reference in infrared spectrometry. A thin polystyrene film is used for characterizing the IR setup. For comparison, the same film is measured by Alpha-T FTIR Spectrometer from Bruker Optics that has $4cm^{-1}$ resolution.

Firstly, the effect of deflection on resolution is observed. Device III-SK is actuated electrostatically; increasing the input voltage thus the deflection in each step. For analysis, 32 datasets are averaged after Fourier transform.

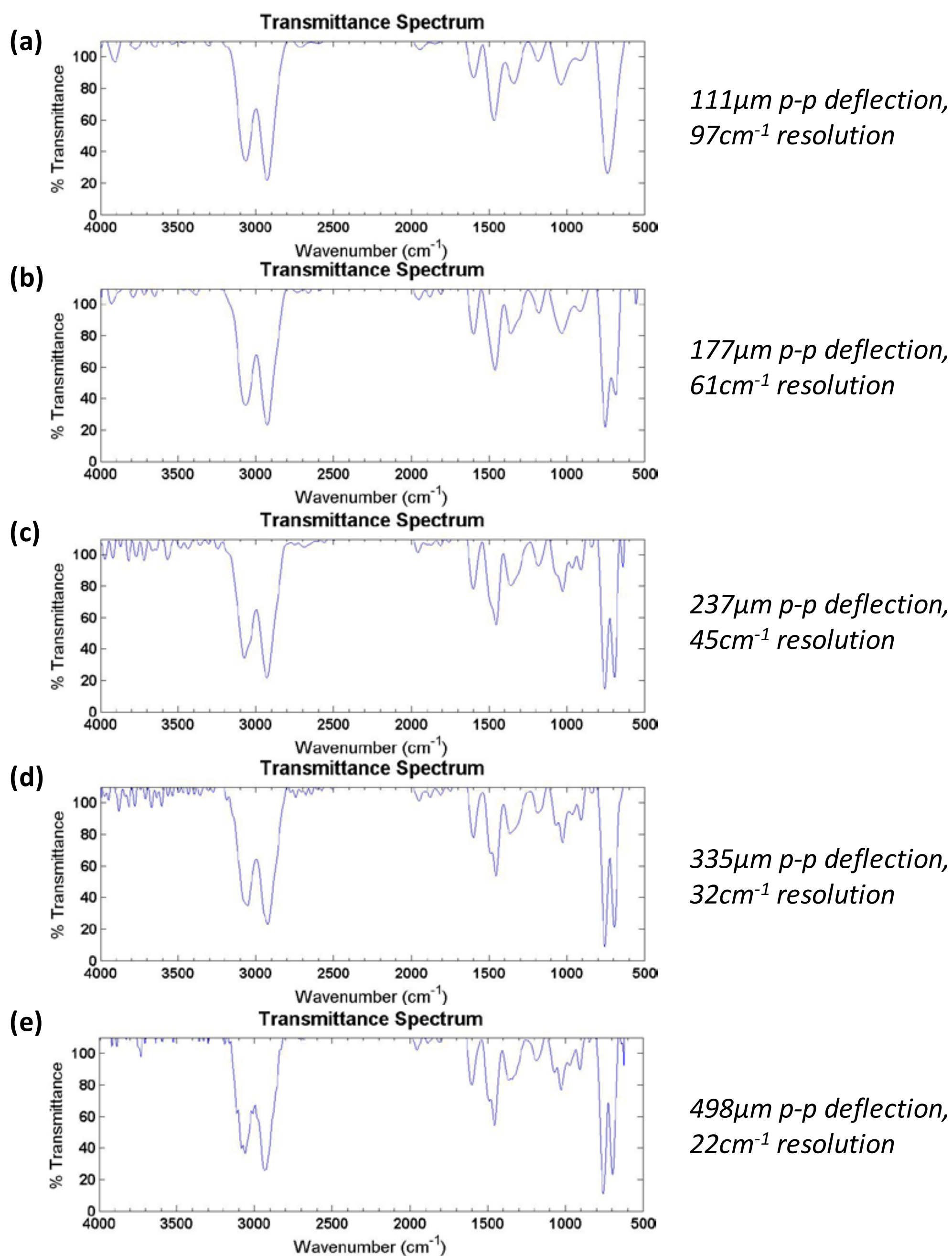

Figure 5.14 Effect of deflection on resolution.

As clearly seen in Figure 5.14, the experimental resolution is improved as well as the theoretical resolution that is provided in the figure as deflection increases. However, it should be noted that experimental resolution is worse than the theoretical. The most significant example is change in the resolvability of two absorption peaks around 750cm^{-1} from plot (a) to (c). Less distinctive changes in resolution or smaller absorption peaks can be seen around 970cm^{-1}, 1050cm^{-1} and 1490cm^{-1}. Note that the resolution values given for each plot are theoretical values assuming an incidence angle of 22°.

Another feature investigated in the analysis is data cropping. Device III-SK is actuated electrostatically with 50V at 518Hz and a p-p deflection of 533µm is obtained. Results of data cropping effect on resolution are given in Figure 5.15. Cropping the interferogram means decreasing OPD, and this results in a worse resolution. However after a certain point in the interferogram, the data becomes useless and does not contain any spectral information. For this particular OPD, using double sided interferogram or cropping 50% from both ends did not make any difference. Nevertheless, it is safer to use the double sided interferogram.

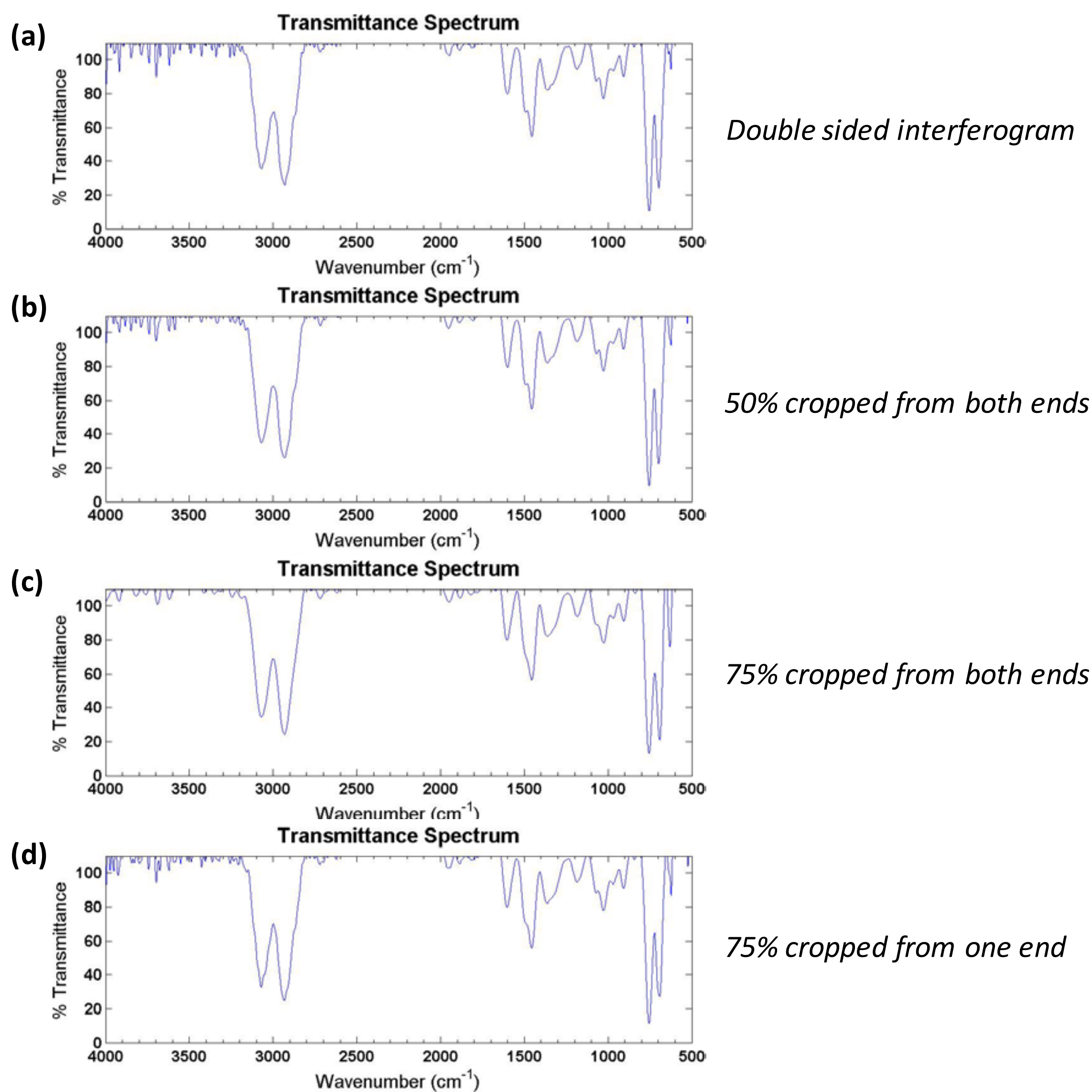

Figure 5.15 Effect of data cropping on resolution.

The asymmetry created by slightly inclined sinusoidal noise on the IR interferogram remained after filtering. In order to see if it can be overcame by using one sided interferogram and flipping it to make a perfectly symmetric double sided interferogram,

two more analysis are done. As it can be observed in Figure 5.16 (b) and (c), the resolution got worse.

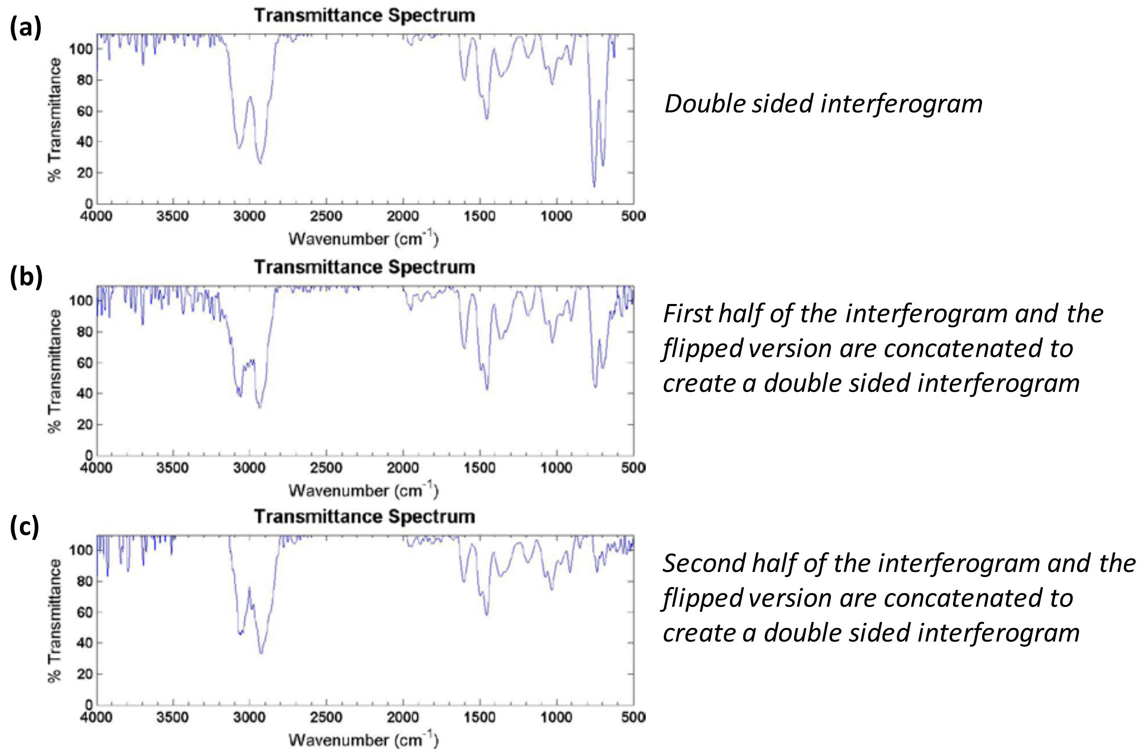

Figure 5.16 Effect of asymmetry in resolution.

The effect of averaging on increasing signal-to-noise ratio, thus improving the resolution can be seen in the spectra below, calculated with LGI MEMS device I-SA moving 931µm p-p at 311.6Hz with speaker actuation. It should be noted that after averaging 32 datasets, SNR does not seem to be improving much.

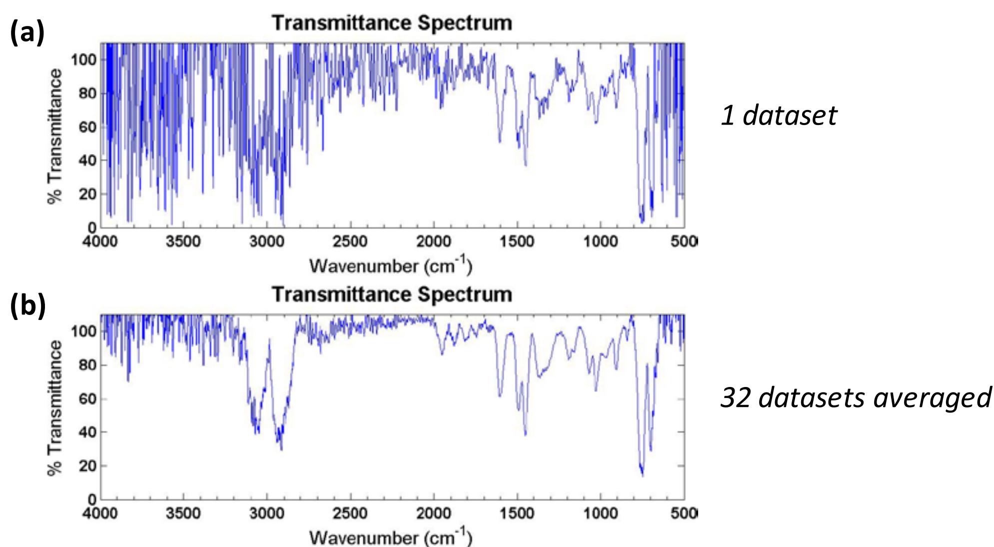

Figure 5.17 Effect of averaging on resolution.

Not only averaging operation but also when it is done has a huge effect on resolution. Aforementioned averaging was done after Fourier transform was applied. However, averaging can also be done at interferogram level. Below figure shows the % transmittance spectrum comparison between spectra calculated by averaging 32 datasets after Fourier transform is applied, before interferogram resampling and after interferogram sampling. It is observed that averaging before interferogram resampling gives the clearest spectrum. In addition, the computational time substantially decreases compared to spectrum averaging since Fourier transform is applied only once.

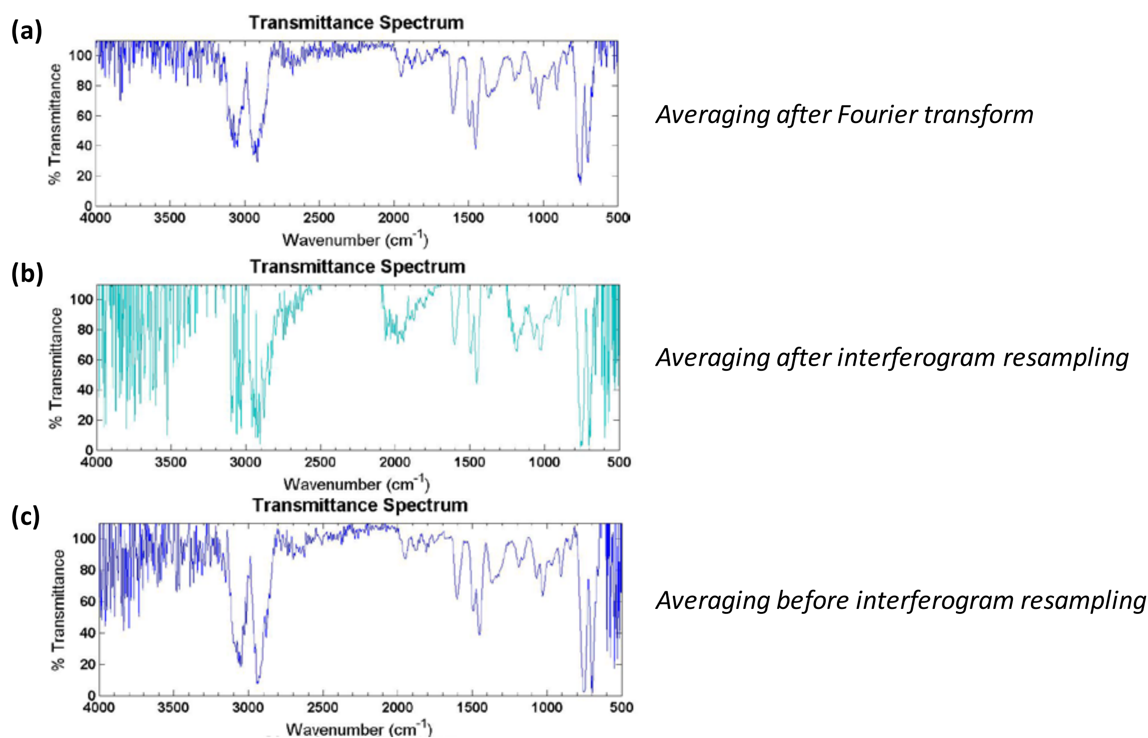

Figure 5.18 Effect of at which step averaging is applied on resolution.

As stated before, IR interferogram resampling is done by using the reference laser's zero crossings. If the deflection and vibration frequency of the MEMS device is known, laser interferogram could be created in MATLAB. Figure 5.19 shows that an artificially created reference laser interferogram works as good as the actual reference laser. This property makes the LGI based FTIR spectrometer much smaller than its counterparts. The only possible drawback of this method is mechanical instability in MEMS device which can lead to a change in vibration frequency or deflection.

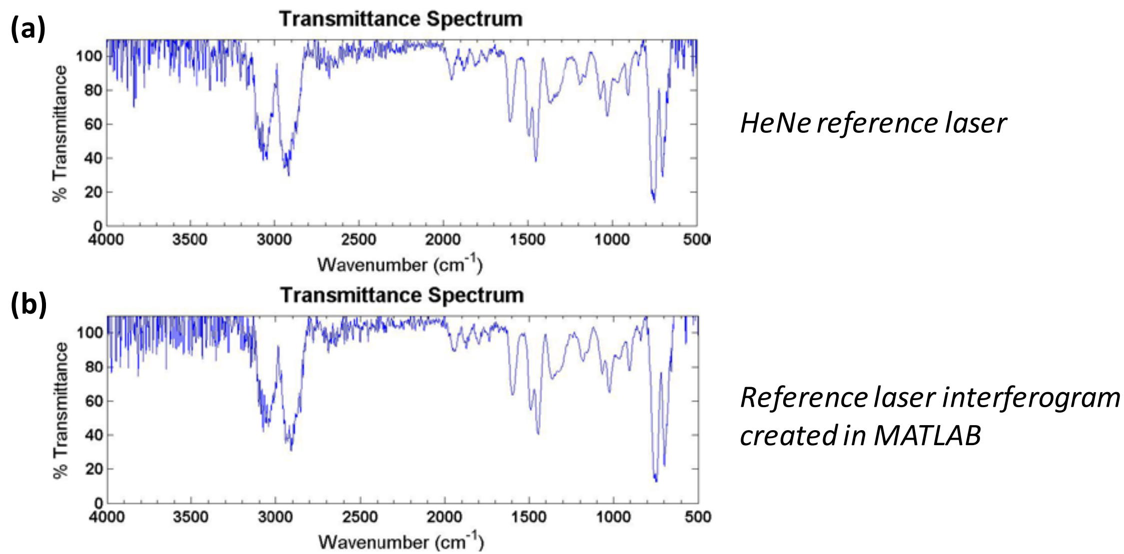

Figure 5.19 Effect of reference laser interferogram on resolution.

Thirteen cases with different lens combinations were simulated in the previous chapter. Case#1, case#12 and case#13 are experimentally realized. The results turned out to be quite consistent with simulations. The best spectrum is obtained in case#13, where one-to-one imaging is done using an off-axis parabolic mirror with 20mm focal length as both collimating and focusing mirror. Although similar experimental conditions were tried to be created for consistency, there happened to be slight changes in vibration frequency, deflection, number of datasets, incidence angle and the distance between optical components. Device I-SA was deflecting 931µm p-p at 311.6Hz with speaker actuation for case#1 as shown in Figure 5.20 (a). Incidence angle is measured as 14° and spectrum is obtained by averaging 32 samples before resampling. In case#12 and case#13, device I-SA was deflecting 936µm p-p at 312Hz with speaker actuation as shown in Figure 5.20 (b) and (c) respectively. The incidence angle is 17° and 72 datasets for case#12 and 86 datasets for case#13 are averaged before resampling.

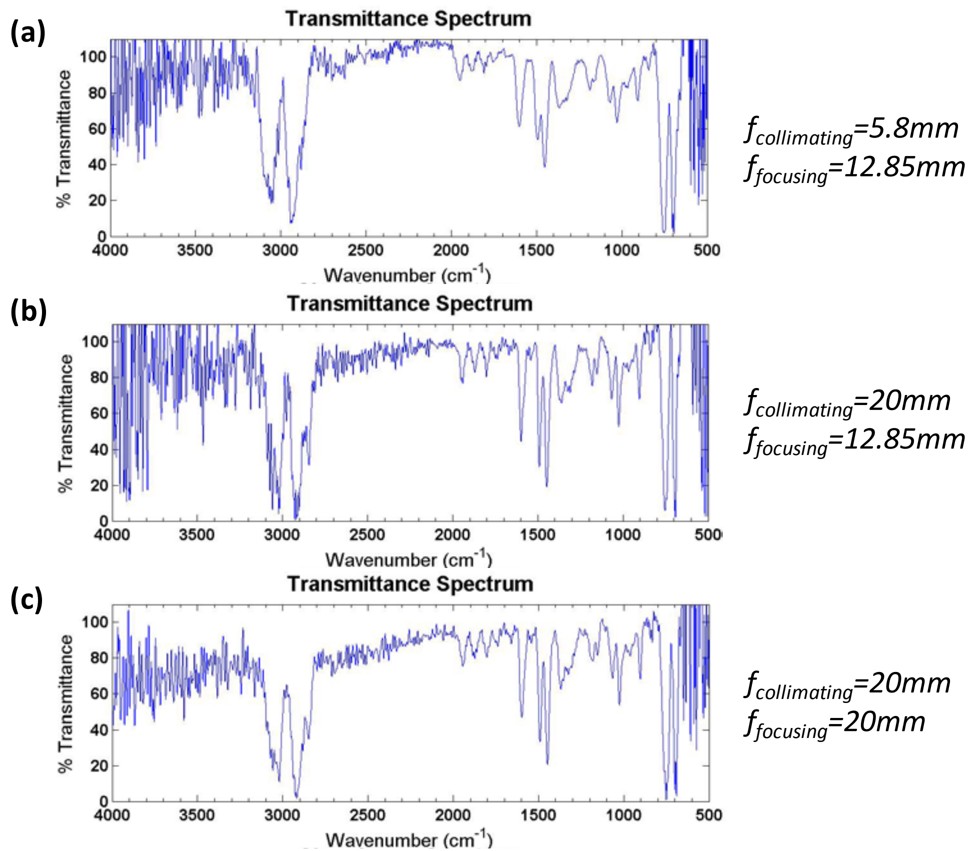

Figure 5.20 Spectra obtained with different lens combinations.

Consequently, the best spectrum is obtained using double sided interferograms averaged before resampling with off-axis parabolic mirrors with 20mm focal length are used as both collimating and focusing mirrors. The highest stable deflection achieved was 936μm p-p with speaker actuation. Despite the spectrum being noisy due to low performance of the detector mainly, absorption peaks are coherent with the spectrum measured with a commercially available FTIR spectrometer. The figure below shows our best spectrum compared to the one measured with Bruker Optics' Alpha-T spectrometer.

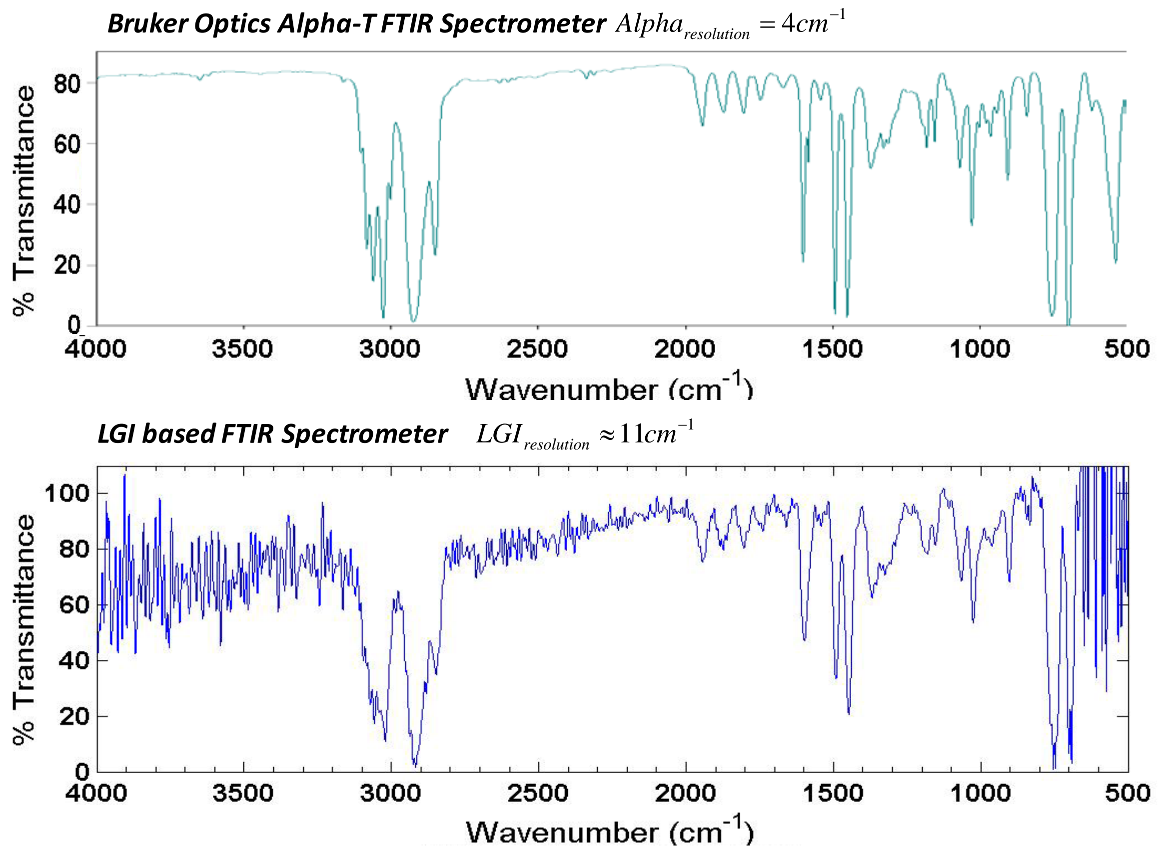

Figure 5.21 Spectrum comparison of LGI based FTIR spectrometer and Bruker Optics' Alpha-T FTIR spectrometer.

5.5 Application: Thin Film Thickness Measurement

In IC industry, epitaxial layer thickness is a critical parameter that must be monitored during fabrication. FTIR spectrometry provides a non-destructive and fast way for measuring thin film thickness. Basic working principle can be described as follows. Radiation from the IR source is modulated in the interferometer, and then gets reflected from the sample creating an interferogram that includes thickness information as shown in Figure 5.22 (a).

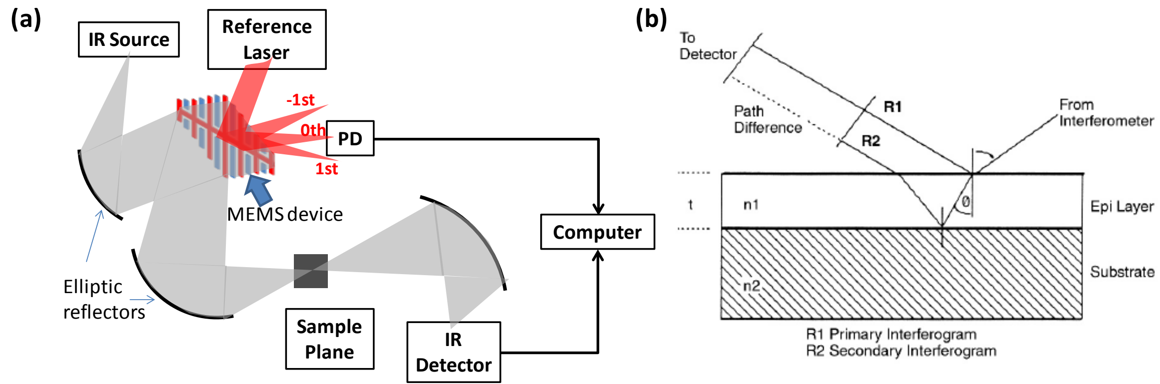

Figure 5.22 (a) LGI based FTIR spectrometer modified for film thickness measurement. (b) Detailed view of sample plane [29].

In the sample plane, the light coming from the LGI MEMS device partly reflects from the sample surface while the remaining light passes through the epitaxial layer, and then reflects from the interface of the film and the substrate. The optical path difference between these two reflected lights results in an interference pattern which introduces two distinctive sidebursts located at a certain distance to the centerburst. The film thickness is related to the position of these sidebursts with the formula given below,

$$t = \frac{\Delta}{2n_1 \cos\theta} \tag{5-13}$$

where 2Δ is the distance between sidebursts in OPD domain, t and n_1 are the thickness and refractive index of the epitaxial layer respectively, and θ is the angle of refraction in the epitaxial layer [30].

For experimental implementation, a 20µm thick silicon on top of a silicon-oxide substrate is used. The recorded IR interferogram is plotted in the OPD domain using laser interferogram for deflection calculation. The distance between sidebursts is measured from Figure 5.23 as 2Δ=266µm. Assuming the refractive index of silicon as n_1=3.45 and

calculating the angle of refraction from Snell's Law as θ=15.6°, the thickness of the silicon can be calculated as t=20.01 which is quite accurate.

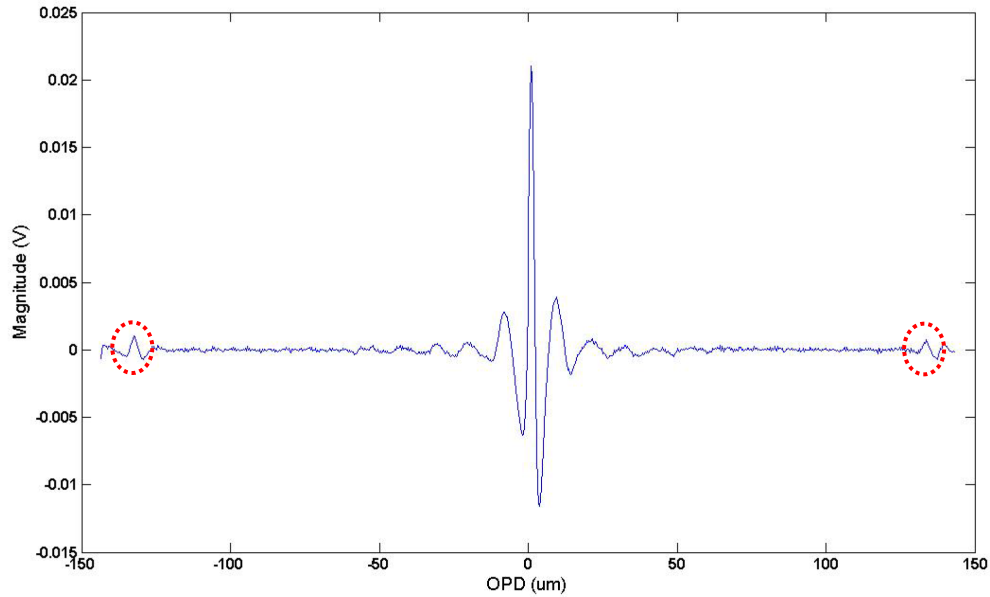

Figure 5.23 IR interferogram obtained with 20μm silicon film in the optical path.

Nonetheless as the epitaxial layer gets thinner, the sidebursts get closer and closer to the centerburst and becomes indistinguishable. Thus, this method is not suitable for measuring very thin films. However, there are still other techniques for extracting the thickness information from the interferogram which are beyond the scope of this thesis [31].

6 CONCLUSION

In this thesis, mechanical and optical characterization of LGI MEMS devices is explained and integration of a bench top LGI based MEMS FTIR spectrometer is described with optically optimized lens combinations. An experimental resolution of 25-30cm^{-1} is achieved with a device that deflects 936µm p-p with speaker actuation. Although the theoretical resolution requirement of the MEMFIS project (10cm^{-1}) could not be met fully, LGI based FTIR spectrometer is shown to perform the best in the LGI MEMS literature in a wide wavelength range (2.5-16µm).

For mechanical characterization, two automatized systems based on laser Doppler vibrometry and laser fringe counting, respectively, are implemented in Labview. MEMS devices are characterized easily, accurately, faster and in a more reliable fashion with these systems. Alternative actuation techniques with speaker and piezoelectric-vibrator are suggested to increase the deflection and to avoid electrostatic actuation related problems. These techniques both worked very well and probably will be used for the next generation LGI MEMS devices. A maximum p-p deflection of around 1mm is achieved stably with acoustic actuation with a relatively more linear frequency response. Preliminary results show that piezoelectric-vibrator actuation is a strong alternative as well. Further tests will be run with different custom piezoelectric elements.

The definition of resolution in LGI based spectrometers is investigated in detail followed by a comparison with experimental results. MEMS devices are optically characterized using a red HeNe laser and the experimental resolution turned out to be fully consistent with theoretical value. The optimum lens combination is found by simulating the system using a scalar diffraction theory based beam propagation code in MATLAB. In

addition, the power efficiency of three of these lens combinations is calculated with ray tracing in ZEMAX. Also, it was shown that LGI based FTIR spectrometer could be used as an instrument for measuring epitaxial layer thickness. The thickness of a 20μm silicon on top of a silicon-oxide substrate is measured accurately using LGI based FTIR spectrometer.

BIBLIOGRAPHY

[1] B. Stuart, *Infrared spectroscopy*: Wiley Online Library, 2004.

[2] D. Steele, "Infrared spectroscopy: theory," *Handbook of Vibrational Spectroscopy,* 2002.

[3] D. W. Ball, "The basics of spectroscopy," 2001.

[4] P. Felgett, "A propos del la theorie du spectrum etre interferential multiplex," *le Journal de Physique et le Radium,* vol. 19, p. 187, 1958.

[5] P. Jacquinot, C. Dufour, and J. Rech, "Optical conditions in the use of photo-electric cells in spectrographs and interferometers," *J. Rech. CNRS,* vol. 6, p. 91, 1948.

[6] J. Connes, "Recherches sur la spectroscopie par transformation de Fourier," *Rev. Opt. Theor. Instrum.,* vol. 2, pp. 45-79, 1961.

[7] J. B. Robert, "Introductory fourier transform spectroscopy," ed: New York, Academic Press, 1972.

[8] J. Strong and G. A. Vanasse, "Lamellar Grating Far-Infrared Interferomer," *J. Opt. Soc. Am.,* vol. 50, pp. 113-113, 1960.

[9] O. Manzardo, R. Michaely, F. Schädelin, W. Noell, T. Overstolz, N. De Rooij, and H. P. Herzig, "Miniature lamellar grating interferometer based onsilicon technology," *Opt. Lett.,* vol. 29, pp. 1437-1439, 2004.

[10] F. Merenda, S. Buhler, H. Farah, G. Boer, and T. Scharf, "Portable NIR/MIR Fourier-transform spectrometer based on a common path lamellar grating interferometer," Orlando, Florida, USA, 2010, pp. 76800V-12.

[11] A. Caglar, U. Hakan, and W. Alexander, "A Fourier transform spectrometer using resonant vertical comb actuators," *Journal of Micromechanics and Microengineering,* vol. 16, p. 2517, 2006.

[12] Y. Hongbin, Z. Guangya, C. F. Siong, L. Feiwen, W. Shouhua, and Z. Mingsheng, "An electromagnetically driven lamellar grating based Fourier transform microspectrometer," *Journal of Micromechanics and Microengineering,* vol. 18, p. 055016, 2008.

[13] F. Lee, G. Zhou, H. Yu, and F. S. Chau, "A MEMS-based resonant-scanning lamellar grating Fourier transform micro-spectrometer with laser reference system," *Sensors and Actuators A: Physical,* vol. 149, pp. 221-228, 2009.

[14] S. Wang, H. Yu, and S. Chau Fook, "A Miniaturized Lamellar Grating Based Fourier Transform Spectrometer With Electrostatic Actuation," *Sensors Journal, IEEE,* vol. 10, pp. 1869-1874, 2010.

[15] C. Ataman and H. Urey, "Vertical Resonant Comb Actuators for Fourier Transform Spectroscopy," in *Optical MEMS and Their Applications Conference, 2006. IEEE/LEOS International Conference on*, 2006, pp. 44-45.

[16] C. Ataman and H. Urey, "Modeling and characterization of comb-actuated resonant microscanners," *Journal of Micromechanics and Microengineering,* vol. 16, p. 9, 2006.

[17] K. L. Turner, S. A. Miller, P. G. Hartwell, N. C. MacDonald, S. H. Strogatz, and S. G. Adams, "Five parametric resonances in a microelectromechanical system," *Nature,* vol. 396, pp. 149-152, 1998.

[18] C. Ataman, "Mems Scanners for Spectroscopy and Laser Scanning Systems," PhD, Koc University, Istanbul, 2008.

[19] H. R. Seren, "MEMS Fourier Transform Spectrometer Using Lamellar Grating," M.Sc., Koc University, Istanbul, 2009.

[20] T. Sandner, C. Drabe, H. Schenk, A. Kenda, and W. Scherf, "Translatory MEMS actuators for optical path length modulation in miniaturized Fourier-transform infrared spectrometers," *Journal of Micro/Nanolithography, MEMS and MOEMS,* vol. 7, p. 021006, 2008.

[21] T. Sandner, T. Grasshoff, and H. Schenk, "Translatory MEMS actuator with extraordinary large stroke for optical path length modulation," in *Optical MEMS and Nanophotonics (OPT MEMS), 2010 International Conference on*, 2010, pp. 25-26.

[22] H. R. Seren, N. P. Ayerden, J. Sharma, S. T. S. Holmstrom, T. Sandner, T. Grasshoff, H. Schenk, and H. Urey, "Lamellar grating based MEMS Fourier Transform Spectrometer," in *Optical MEMS and Nanophotonics (OPT MEMS), 2010 International Conference on*, 2010, pp. 105-106.

[23] H. R. Seren, S. Holmstrom, N. P. Ayerden, J. Sharma, and H. Urey, "Lamellar-Grating-Based MEMS Fourier Transform Spectrometer," *Microelectromechanical Systems, Journal of,* vol. PP, pp. 1-9, 2012.

[24] A. M. Elshurafa, K. Khirallah, H. H. Tawfik, A. Emira, A. K. S. Abdel Aziz, and S. M. Sedky, "Nonlinear Dynamics of Spring Softening and Hardening in Folded-MEMS Comb Drive Resonators," *Microelectromechanical Systems, Journal of,* vol. 20, pp. 943-958, 2011.

[25] P. R. Griffiths and J. A. De Haseth, *Fourier transform infrared spectrometry* vol. 171: Wiley-Interscience, 2007.

[26] V. Saptari, "Fourier transform spectroscopy instrumentation engineering," 2004.

[27] O. Ferhanoglu, H. R. Seren, S. Lüttjohann, and H. Urey, "Lamellar grating optimization for miniaturized fourier transform spectrometers," *Opt. Express,* vol. 17, pp. 21289-21301, 2009.

[28] N. V. Tkachenko, *Optical spectroscopy: methods and instrumentations*: Elsevier Science, 2006.

[29] R. B. Fred Walder, "FT-IR Measurement of Epitaxial Film Thickness Applications," Thermo Scientific2008.

[30] Z. Zhen-Hong and R. Reif, "Epi-film thickness measurements using emission Fourier transform infrared spectroscopy. I. Sensor characterization," *Semiconductor Manufacturing, IEEE Transactions on,* vol. 8, pp. 333-339, 1995.

[31] A. A. P. Cherkassky, "Metrology of thin silicon expitaxial films: determination of epitaxial film thickness by Fourier-transform infra-red spectrometry," Massachusetts Institute of Technology, 1995.